TECHNISCHE UNIVERSITÄT WIEN

INSTITUT FÜR MECHANIK UND MECHATRONIK
Mechanics & Mechatronics

Design, Modeling and Implementation of a Cable Driven Parallel Robot

DIPLOMA THESIS

Conducted in partial fulfillment of the requirements for the degree of a

Diplom-Ingenieur (Dipl.-Ing.)

supervised by

Ao.Univ.-Prof. Dr.techn. Horst Ecker
Univ.-Prof. Dr. techn. Andreas Kugi
Dipl.-Ing. Ulrich Knechtelsdorfer BSc
Dipl.-Ing. Michael Schwegel BSc

submitted at the

TU Wien

Faculty of Mechanical and Industrial Engineering
Institute E325 - Mechanics and Mechatronics

by
Georg Feiler
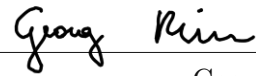Matriculation number 01525499

Vienna, March 2023

Eidesstattliche Erklärung

Hiermit erkläre ich, dass die vorliegende Arbeit gemäß dem Code of Conduct - Regeln zur Sicherung guter wissenschaftlicher Praxis (in der aktuellen Fassung des jeweiligen Mitteilungsblattes der TU Wien), insbesondere ohne unzulässige Hilfe Dritter und ohne Benutzung anderer als der angegebenen Hilfsmittel, angefertigt wurde. Die aus anderen Quellen direkt oder indirekt übernommenen Daten und Konzepte sind unter Angabe der Quelle gekennzeichnet. Die Arbeit wurde bisher weder im In- noch im Ausland in gleicher oder in ähnlicher Form in anderen Prüfungsverfahren vorgelegt.

Wien, März 2023

Georg Feiler

Preamble

This thesis is the first of two master theses dealing with the design and development of a cable driven robot technology demonstrator, which is able to catch a flying dart thrown by a human such that the dart hits any desired field on the dartboard.

The project marks the end of my two studies in both mechanical engineering and electrical engineering at TU Wien, which have shaped my life in many ways. I will always look back to my time at university with fond memories. I want to express my deep and honest gratitude to many individuals that I had the honor of meeting, working and studying with, who have made my journey unique, enjoyable and unforgettable.

I want to thank Prof. Horst Ecker and Prof. Andreas Kugi for the opportunity to conduct this thesis and for the possibility to dedicate my time to such an inspiring and interesting project. Prof. Kugi's way of teaching and organizing research have taught me that academic research can be meaningful, sustainable and fun at the same time. I want to express my deep gratitude to Prof. Ecker for his continuous support throughout my studies. Thank you for all the cordial and honest conversations, your invaluable experience and your keen insights.

My sincere gratitude belongs to Ulrich Knechtelsdorfer and Michael Schwegel for their continuous support and supervision. Without their theoretical knowledge and expertise, their practical mindset and their creativity this thesis would not have been possible. Thank you for your dedication, your open ears and your patience with me.

I also want to thank Thomas Weingartshofer, Gerald Ebmer and Christian Hartl-Nešić for their tireless and generous help with hardware and software related problems which saved me countless frustrating hours.

I am also very grateful for the inexhaustible support, encouragement and love of my family. I want to thank my parents Maria and Gerhard for their encouragement and support which enabled me to focus on my studies. I want to thank my brother Martin for challenging me to strive for excellence and to never give up in times of failure. I want to thank my lovely girlfriend Luisa for her love and ongoing support along the way.

Last but not least, I would like to express my deep gratitude and sincere appreciation to the fellow students that I had the pleasure of studying with and who have become good friends in the process. Thank you Felix, Benjamin, Elias, Christopher and Jan for all the inspiring conversations, your ideas and your advice.

Vienna, March 2023

Abstract

In the present work, a novel class of planar cable driven parallel robots is designed, analyzed and mathematically modelled.

For conventional cable driven robots, the cables are rigidly attached to the end effector. This results in a very limited capability of rotating the end effector. To overcome this limitation and allow an arbitrary amount of rotation, the proposed design uses cables which are wrapped around a cylindrical fixture on the end effector. In contrast to the state of the art, this results in a simple and robust design without any additional moving parts attached to the end effector.

All possible cable configurations are subsequently analyzed using Burnside's lemma known from group theory. A closed-form solution for the number of all possible configurations is derived. The workspace of different configurations is analyzed in detail and a suitable cable configuration for a prototype is selected.

Furthermore, a closed-form analytical solution for the inverse kinematics is derived and a solution for the forward kinematics is presented. Both the inverse and the forward kinematics are implemented on a real-time system and validated experimentally on a prototype robot. The convergence behavior and the robustness of the forward kinematic algorithm are studied in detail via simulations.

Based on the robot kinematics, a control-oriented dynamical model is derived and a trajectory following controller for the robot is designed. Experiments are conducted to validate the theoretical considerations and demonstrate the performance and capabilities of the novel cable driven robot concept.

Kurzfassung

Diese Arbeit beschäftigt sich mit dem Entwurf sowie der mathematischen Modellierung eines neuartigen planaren Seilroboters. Bei klassischen Seilrobotern ist der Endeffektor an festen Punkten mit Seilen verbunden und wird von diesen bewegt, wodurch die Möglichkeit den Endeffektor zu drehen sehr eingeschränkt ist. Um diese Einschränkung zu überwinden und beliebig große Rotationen des Endeffktors zu ermöglichen, wird eine neue Klasse von Seilrobotern entwickelt, bei der die Seile den Endeffektor umschlingen.

Dadurch entsteht ein sehr vielseitiger planarer Roboter, welcher sich durch einen einfachen, kostengünstigen und robusten Aufbau auszeichnet. Alle möglichen Seilkonfigurationen des Konzepts werden systematisch analysiert, und basierend auf Burnside's Lemma, welches aus der Gruppentheorie bekannt ist, wird eine Formel für die Anzahl aller möglichen Seilkonfigurationen hergeleitet. Der Arbeitsraum des Seilroboters wird anhand verschiedener Gütekriterien beleuchtet, um in weiterer Folge einen geeigneten Prototyp zu konzipieren. Eine geschlossene analytische Lösung für die Rückwärtskinematik wird hergeleitet, sowie eine Lösung der Vorwärtskinemaik präsentiert. Sowohl die Rückwärtskinematik als auch die Vorwärtskinematik werden auf einem Echtzeitsystem implementiert und an einem Prototyp des Roboters validiert. Die Konvergenzeigenschaften der Vorwärtskinematik sowie die Robustheit gegenüber Messrauschen werden anhand von Simulationen untersucht.

Basierend auf der Kinematik des Roboters wird ein dynamisches Robotermodell entwickelt und ein Trajektorienfolgeregler entworfen. Durch verschiedene Versuche und Messungen am experimentellen Prototyp werden die theoretischen Überlegungen validiert sowie die Leistungsfähigkeit des neuartigen Konzepts demonstriert.

Contents

List of Figures

List of Symbols

$\mathbf{x}$ $\in \mathbb{R}^n$ pose of the endeffector.

$\hat{\mathbf{x}}$ $\in \mathbb{R}^n$ approximate solution for the endeffector pose.

$\mathbf{x}^0$ $\in \mathbb{R}^n$ initial guess for the endeffector pose.

x_C x-coordinate of point C.

y_C y-coordinate of point C.

φ rotation angle of the endeffector.

$\hat{\varphi}$ approximate solution for the rotation angle of the endeffector.

φ^* exact solution for the rotation angle φ in the forward kinematics.

$\varphi_{\min}$ minimum rotation angle of the endeffector.

$\varphi_{\max}$ maximum rotation angle of the endeffector.

φ^0 initial guess for the rotation angle φ.

n_x degrees of freedom (DOF).

n_q number of cables.

m_1 classical manipulability measure for a robot.

m mass.

m_{EE} mass of the endeffector.

η force efficiency.

N number of points.

r_{w} radius of the circle on which the winches are mounted.

r radius of the endeffector.

γ angle between the cable contact point and the vertical axis.

s cable winding direction.

l total cable length.

l' length of the cable which is in contact with the endeffector.

l_{r} rolled cable length.

l_{s} spare cable length.

l_0 cable length in the reference pose defined by $\mathbf{r}_0$ and $\varphi = 0$.

$l_{\varphi 0}$ cable length without any endeffector rotation ($\varphi = 0$).

Δl change of the cable length relative to the reference pose.

$\mathbf{s}$ $\in \mathbb{R}^{n_q}$ vector of winding directions.

$\mathcal{B}$ set of balanced winding configurations.

$\mathcal{B}^{\sigma_k}$ set of configurations invariant to σ_k.

$\mathcal{E}$ set of task-space velocities with unit length joint velocities.

$\mathcal{P}_F$ set of available wrenches for the force-efficiency definition.

$\mathcal{U}$ set defining the inner workspace within a square of 25cm $\times$ 25cm.

$\mathcal{V}$ set defining the collision region which contains all points of the EE.

$\mathcal{W}$	wrench-closure workspace.
σ	standard deviation of measurement noise.
σ_k	circular shifting operator by k places.
$\mathcal{S}$	group of all circular shifting operators.
k	block length of a symmetrical configuration.
i, j	$\in \mathbb{N}$ counting index, cable index.
$\mathbf{q}$	$\in \mathbb{R}^{n_q}$ joint vector (cable lengths).
$\boldsymbol{\phi}_{\text{ik}}$	$\mathbb{R}^n \to \mathbb{R}^{n_q}$ mapping defining the inverse kinematic transformation.
$\boldsymbol{\phi}_{\text{fk}}$	$\mathbb{R}^{n_q} \to \mathbb{R}^n$ mapping defining the forward kinematic transformation.
$\hat{\boldsymbol{\phi}}_{\text{fk}}$	$\mathbb{R}^{n_q} \to \mathbb{R}^n$ approximation of $\boldsymbol{\phi}_{\text{fk}}$.
$\mathbf{J}_{\text{ik}}$	$\in \mathbb{R}^{n_q \times n_x}$ Jacobian matrix of the inverse kinematics.
$\mathbf{A}^{\text{T}}$	$\in \mathbb{R}^{6 \times n_q}$ structure matrix.
$\mathbf{M}$	$\in \mathbb{R}^{n_x \times n_x}$ mass matrix.
$\mathbf{C}$	$\in \mathbb{R}^{n_x \times n_x}$ Coriolis matrix.
$\boldsymbol{\Lambda}$	$\in \mathbb{R}^{n_x \times n_q}$ torque transmission matrix.
$\mathbf{r}_{AB}$	$\in \mathbb{R}^3$ vector pointing from point B to point A.
$\mathbf{r}_C$	$\in \mathbb{R}^3$ position vector pointing to point C.
$\hat{\mathbf{r}}_C$	$\in \mathbb{R}^3$ approximate solution of $\mathbf{r}_C$ from the forward kinematics.
$\mathbf{r}_0$	$\in \mathbb{R}^3$ reference position vector.
$\mathbf{e}_{AB}$	$\in \mathbb{R}^3$ unit vector in direction from point B to point A.
$\mathbf{e}_r$	$\in \mathbb{R}^3$ radial basis vector for polar coordinates.
$\mathbf{e}_\varphi$	$\in \mathbb{R}^3$ azimutal basis vector for polar coordinates.
h_A	offset between winch and groove-plane in z direction.
h_C	offset between point C and groove-plane in z direction.
e_C	position error of the endeffector center C.
$e_{C,xy}$	position error of the endeffector center C in the xy-plane only.
$r_{AC,xy}$	distance between the endeffector C and the winch A in the xy-plane only.
ψ	angle used in the inverse kinematics.
$\mathbf{R}_z$	$\in \text{SO}(3)$ rotation matrix around z-axis.
F_x	force on the endeffector in x-direction.
M_x	torque on the endeffector around x-axis.
τ	cable force.
τ_s	force in the most stressed cable.
$\boldsymbol{\tau}$	$\in \mathbb{R}^{n_q}$ vector of cable forces.
$\boldsymbol{\tau}_{\text{min}}$	$\in \mathbb{R}^{n_q}$ vector of minimum pretension cable forces.
$\boldsymbol{\tau}_{\text{max}}$	$\in \mathbb{R}^{n_q}$ vector of maximum cable forces.
$\mathbf{f}$	$\in \mathbb{R}^{n_x}$ vector of generalized forces (wrench) acting on the endeffector.
$\mathbf{f}_{\text{d}}$	$\in \mathbb{R}^{n_x}$ desired wrench vector on the endeffector.
$\mathbf{d}$	$\in \mathbb{R}^{n_x}$ direction of motion.
$\mathbf{g}$	$\in \mathbb{R}^{n_x}$ generalized gravity vector.
$\delta\mathbf{x}$	$\in \mathbb{R}^{n_x}$ virtual displacement of the endeffector pose.
$\delta\mathbf{q}$	$\in \mathbb{R}^{n_q}$ virtual displacement of the cables, compliant with the constraints.
$\delta\boldsymbol{\xi}$	$\in \mathbb{R}^{n_q}$ virtual displacement of the motor angles, compliant w. constraints.

$\delta W_{\mathbf{f}}$	virtual work done by the endeffector wrench $\mathbf{f}$.
$\delta W_{\boldsymbol{\tau}}$	virtual work done by the cable forces $\boldsymbol{\tau}$.
θ	parameter for the involute curve.
θ_0	parameter for the involute curve in the reference pose.
θ^*	solution for the involute parameter in the forward kinematics.
$\hat{\theta}$	approximate solution for the involute parameter in the forward kinematics.
$\boldsymbol{\theta}_e$	$\in \mathbb{R}^{n_q+1}$ vector of extended involute parameters.
$\boldsymbol{\theta}_e^0$	$\in \mathbb{R}^{n_q+1}$ initial guess for the extended involute parameters.
$\boldsymbol{\theta}_e^*$	$\in \mathbb{R}^{n_q+1}$ exact solution for the extended vector of involute parameters.
$\hat{\boldsymbol{\theta}}_e$	$\in \mathbb{R}^{n_q+1}$ approximate solution for the extended involute parameters.
β	polar coordinate angle for the involute curve.
β_0	polar coordinate angle for the involute curve in the reference pose.
β_{A0}	polar coordinate angle for point A in the reference pose.
α_0	rotation angle of the involute base point in the reference pose.
$\mathbf{u}$	motor voltage space vector.
$\mathbf{i}$	motor current space vector.
T	motor torque.
$\mathbf{T}$	$\in \mathbb{R}^{n_q}$ vector of motor torques.
ξ	motor angle.
$\boldsymbol{\xi}$	vector of motor angles.
p_s	pitch of the cable spool.
r_s	radius of the cable spool.
ν_{w}	transmission ratio of the winch mechanism.
l_p	distance between cable spool and guiding pulley.
α_p	cable angle in the winch mechanism.
I_{w}	mass moment of inertia of the winch system..
$I_{z,\mathrm{EE}}$	mass moment of inertia of the EE around the z-axis.

1 Introduction

Due to the high and increasing demand for a cost-effective, flexible and fast production of goods, the number of industrial robots deployed worldwide has been steadily increasing in the past years [1]. In 2021, the number of industrial robots in operation reached 3.4 million and is still expected to grow steadily in all major markets [2]. Due to various emerging trends, the demand for robotics in the logistics and warehouse sector has been growing especially quickly in the recent years and the market for warehouse robotics is expected to double until 2030 [3].

These recent developments create a high demand for industrial robots which are capable of very fast and dynamic motion as well as manipulators which feature large and extensible workspaces. Due to their structure, parallel kinematic robots are generally superior to serial kinematic robots in terms of low inertia and high ratio of payload to moving mass and can thus be used for tasks with the most demanding dynamic requirements. A special type are cable-driven parallel robots (CDPRs), where the end-effector platform (EE) is suspended by cables instead of rigid links [4]. This allows the robot to access very large workspaces and enables high flexibility in the deployment of the robot. However, because cables can only exert pulling forces on the EE, additional challenges in the robot design and control are introduced which make CDPRs an active field of research [5]. In particular, planar CDPRs, characterized by two translational degrees of freedom, are employed in a wide field of applications. Among them are storage and retrieval systems [6], laser engraving [7] and exoskeletons for limb rehabilitation [8]. Even systems without active control, where the trajectory of the EE is defined by non-cirular pulleys, are used for performing repeating haulage tasks [9].

In many designs of planar CDPRs, the pose of the EE is limited in the rotation angle. This maximum rotation angle is defined by kinematic constraints such as collisions of the cables and depends on the position of the EE [10]. A rotation of the EE is required in many applications, e. g. for the construction of a rotary coordinate table. This is why significant research effort is dedicated to enlarging the rotation angle of the EE of CDPRs.

In this thesis, a novel kinematic structure of a planar CDPR is studied which allows for arbitrary rotation of the EE. By wrapping the cables around a circular fixture attached to the EE, simultaneous rotation and translation can be enabled. This results in a mechanically simple and robust CDPR design without auxiliary moving parts. Thus, the robot is simple and inexpensive to manufacture and to maintain. The limits for the rotational degree of freedom are pre-defined by the number of turns around the EE but can be arbitrarily chosen. In the present work, the kinematic structure of a novel class of CDPRs is investigated and all different possible cable winding configurations are considered and classified. The kinematics of the robot are studied and solutions for both the inverse- as well as the forward kinematic problem are presented. Based on the kinematics of the robot, a dynamic kinetic robot model is derived. The workspace of

the CDPR concept for different numbers of cables and different cable configurations is analyzed using different quality criteria. Based on the results, a suitable candidate for a hardware prototype is selected. Finally, a prototype robot is constructed and the previous theoretical results are experimentally validated on the hardware prototype.

Parts of this thesis have been published in [11]. An upcoming master's thesis will extend the present work by designing and implementing a control strategy for the CDPR prototype. Using a dartboard mounted at the EE and a camera tracking system, the resulting control system will be capable of catching a flying dart thrown by a human such that the dart hits any desired field on the dartboard. Thus, a technology demonstrator will be created which showcases the potential and capabilities of the novel CDPR design.

1.1 Literature review

The aim of this section is to provide an overview of existing approaches, which can be found in the literature, to achieve large rotations in a CDPR. An extensive study of the possible rotation angle of the EE of a CDPR is performed by Reddy [12]. To extend the maximum rotation angle of the EE, Reddy et al. [13] propose an approach using a spindle mounted on the EE of a conventional planar CDPR which performs translational movement. The spindle provides additional rotation and is actuated by a mechanism consisting of a spring, a winch, and an additional cable.

Miermeister and Pott [14] proposed a similar approach for a spatial CDPR. Here, multiple platforms are individually actuated by cables and joined via a crank mechanism as illustrated in Figure 1.1. By coordinating the movement of the platforms, the crank

(a) 3D model of the crank mechanism. (b) Kinematic model.
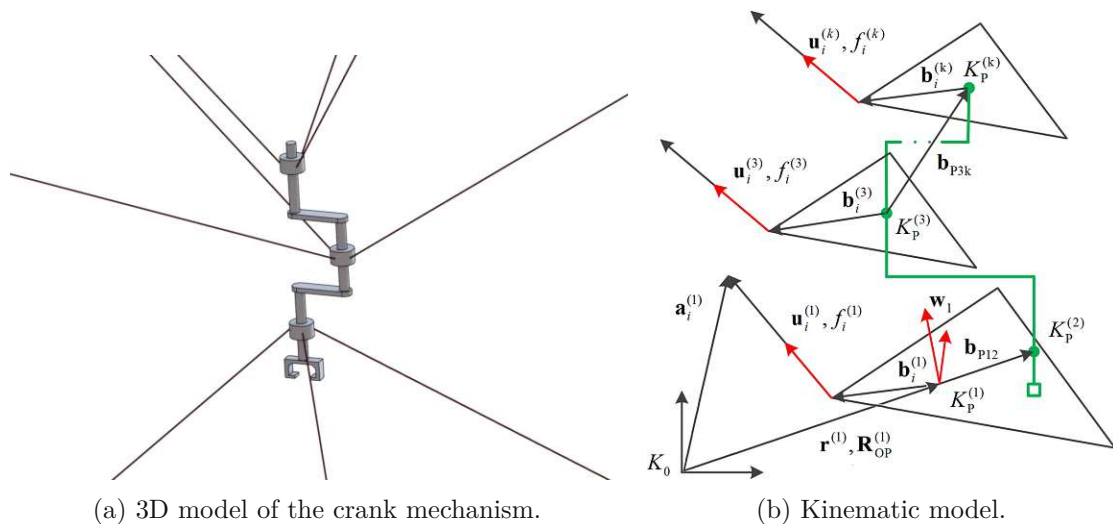
Figure 1.1: CDPR design proposed by Miermeister and Pott [14].

can be turned and an endless rotation angle of the EE can be achieved.

Hirosato and Harada [15] studied a planar design, where a pentagonal EE houses a spindle. The EE is driven by a cable which is fixed on the EE in combination with two cable loops, which are connected to the spindle and form rotational pairs. Each rotational

pair is wound around the spindle inside the pentagonal EE and is actuated by a pair of winches. To facilitate translational movement, the rotational pairs must change in length. This is enabled by adding a cable reservoir which is tensioned via a spring and stores the excess cable in the loop. The structure of the pentagonal robot *SEIMEI* by Hirosato and Harada is shown in Figure 1.2.
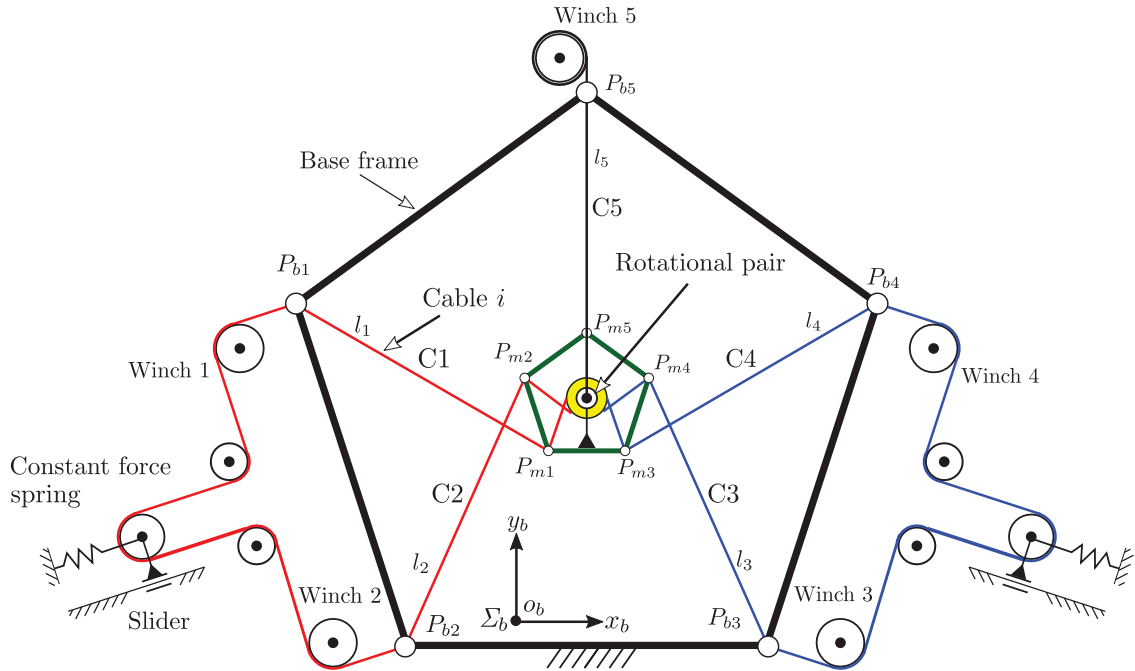
Figure 1.2: *SEIMEI* planar CDPR featuring endless rotation [15].

These approaches found in the literature introduce a significant additional mechanical complexity to the CDPR to extend the rotational range of the EE. To the best of the authors knowledge, there exist no other approaches which systematically combine arbitrarily large rotation and translational movement without adding weight, complexity or moving parts to the EE.

To analyze the capability of a robot to achieve a manipulation task within the workspace, many manipulability indices have been proposed in the literature, see, e.g., [4, 16]. The well-known manipulability measure quantifies a balance between achievable twists and wrenches of the EE, see [17]. For CDPRs, the requirement of a minimal tension in all cables leads to the notion of the wrench-closure workspace and, when problem-specific wrench directions and torque limits are considered, to the so-called wrench-feasible workspace, see [18–20]. These workspace definitions, however, do not provide information about the quality of their interior. In [16], it is shown that the manipulability is no intrinsic property of a kinematic structure and hence a suitable measure has to be chosen to address a specific problem.

1.2 Structure of the thesis

In Chapter 2, the mechanical design of the proposed planar CDPR concept is presented and explained in detail. First, in Section 2.1 some design considerations are investigated. Based on Burnside's Lemma known from group theory, the number of all possible unique cable configurations is derived and calculated in Section 2.2.

Consecutively, in Chapter 3 the kinematic structure is studied and the inverse kinematics are derived for the CDPR. For this, the inverse kinematic problem is formulated and all the basic modeling assumptions are introduced in Section 3.1. The CDPR geometry is studied in order to derive the inverse kinematic transformation function in Section 3.2. The differential kinematics are briefly discussed and the Jacobian Matrix is derived in Section 3.3, which relates forces and velocities of the cables to the forces and velocities of the EE.

Chapter 4 deals with the forward kinematics of the novel CDPR. The forward kinematic problem is introduced and discussed in Section 4.1. A solution approach for the forward kinematics is presented in Section 4.2. Simulations concerning the convergence behavior of the forward kinematics solution are presented in Section 4.4 for different CDPR designs.

In Chapter 5, the workspace of different CDPR designs is examined and evaluated. For this, a classical manipulability measure from the literature is used in Section 5.1. Because the manipulability measure shows some weaknesses and drawbacks for CDPRs, the *force efficiency* is employed as another quality measure in Section 5.2. The force efficiency in different directions is computed for different robot designs. Finally, in Section 5.3 the possibility of using alternative configurations with uneven numbers of cables is analyzed and discussed.

Based on the inverse kinematics and the Jacobian matrix, a dynamic model of the CDPR is developed in Chapter 6. The winch mechanics are described in Section 6.2 and the equations of motions are derived using the Newton-Euler equations in Section 6.3.

A controller for the CDPR is designed and implemented on a real-time computer system in Chapter 7. The controller will be further elaborated and studied in an upcoming master's thesis.

The novel CDPR concept is validated by realizing a hardware prototype, which is presented in Chapter 8. First the experimental setup is briefly outlined and introduced in Section 8.1. Using a commercial motion tracking system based on infrared cameras, the forward kinematics positioning accuracy is evaluated in Section 8.2. The force efficiency measure, discussed in Section 5.2, is experimentally validated for a given task in Section 8.3. Finally, the achievable dynamic positioning performance is assessed in Section 8.4 for both translational and rotational motion.

The thesis ends with a summary of the findings and an outlook on possible extensions and improvements in Chapter 9. Additional derivations and a list of parameter values of the robot prototype are provided in Appendix A.

2 Mechanical Design

The pose $\mathbf{x}$ of the EE of a planar robot is fully defined by the translational positions x_C and y_C of the EE centerpoint and its rotation angle φ. Thus, the pose $\mathbf{x}$ in matrix notation reads as

$$\mathbf{x} = \begin{bmatrix} x_C & y_C & \varphi \end{bmatrix}^{\mathrm{T}}. \tag{2.1}$$

For a CDPR, the joint space is parameterized by the length of the cables which connect the EE to the rigid frame. The number of cables n_q and consequently the necessary winches to actuate these cables, is an open design parameter. For a planar robot with $n_x = 3$ degrees of freedom (DOFs), a minimum of $n_q = n_x + 1 = 4$ cables is necessary to completely restrain the robot and guarantee that all cables remain under tension without relying on external forces such as gravity. For any larger number $n_q > n_x + 1$ of cables, the resulting robot is called redundantly restrained and the degree of redundancy increases with an increasing number of cables n_q [21]. In general, increasing n_q increases the complexity and cost of the robot. At the same time, increasing n_q causes more cables to contribute to the EE motion and thus increases the stiffness and manipulation capabilities of the CDPR. To compare different robot designs and geometries in a meaningful way, it is assumed in the following without loss of generality that the winches are placed equally spaced on a circle with radius r_{w}, where the center of the circle defines the origin of the workspace. In Figure 2.1(a), the kinematic diagram of a conventional planar 4-cable

(a) Conventional CDPR. (b) Proposed CDPR. (c) Vertical offset.
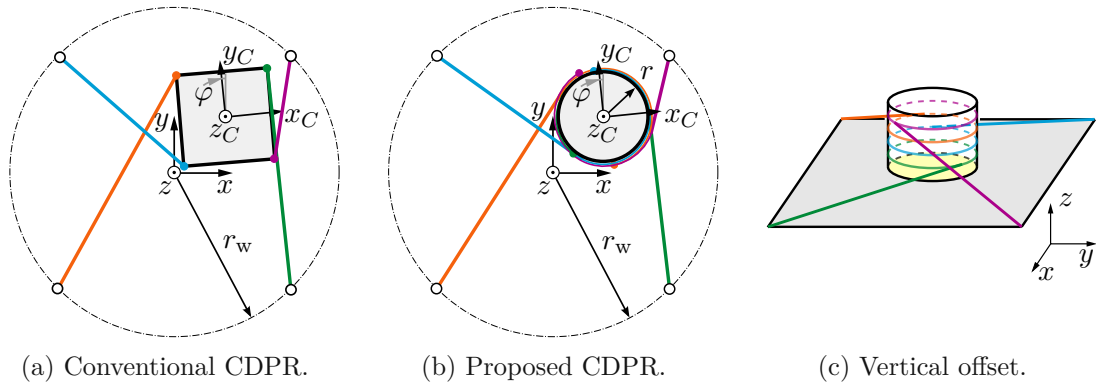
Figure 2.1: Kinematic diagram of (a) a conventional CDPR, (b) the proposed CDPR design and (c) the vertical displacement of the cables in the guiding grooves.

CDPR is shown. The EE collides with a cable if φ exceeds a lower or upper limit. This constrains the available workspace. The limits depend not only on the geometry of the frame and the EE, but also on the EE position and are not trivial to compute [10].

2.1 Circular end effector

A collision between the EE and the cables can be avoided when the EE is designed in a circular shape with radius $r < r_w$, as shown in Figure 2.1(b). Here, the cable is wrapped (possibly more than once) around the EE and is fixed at the EE as depicted. Each cable is guided in a groove which is offset to the winches in z-direction (out-of-plane), consequently collisions of cables are avoided as illustrated in Figure 2.1(c). In order to block forces in z-direction and rotations around the x- and y-axes, the EE glides on a guiding surface, which is installed parallel to the xy-plane.

When a cable touching a convex surface is under tension, it leaves the surface in a direction tangential to the surface as shown in Figure 2.2. The angle between the normal on the tangent and the vertical axis is denoted γ.
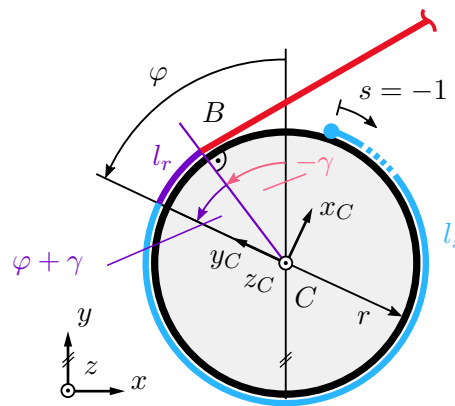
Figure 2.2: Circular EE wrapped by a cable.

It is possible to wrap the cable clockwise (CW) or counterclockwise (CCW) around the EE, which is indicated by the wrapping direction $s = -1$ or $s = 1$, respectively.

The length l' of the cable in contact with the EE can be partitioned into a part which depends on φ in the form

$$l_r = -sr(\varphi + \gamma) \tag{2.2}$$

and a spare length l_s in the form

$$l' = l_r + l_s \,, \tag{2.3}$$

see Figure 2.2. The value of l_s defines the limits of φ. A possible range of $\varphi_{\min} < \varphi < \varphi_{\max}$ can be ensured in the whole workspace if the condition

$$l_s = r\left(\max(-\varphi_{\min}, \varphi_{\max}) + \frac{\pi}{2}\right) \tag{2.4}$$

is met when the EE is at the origin. The limits $\varphi_{\min}$ and $\varphi_{\max}$ are design variables and can be chosen arbitrarily. Note that $\varphi_{\max}$ is not limited to a full rotation.

The force transmitted by a cable also exerts a torque on the EE. To enable rotations in both directions, at least one cable has to be wrapped CW and at least one cable CCW, respectively. If the number of CW cables is equal to the number of CCW cables and they exert the same force, the torque around the z-axis vanishes. In the following, in

order to achieve forces of similar magnitude in the cables, only equal numbers of CW and CCW cables are considered. Consequently, n_q is an even number. The possibility of using asymmetric configurations with uneven numbers of cables is briefly discussed and investigated in Section 5.3, where the workspace of a design with $n_q = 5$ cables is studied.

2.2 Unique balanced cable configurations

Under the given constraints, two unique balanced cable configurations exist for the 4-cable CDPR, see Figure 2.3. It can be shown that all other balanced cable configurations may be achieved by a circular shifting of those two cable configurations.
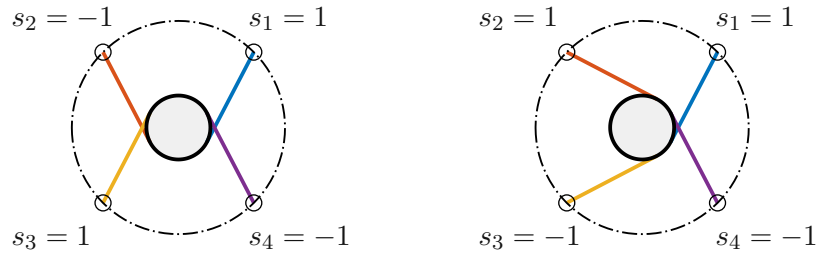
Figure 2.3: Possible cable configurations for $n_q = 4$.

To generally investigate the total number of unique balanced cable wrapping configurations, Burnside's lemma [22] known from group theory is applied in the following. For this, the set of admissible balanced configurations with an equal number of $s_i = 1$ and $s_i = -1$ can be defined as

$$\mathcal{B} = \left\{ \mathbf{s} \,|\, \sum_{i=1}^{n_q} s_i = 0 \right\} , \tag{2.5}$$

where $\mathbf{s} = [s_1, \ldots, s_{n_q}]^{\mathrm{T}}$ denotes the vector of wrapping directions which defines a configuration. Furthermore, let $\sigma_k(\mathbf{s})$ denote a circular shift of the configuration $\mathbf{s}$ by k places, which corresponds to a rotation. The circular shifting operator $\sigma_k(\mathbf{s})$ can be defined recursively in the form

$$\sigma_1\left(\begin{bmatrix} s_1 & \ldots & s_{n_q} \end{bmatrix}\right) = \begin{bmatrix} s_{n_q} & s_1 & \ldots & s_{n_q-1} \end{bmatrix} \tag{2.6}$$

$$\sigma_k(\mathbf{s}) = \sigma_1(\sigma_{k-1}(\mathbf{s})) . \tag{2.7}$$

All possible n_q circular shifts of a configuration $\mathbf{s} \in \mathcal{B}$ form a group denoted by $\mathcal{S}$. According to Burnside's lemma, the total number of unique orbits of the set $\mathcal{B}$ under the group $\mathcal{S}$ denoted as $|\mathcal{B}/\mathcal{S}|$ is

$$|\mathcal{B}/\mathcal{S}| = \frac{1}{|\mathcal{S}|} \sum_{\sigma_k \in \mathcal{S}} |\mathcal{B}^{\sigma_k}| , \tag{2.8}$$

where $|\cdot|$ denotes the cardinality of set $\cdot$ and $\mathcal{B}^{\sigma_k}$ is the set of all elements in $\mathcal{B}$ which are invariant with respect to the circular shift σ_k i.e.

$$\mathcal{B}^{\sigma_k} = \{\mathbf{s} \in \mathcal{B} \,|\, \sigma_k(\mathbf{s}) = \mathbf{s}\} . \tag{2.9}$$

In other words, $\mathcal{B}^{\sigma_k}$ contains all possible configurations which are unchanged with respect to k circular shifting operations.

To be invariant with respect to a circular shifting operation, a configuration **s** needs to be rotationally symmetric, which means that it needs to be composed of equal blocks of length k such that a circular shift by k places leaves the configuration unchanged. Thus, for a configuration to be invariant with respect to σ_k, its length n_q needs to be a multiple of k. Because of the constraint that the configuration must be an element of $\mathcal{B}$, all the equal sub-blocks of length k must also be elements of $\mathcal{B}$. In other words, if the configuration **s** should be balanced and if it is composed of identical blocks, then each block must also be balanced. Thus, k must be even and there are no invariant combinations for uneven block lengths that are elements of $\mathcal{B}$. Figure 2.4 shows an example for the symmetry of a balanced cable configuration with $n_q = 12$, with respect to the shifting operation σ_k for $k = 4$. For any even block length k, there are subsequently $\binom{k}{\frac{1}{2}k}$ possibilities for forming
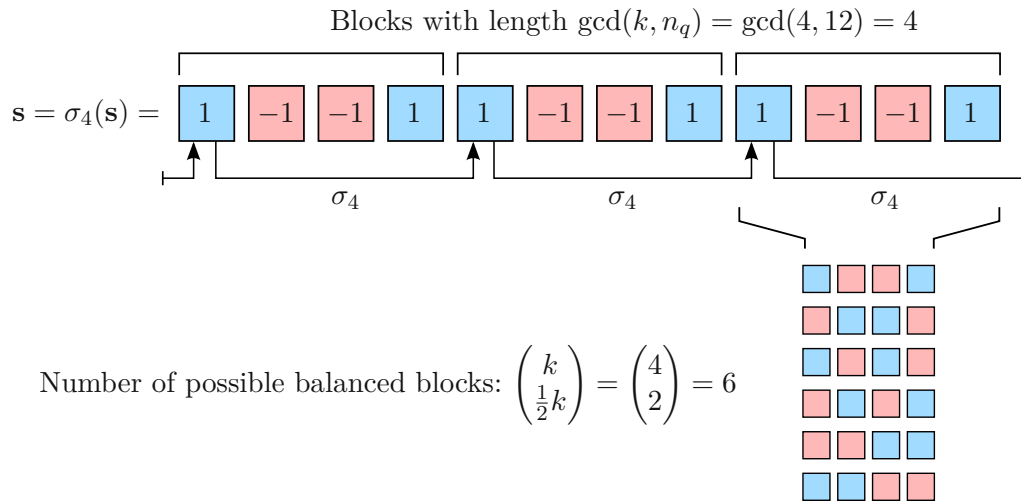
Figure 2.4: Example of rotational symmetry of a balanced cable configuration.

a balanced block. The longest possible block length for a configuration of n_q cables can be expressed using the *greatest common divisor* $\gcd(k, n_q)$. Additionally, all possible smaller blocks are shifted representations of the longest possible block and are thus contained within the largest possible block. Hence, for a shift of $k = 2i$, $i \in \mathbb{N}$ using the largest possible block size yields a total number of

$$|\mathcal{B}^{\sigma_k}| = \binom{\gcd(k, n_q)}{\frac{1}{2}\gcd(k, n_q)} \tag{2.10}$$

different configurations which are invariant with respect to k circular shifts.

Finally, by inserting Eq. (2.10) into Eq. (2.8), the general expression

$$|\mathcal{B}/\mathcal{S}| = \frac{1}{n_q} \sum_{i=1}^{\frac{n_q}{2}} \binom{\gcd(2i, n_q)}{\frac{1}{2}\gcd(2i, n_q)} \tag{2.11}$$

for the number of unique cable wrapping configurations for n_q cables is obtained.

3 Inverse kinematics

3.1 Inverse kinematics problem formulation

When solving the inverse kinematics problem of a CDPR, the EE pose $\mathbf{x}$ defined in Eq. (2.1) and the geometry of the robot are known and the cable lengths

$$\mathbf{q} = \begin{bmatrix} l_1 & l_2 & \dots & l_{n_q} \end{bmatrix}^{\mathrm{T}} \tag{3.1}$$

have to be calculated. Note that for a cable driven robot the vector $\mathbf{q}$, which combines the cable lengths l_i, is considered the joint vector. Hence the inverse kinematic transformation function $\boldsymbol{\phi}_{\mathrm{ik}} : \mathbb{R}^{n_x} \to \mathbb{R}^{n_q}$ can be expressed in the form

$$\mathbf{q} = \boldsymbol{\phi}_{\mathrm{ik}}(\mathbf{x}) \ . \tag{3.2}$$

Since a CDPR belongs to the very large class of so-called multi-body systems, there exist many model structures for describing such a system in the literature. In this work, the classical *standard kinematic model* for CDPRs is used which follows the conventions and assumptions of a multi-body system with rigid bodies and limp cables. The standard kinematic model is described and discussed in detail in [21]. The following assumptions are employed in the model:

- **Limp cables:** It is assumed that the cables can only pull and not push. There are no bending moments or forces other than pulling forces.

- **Inelastic cables:** The lengths of the cables do not change significantly depending on the tension applied. This assumption is critically evaluated and justified for the hardware prototype in Section 8.2.

- **Massless cables:** The cables are considered massless. Hence, cables suspended in the air form straight lines and there is no sag.

- **Rigid bodies:** All deformations in solid bodies are neglected and thus all bodies are assumed to be perfectly stiff.

- **Ideal cable guiding:** The dimensions of cable guides are small compared to the dimensions of the robot. Nonlinear effects in the cable guiding system are neglected (geometry, hysteresis, creep).

In Section 3.2, the cable geometry is used to derive the inverse kinematic transformation function $\boldsymbol{\phi}_{\mathrm{ik}}$ from Eq. (3.2). Subsequently in Section 3.3, the inverse kinematics Jacobian matrix $\mathbf{J}_{\mathrm{ik}}$, which relates the cable forces to the generalized forces acting on the EE in Cartesian space is derived from this relation. The Jacobian matrix provides the foundation for deriving a dynamical model in Chapter 6.

3.2 Inverse kinematic transformation

Let C denote the centerpoint of the circular EE, A the anchor point of a cable and B the point where the cable contacts the circular EE as depicted in Figure 3.1. The cable is guided in a groove which lies at a height h_C with respect to the xy-plane, and the distance to the winch anchor point is denoted by h_A, respectively. Projecting the anchor point A to the groove-plane, which is parallel to the xy-plane, yields point A', and projecting the center C onto the groove-plane yields C'. The tangential connection of the cable and the circular EE results in a right triangle formed by A', B and C'.
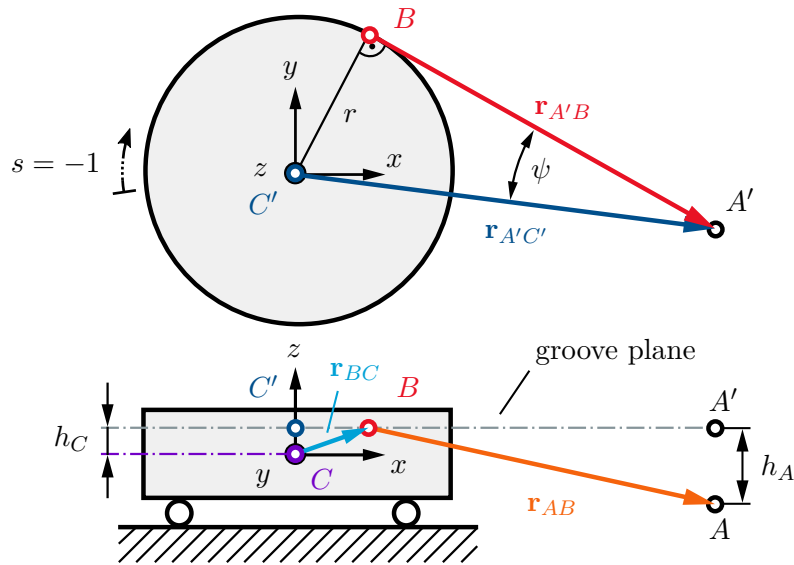
Figure 3.1: Cable geometry for the inverse kinematic problem.

The angle ψ shown in Figure 3.1 can be calculated in the form

$$\psi = \arcsin \frac{r}{\|\mathbf{r}_{A'C'}\|_2} \, . \tag{3.3}$$

The unit vector $\mathbf{e}_{A'B}$ pointing in the direction of the vector $\mathbf{r}_{A'B}$ is found by rotating the unit vector $\mathbf{e}_{A'C'}$, which points in the direction of the known vector $\mathbf{r}_{A'C'}$, by the angle ψ around the z-axis. This rotation can be performed using the rotation matrix $\mathbf{R}_z$

$$\mathbf{e}_{A'B} = \mathbf{R}_z(s\psi)\mathbf{e}_{A'C'} \, , \qquad \mathbf{R}_z(\alpha) = \begin{bmatrix} \cos s\psi & -\sin s\psi & 0 \\ \sin s\psi & \cos s\psi & 0 \\ 0 & 0 & 1 \end{bmatrix} , \tag{3.4}$$

where the direction of the rotation is defined by $s = \pm 1$ indicating CW or CCW windings as introduced in Section 2.1.

The length of $\mathbf{r}_{A'B}$ is obtained by using

$$\|\mathbf{r}_{A'B}\|_2 = \sqrt{\|\mathbf{r}_{A'C'}\|_2^2 - r^2} \, . \tag{3.5}$$

Combining Eqs. (3.4) and (3.5) leads to

$$\mathbf{r}_{A'B} = \mathbf{R}_z(s\psi)\mathbf{r}_{A'C'}\sqrt{1 - \frac{r^2}{\|\mathbf{r}_{A'C'}\|_2^2}} \, . \tag{3.6}$$

Finally, $\mathbf{r}_{AB}$ is found by respecting the offset between the anchor point and the groove in z-direction

$$\mathbf{r}_{AB} = \mathbf{r}_{A'B} - h_A \mathbf{e}_z \, . \tag{3.7}$$

Substituting Eq. (3.3) and Eq. 3.6 into Eq. (3.7) and rearranging terms, the vector $\mathbf{r}_{AB}$ can be written in the form

$$\mathbf{r}_{AB} = \begin{bmatrix} (1 - \rho^2)(x_A - x_C) - s\rho\sqrt{1 - \rho^2}(y_A - y_C) \\ (1 - \rho^2)(y_A - y_C) + s\rho\sqrt{1 - \rho^2}(x_A - x_C) \\ -h_A \end{bmatrix}, \qquad \rho = \frac{r}{\|\mathbf{r}_{A'C'}\|_2} \, . \tag{3.8}$$

The total cable length can be obtained as the sum of the free cable length $\|\mathbf{r}_{AB}\|_2$ suspended in the air and the cable length l' which is in contact with the EE disk

$$l = \|\mathbf{r}_{AB}\|_2 + l' \, , \tag{3.9}$$

where l' is a function of the angle γ, see Eqs. (2.2), (2.3) and Figure 2.2. The angle γ can be computed in the form

$$\gamma = \mathrm{atan2}\left(\mathbf{r}_{BC}^{\mathrm{T}}\mathbf{e}_x, \mathbf{r}_{BC}^{\mathrm{T}}\mathbf{e}_y\right) \, , \tag{3.10}$$

utilizing the four-quadrant arc-tangent function [4] and the vector $\mathbf{r}_{BC}$ from Eq. (3.12). This computation can be carried out for all n_q cables and combined to obtain the vector of joint coordinates $\mathbf{q}$.

As it can be seen from Eqs. (3.8) to (3.10), the computation of the joint coordinates $\mathbf{q}$ from the pose $\mathbf{x}$ is straightforward and computationally inexpensive. Furthermore, the number of operations is strictly deterministic and only standard arithmetic operations are required. Because each cable length only depends on the pose of the EE and since there is no coupling between the individual cable lengths, the inverse kinematics can be solved one cable at a time. Hence, the computational costs only scale linearly with the number of cables and the solution can be easily implemented on a real-time computer system, even for robots with a large number of cables n_q. The solution of the inverse kinematics is always unique and always exists, although the length $\mathbf{r}_{A'B}$ and the angle ψ can become complex when the winch lies inside the circular EE disk and thus $\|\mathbf{r}_{A'C'}\|_2 < r$. This case is considered physically impossible and meaningless.

3.3 Jacobian matrix of the inverse kinematics

To subsequently investigate the kinetics of the robot and develop a dynamical model, the kinematic transmission function of the cable forces to the generalized forces acting on the EE is required. In the context of robotics, the collection of generalized forces, i.e. all forces and torques acting on the EE in the task space, is called wrench [23]. The wrench $\mathbf{f} \in \mathbb{R}^{n_x}$

$$\mathbf{f} = \begin{bmatrix} F_x & F_y & M_z \end{bmatrix}^{\mathrm{T}} \tag{3.11}$$

is created as a result of the strictly positive cable forces $\boldsymbol{\tau} \in \left(\mathbb{R}^+\right)^{n_q}$ acting on the rigid EE disk. Each individual cable force τ_i acts in the direction of the vector $\mathbf{e}_{A_iB_i}$ and generates a torque around the centerpoint C with the lever arm

$$\mathbf{r}_{BC} = \mathbf{r}_{AC} - \mathbf{r}_{AB} \,. \tag{3.12}$$

Hence, the total forces and torques transmitted from the cables to the EE are given by

$$\begin{bmatrix} F_x \\ F_y \\ F_z \\ M_x \\ M_y \\ M_z \end{bmatrix} = \underbrace{\begin{bmatrix} \mathbf{e}_{A_1B_1} & \cdots & \mathbf{e}_{A_{n_q}B_{n_q}} \\ \mathbf{r}_{B_1C_1} \times \mathbf{e}_{A_1B_1} & \cdots & \mathbf{r}_{B_{n_q}C_{n_q}} \times \mathbf{e}_{A_{n_q}B_{n_q}} \end{bmatrix}}_{\mathbf{A}^{\mathrm{T}}(\mathbf{x})} \underbrace{\begin{bmatrix} \tau_1 \\ \vdots \\ \tau_{n_q} \end{bmatrix}}_{\boldsymbol{\tau}} , \tag{3.13}$$

where F_x, F_y and F_z denote the total resulting forces in the x, y and z-direction respectively and M_x, M_y and M_z denote the torques acting around the x, y and z-axis respectively. The resulting kinematic transmission matrix $\mathbf{A}^{\mathrm{T}} \in \mathbb{R}^{6 \times n_q}$ is called *structure matrix* in the literature [21] and relates the cable forces to the wrench applied to the EE. Note that $\mathbf{A}^{\mathrm{T}}$ is a function of the EE pose $\mathbf{x}$.

The relation of the cable forces $\boldsymbol{\tau}$ and the task-space wrench $\mathbf{f}$ can be formally derived using the *d'Alembert's principle* i.e. the principle of virtual work. According to d'Alembert's principle, the virtual work done by the constraint forces acting between EE disk and guiding plane is always zero [24]. Thus the virtual work done by the wrench $\delta W_{\mathbf{f}}$ must be equal to the virtual work done by the cable forces $\delta W_{\boldsymbol{\tau}}$

$$\begin{aligned} \delta W_{\mathbf{f}} &= \delta W_{\boldsymbol{\tau}} \\ \mathbf{f}^{\mathrm{T}}\delta\mathbf{x} &= -\boldsymbol{\tau}^{\mathrm{T}}\delta\mathbf{q} \end{aligned} \tag{3.14}$$

for any arbitrary virtual displacement $\delta\mathbf{q}$ and $\delta\mathbf{x}$ respectively, which is compliant with the constraints imposed by the guiding plane. The minus sign in Eq. (3.14) is a result of the convention that pulling cable forces are considered positive. In order to do positive work, a cable must contract ($\delta q_i < 0$) under a positive cable force ($\tau_i > 0$). The variation of Eq. (3.2) yields a relation of the virtual displacement of the EE $\delta\mathbf{x}$ and a virtual displacement of the cable lengths $\delta\mathbf{q}$ in the form

$$\delta\mathbf{q} = \frac{\partial\phi_{\mathrm{ik}}}{\partial\mathbf{x}}\delta\mathbf{x} \,. \tag{3.15}$$

Inserting Eq. (3.15) into Eq. (3.14) leads to the relation

$$\mathbf{f}^{\mathrm{T}}\delta\mathbf{x} = -\boldsymbol{\tau}^{\mathrm{T}}\underbrace{\frac{\partial\phi_{\mathrm{ik}}}{\partial\mathbf{x}}}_{\mathbf{J}_{\mathrm{ik}}(\mathbf{x})}\delta\mathbf{x} \,. \tag{3.16}$$

Here, $\mathbf{J}_{\mathrm{ik}} \in \mathbb{R}^{n_q \times n_x}$ is the so-called Jacobian matrix of the inverse kinematics [21] which is a function of the pose $\mathbf{x}$. Because the virtual displacement $\delta\mathbf{x}$ is arbitrary, Eq. (3.16) can be rewritten as

$$\mathbf{f} = -\mathbf{J}_{\mathrm{ik}}^{\mathrm{T}}\boldsymbol{\tau} \,. \tag{3.17}$$

Comparing the force transmission relations Eq. (3.13) and Eq. (3.17) reveals the direct connection between the structure matrix $\mathbf{A}^{\mathrm{T}}$ and the Jacobian $\mathbf{J}_{\mathrm{ik}}$ of the inverse kinematics, which can be expressed by

$$\mathbf{J}_{\mathrm{ik}}^{\mathrm{T}} = -\begin{bmatrix} 1 & 0 & 0 & 0 & 0 & 0 \\ 0 & 1 & 0 & 0 & 0 & 0 \\ 0 & 0 & 0 & 0 & 0 & 1 \end{bmatrix} \mathbf{A}^{\mathrm{T}} . \tag{3.18}$$

In other words, the constraints imposed by the guiding plane blocks the force F_z and the tilting torques M_x and M_y imposed on the EE by the cables. Thus, the corresponding columns of the structure matrix $\mathbf{A}^{\mathrm{T}}$ and the Jacobian $\mathbf{J}_{\mathrm{ik}}$ are identical but have opposite signs due to the convention that pulling cable forces are positive and contracting cables result in negative changes of the joint coordinates $\mathbf{q}$.

By definition, the Jacobian matrix of the inverse kinematics establishes the relation between the generalized EE velocity $\dot{\mathbf{x}}$ and the joint velocity $\dot{\mathbf{q}}$ in the form

$$\frac{\mathrm{d}\mathbf{q}(t)}{\mathrm{d}t} = \frac{\mathrm{d}\boldsymbol{\phi}_{\mathrm{ik}}(\mathbf{x}(t))}{\mathrm{d}t} = \underbrace{\frac{\partial \boldsymbol{\phi}_{\mathrm{ik}}}{\partial \mathbf{x}}}_{\mathbf{J}_{\mathrm{ik}}(\mathbf{x})} \frac{\mathrm{d}\mathbf{x}}{\mathrm{d}t}$$

$$\dot{\mathbf{q}} = \mathbf{J}_{\mathrm{ik}}\dot{\mathbf{x}} . \tag{3.19}$$

Note that $\mathbf{J}_{\mathrm{ik}}$ is in general a $n_q \times n_x$ matrix and for any over-constrained robot, in particular the present CDPR where $n_q > n_x$, the matrix is rectangular and cannot be inverted.

4 Forward kinematics

4.1 Forward kinematics problem formulation

In the forward kinematics problem, the cable lengths i. e. joint coordinates $\mathbf{q}$ are known and the pose $\mathbf{x}$ of the EE has to be calculated. Thus, the forward kinematics problem can be formulated as a transformation function $\phi_{\mathrm{fk}} : \mathbb{R}^{n_q} \to \mathbb{R}^{n_x}$ in the form

$$\mathbf{x} = \phi_{\mathrm{fk}}(\mathbf{q}) \ . \tag{4.1}$$

To find this function, the *standard model* for a CDPR is used and the same modelling assumptions as discussed in Section 3.1 are applied. In contrast to the inverse kinematics problem studied in Chapter 3, the forward kinematics problem of the present planar CDPR is over-constrained because the number of cables $n_q > n_x$ and hence the robot has to be kinematically over-constrained in order to guarantee tension in all cables. For parallel robots, where all the limbs of the robot are kinematically connected to the EE in parallel, the forward kinematics is in general much more complicated than the inverse kinematics [25]. It can be shown that for CDPRs, the inverse kinematic transformation function ϕ_{ik} always has a unique solution, but the forward kinematics transfer function ϕ_{fk} might have one, multiple, infinite or no solution for given joint coordinates $\mathbf{q}$ [21].

In particular, the presence of measurement errors in the joint coordinates can cause the forward kinematics to have no exact solution at all and thus approximate solutions $\hat{\phi}_{\mathrm{fk}}(\mathbf{q})$, e. g. in a least-squares sense, must be considered instead. The problem can be formulated as an optimization problem for an error measure $\varepsilon(\mathbf{q}, \hat{\mathbf{x}})$ such that

$$\hat{\phi}_{\mathrm{fk}}(\mathbf{q}) = \arg \min_{\hat{\mathbf{x}}} \quad \|\varepsilon(\mathbf{q}, \hat{\mathbf{x}})\|_2^2 \tag{4.2}$$

is fulfilled.

To be useful for controlling the robot in a practical implementation, special care must be taken that the forward kinematics solution satisfies the following requirements:

- **Real-time capability:** To implement an algorithm for the forward kinematics on a computer system, the worst-case computational time must be bounded and it must be sufficiently low to achieve practically useful cycle times.

- **Error detection:** If the algorithm fails to find a valid solution for the forward kinematics problem, the error must be detectable in order to guarantee safe operation.

- **Stable convergence:** The algorithm must converge to the same solution in a stable way without jumping back and forth between solutions, in case multiple solutions exist.

A more in-depth discussion on different approaches for solving the forward kinematics problem in a CDPR as well as the challenges and requirements can be found in [21].

4.2 Forward kinematics solution approach

In a first step in Section 4.2.1, only the planar geometry in the xy-plane is considered and all vertical displacements in z-direction are assumed to be zero, i.e. $h_A = h_C = 0$. For the sake of simplicity, this planar problem is analyzed first. Based on the geometric constraints, a solution for the forward kinematics problem is formulated as a nonlinear least-squares problem in Section 4.2.2. In Section 4.2.3, the solution is extended by taking the offsets in z-direction into account. Subsequently, the error introduced by the offsets in z-direction is analyzed and its significance is evaluated.

4.2.1 Planar geometry

To solve the forward kinematics problem, a mathematical formulation of the constraint imposed on the translational movement of the EE in the xy-plane is sought. First, the constraint imposed by a single cable is formulated and then the constraints of all n_q cables are combined to find the EE pose.

The EE can rotate around the z-axis and translate in the xy-plane independently. However, by considering these two types of motion separately, their relation with respect to the cable length l and the rotation angle φ can be analyzed. In the following, only the planar geometry is considered. Thus, the point A', which is the projection of point A onto the groove plane as shown in Figure 3.1, is used instead of A. Similarly, the point C' is used instead of C. Combining the relations from Eqs. (2.2), (2.3) and (3.9) yields the expression

$$l = \|\mathbf{r}_{A'B}\|_2 + l_s - sr\gamma - sr\varphi \ . \tag{4.3}$$

In a first step, consider keeping φ and l fixed while moving the EE translationally. This causes the cable to constrain the motion of the EE to a curve of admissible positions, as visualized in Figure 4.1. The curve of admissible positions, which is traced by the centerpoint C' as the cable is wrapped around the circular EE, is called an *involute curve*.
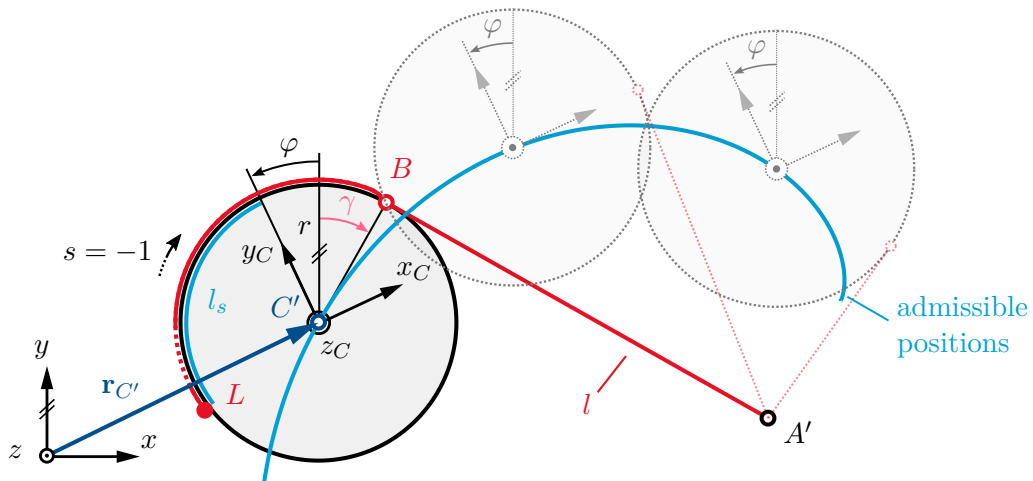
Figure 4.1: Admissible EE positions for constant φ and l.

Equation (4.3) shows that any change in the distance $\|\mathbf{r}_{A'B}\|_2$ is directly proportional to a change in the wrapping angle γ between the vertical and the tangent contact point B, when l and φ are fixed. Here, the spare cable length l_s is a constant parameter. It can be concluded, that the EE is constrained to a certain involute curve, which depends on the choice of l and φ. The aim is to find a mathematical formulation for all admissible EE positions as a function of l and φ.

In a second step, consider only rotating the EE by changing φ while keeping its position $\mathbf{r}_{C'}$ fixed. When the EE position $\mathbf{r}_{C'}$ is constant, the location of the cable contact point B must also be constant. As a result, the length $\|\mathbf{r}_{A'B}\|_2$ and the angle γ are constant as well, see Figure 4.1. Thus, Eq.(4.3) shows that the cable length l increases or decreases when changing φ, depending on the wrapping direction s. This is a result of the cable being wrapped around or unwrapped from the EE, respectively. However, while both l and φ change, the set of admissible poses remains unchanged in this case. Hence, it can be concluded, that the constraint determining the admissible EE positions must be a function of the quantity

$$l_{\varphi 0} = \|\mathbf{r}_{A'B}\|_2 + l_s - sr\gamma = l + sr\varphi \ . \tag{4.4}$$

In other words, if both l and φ change in such a way that $l_{\varphi 0}$ is unchanged, then the constraint determining the set of admissible EE positions $\mathbf{r}_{C'}$ in the xy-plane also remains unchanged. When comparing Eqs. (4.3) and (4.4) it can be seen that the length $l_{\varphi 0}$ can be interpreted as the cable length, which is obtained when rotating the EE such that $\varphi = 0$.

To find out how a single cable constrains the EE motion, consider disconnecting the cable from the winch at point A' and winding it fully onto the EE starting from its attachment point L until it contacts the EE at point E. This is visualized in Figure 4.2 where the dashed lines indicate intermediate positions of the cable when wrapping it around the EE. In the process of winding the cable onto the circular EE, its endpoint
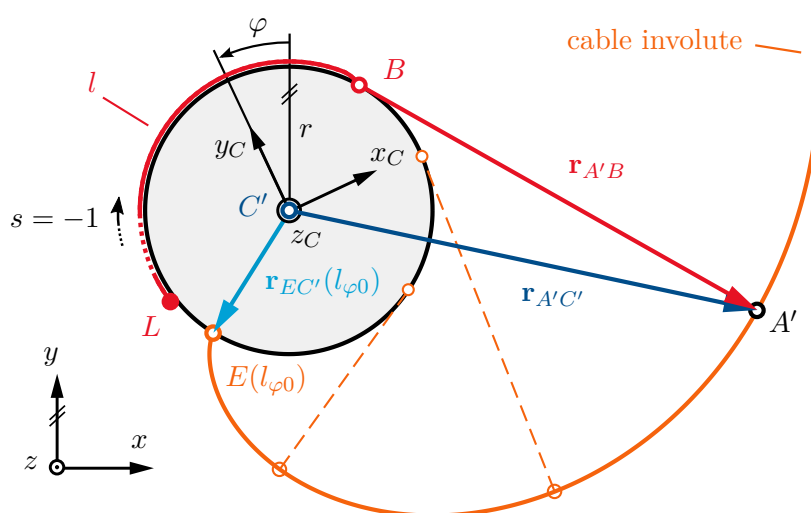
Figure 4.2: Geometry for the forward kinematics.

traces an *involute curve* which will be called the *cable involute* subsequently. Note that the cable involute always has the same shape which is fully defined by the radius r of the circular EE. This radius is called the *generating base-radius* of the involute. Only the position of the so-called base-point E on the EE depends on the length $l_{\varphi 0}$. This circumstance can be used to find a parameterization for all points on the cable involute.

To derive such a parameterization, a generic involute curve with the same base-radius r can be parameterized first and then rotated accordingly such that it matches the cable involute. For this, consider the base-point Q located at $[r, 0, 0]^\mathrm{T}$ as a starting point for the involute curve and the generic point P which lies on the involute. The geometry of the generic involute curve is visualized in Figure 4.3.
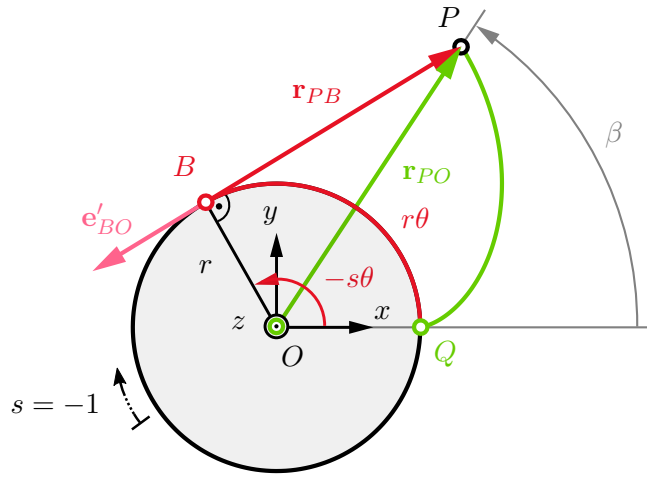
Figure 4.3: Involute curve geometry.

The involute can be parameterized by finding an expression for the location of $P(\theta)$ as a function of the curve parameter θ. Because P is connected to the base-circle via a cable, the corresponding contact point B between cable and circle can be utilized to construct the location of point P. To achieve this, the contact point B on the circle can be parameterized using the angle θ, respecting the winding direction which is given by $s \in \{-1, 1\}$. This yields the vector $\mathbf{r}_{BO}$ and its tangent unit vector $\mathbf{e}'_{BO}$ in the form

$$\mathbf{r}_{BO}(\theta) = r \begin{bmatrix} \cos(-s\theta) \\ \sin(-s\theta) \\ 0 \end{bmatrix} = r \begin{bmatrix} \cos(s\theta) \\ -\sin(s\theta) \\ 0 \end{bmatrix} \tag{4.5}$$

$$\mathbf{e}'_{BO}(\theta) = \frac{\mathbf{r}'_{BO}(\theta)}{\|\mathbf{r}'_{BO}(\theta)\|_2} = \begin{bmatrix} -s\sin(s\theta) \\ -s\cos(s\theta) \\ 0 \end{bmatrix}. \tag{4.6}$$

By following the tangent direction $\mathbf{e}'_{BO}$ and applying the unwound cable length $r\theta$, the vector $\mathbf{r}_{PB}$ is obtained as

$$\mathbf{r}_{PB}(\theta) = r\theta \begin{bmatrix} s\sin(s\theta) \\ s\cos(s\theta) \\ 0 \end{bmatrix}. \tag{4.7}$$

Finally, a parametrization for the involute curve is found by

$$\mathbf{r}_{PO}(\theta) = \mathbf{r}_{BO} + \mathbf{r}_{PB} = r \begin{bmatrix} \cos{(s\theta)} + s\theta\sin{(s\theta)} \\ -\sin{(s\theta)} + s\theta\cos{(s\theta)} \\ 0 \end{bmatrix} . \tag{4.8}$$

This formulation in Cartesian coordinates is useful for later combining multiple involute curves in a common Cartesian reference frame. However, the shape of the generic involute curve can be alternatively represented in a polar coordinate system centered at point O, which marks the center of the base-circle. In this polar reference frame, the generic involute can be represented using $\|\mathbf{r}_{PO}\|_2$ and β which are defined by the relations

$$\|\mathbf{r}_{PO}\|_2 = r\sqrt{1+\theta^2} \tag{4.9}$$

$$\tan{(\theta - \beta)} = \frac{\|\mathbf{r}_{PB}\|_2}{r} = \theta \tag{4.10}$$
$$\beta = \theta - \arctan{\theta} .$$

The relations from Eqs. (4.9) and (4.10) are useful for converting different quantities within an involute but less convenient for combining multiple involute curves.

In order to find an expression for the cable involute shown in Figure 4.2, the generic involute $\mathbf{r}_{PO}(\theta)$ must be rotated until its base point Q coincides with $E(l_{\varphi 0})$. In a practical robot implementation, the total cable length l is not measured directly but instead inferred from the winch position. Thus, it is expedient to decompose l into a reference length l_0 which is calibrated once and a change from that length Δl which is measured by the winches such that

$$l = l_0 + \Delta l . \tag{4.11}$$

In the following, the required rotation angle for rotating the generic involute such that it matches the cable involute is calculated in two steps. First, the rotation angle corresponding to the reference length l_0 is determined. Second, the additional rotation from this reference configuration, caused by a change of Δl, is computed.

For the first step, let $\mathbf{x}_0 = [x_0, y_0, 0]^{\mathrm{T}}$ denote the reference pose for which the cable length equals l_0. In this reference pose, the EE centerpoint C' is located at $\mathbf{r}_0$. The required rotation angle of the generic involute to obtain the reference involute shown in Figure 4.4 is denoted α_0. The angle α_0 can be found by calculating the angle between the horizontal and the point $E(l_0)$ as illustrated in Figure 4.4. To find the value of α_0 for a reference pose $\mathbf{x}_0$, it can be expressed as

$$\alpha_0 = \beta_{A0} - \beta_0 , \tag{4.12}$$

using the auxiliary polar angles β_{A0} and β_0 as shown in Figure 4.4. Since the robot geometry and the reference position $\mathbf{r}_0$ are known, the angle β_{A0} is known and θ_0 can be calculated using the relation from Eq. (4.9). Equation (4.10) yields the angle β_0 which can be used in Eq. (4.12) to obtain α_0.

In the second step, the additional rotation of the reference involute, caused by the change in cable length Δl, is considered. The location of the base-point E on the circular
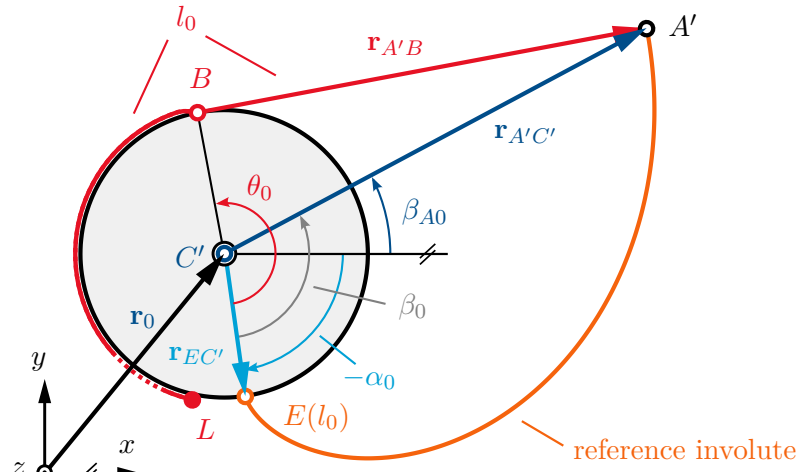
Figure 4.4: Involute in the reference position.

EE is determined by completely wrapping the cable around the EE in the winding direction given by s. Thus, any change Δl will cause the point E to rotate by the angle $s\frac{\Delta l}{r}$ on the circumference of the EE.

Finally, the previously derived components are combined and a parameterization for the cable involute is obtained by rotating the generic involute from Figure 4.3 around the z-axis. To arrive at the reference configuration, a rotation by the angle α_0 from Eq. (4.12) is required. In addition, the change in cable lengths Δl corresponds to a rotation by $s\frac{\Delta l}{r}$. Finally, a change in φ is related to a rotation of $s\varphi$ as shown in Eq. (4.4). Combining these three rotation terms yields the expression

$$\mathbf{r}_{A'C'}(\theta, \Delta l, \varphi) = \mathbf{R}_z\left(\alpha_0 + s\frac{\Delta l}{r} + s\varphi\right)r\begin{bmatrix} \cos(s\theta) + s\theta\sin(s\theta) \\ -\sin(s\theta) + s\theta\cos(s\theta) \\ 0 \end{bmatrix} \quad (4.13)$$

for the cable involute. Here, the rotation matrix $\mathbf{R}_z(\cdot)$ from Eq. (3.4) is used. With Eq. (4.13) an expression which formulates the constraint imposed by a single cable is found. This constraint parameterizes all admissible EE positions using the parameter θ. These admissible EE positions can be formulated explicitly in the form

$$\mathbf{r}_{C'}(\theta, \Delta l, \varphi) = \mathbf{r}_{A'} - \mathbf{r}_{A'C'}(\theta, \Delta l, \varphi)\,, \quad (4.14)$$

using the known winch position $\mathbf{r}_{A'}$. This results in an involute on which the EE can lie, subsequently called the *constraint involute*. The constraint in the *xy*-plane is visualized in Figure 4.5. Either changing the angle φ or changing the length Δl corresponds to a change of $l_{\varphi 0}$, see Eqs. (4.4) and (4.11). As a consequence, the base-point of the constraint-involute given by $\mathbf{r}_{EC'}$ rotates on the base-circle. Figure 4.5 visualizes the base-circle of the constraint-involute using a dash-dotted line and intermediate positions of the EE centerpoint C' along the constraint-involute using dashed lines. The angle θ parameterizes all points which lie on the involute.
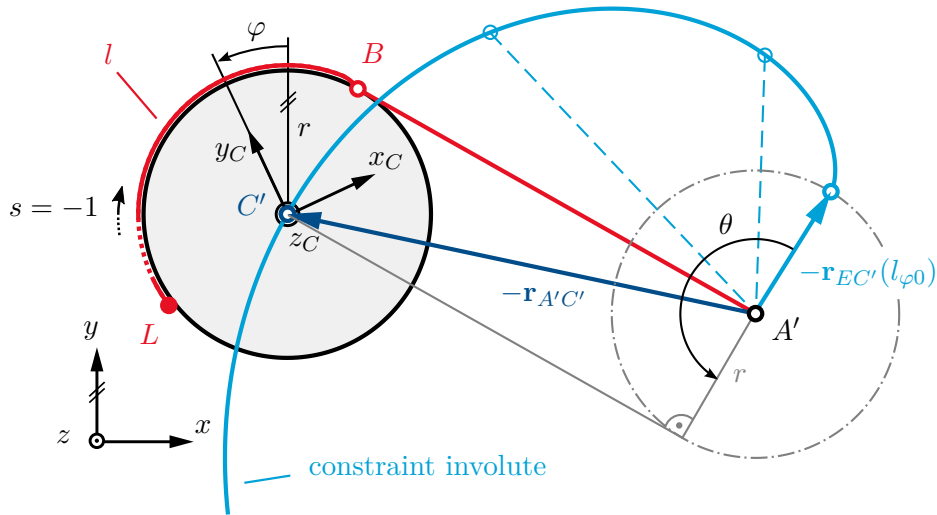
Figure 4.5: Constraint in the xy-plane imposed by one cable.

In other words, $\mathbf{r}_{C'}(\theta, \Delta l, \varphi)$ from Eq. (4.14) describes a family of involute curves. Each specific involute curve is parameterized by the curve parameter θ whereas the rotation of the individual involute curve is determined by the combination of Δl and φ.

4.2.2 Nonlinear least-squares problem

To find the EE pose, the constraints of all n_q cables must be combined i. e. the intersection of all constraint involutes $\mathbf{r}_{C'i}(\theta_i, q_i, \varphi)$ for $i = 1, \ldots, n_q$ given by Eq. (4.14) must be found. To gain a better understanding of the present situation, an example for $n_q = 4$ is shown in Figure 4.6. To facilitate translational movement of the board, the constraint involutes rotate around the winch locations A_i. Changing the cable lengths corresponds to rotating the respective constraint involute which causes the EE to move closer or further away due to the spiral shape of the constraint involute.

As discussed in Section 4.1, the joint coordinates i. e. the cable length differences Δl are subject to measurement errors. Hence, in general an exact solution, i. e. intersection of all n_q involute constraints, does not exist. Let

$$\boldsymbol{\theta}_e = \left[\theta_1, \ldots, \theta_{n_q}, \varphi\right]^{\mathrm{T}} \tag{4.15}$$

denote the extended vector of involute parameters for all constraint involutes. Solving the forward kinematics problem corresponds to finding the solution $\boldsymbol{\theta}_e^* = [\theta_1^*, \ldots, \theta_{n_q}^*, \varphi^*]^{\mathrm{T}}$ for the extended involute parameters which causes the points $\mathbf{r}_{C'i}(\theta_i^*, q_i, \varphi^*)$ to coincide. In this case, all constraints are satisfied and all constraint involutes intersect at a single point. This intersection can be written in the form

$$\mathbf{r}_{C'1}(\theta_1^*, q_1, \varphi^*) = \mathbf{r}_{C'2}(\theta_2^*, q_2, \varphi^*) = \cdots = \mathbf{r}_{C'n_q}(\theta_{n_q}^*, q_{n_q}, \varphi^*) . \tag{4.16}$$

The intersection of all n_q constraint involutes can be rewritten as $n_q - 1$ equations for the x-coordinates and $n_q - 1$ equations for the y-coordinates which yields a total number of
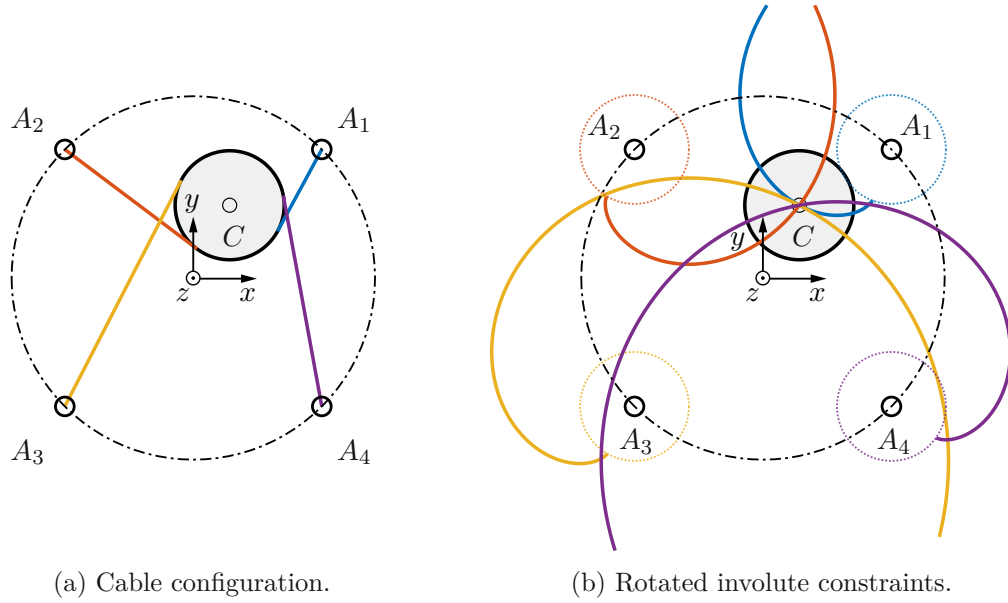
(a) Cable configuration.

(b) Rotated involute constraints.

Figure 4.6: Constraints imposed by the cables.

$2(n_q - 1)$ scalar equations. The unknown vector $\boldsymbol{\theta}_e^*$ contains $n_q + 1$ variables and thus the system of equations is over-determined for $n_q > n_x = 3$.

Although in general an exact solution $\boldsymbol{\theta}_e^*$ cannot be found for the over-determined system due to measurement errors, finding an approximate solution $\hat{\boldsymbol{\theta}}_e$ is of interest. Using the coordinates of the mean point of the involute constraints

$$\bar{\mathbf{r}}_{C'}(\boldsymbol{\theta}_e, \mathbf{q}) = \frac{1}{n_q} \sum_{i=1}^{n_q} \mathbf{r}_{C'i}(\theta_i, q_i, \varphi) \ , \tag{4.17}$$

the approximate solution for the involute parameters can be formulated as a nonlinear least-squares problem in the form

$$\hat{\boldsymbol{\theta}}_e = \arg \min_{\boldsymbol{\theta}_e} \quad \sum_{i=1}^{n_q} \| \bar{\mathbf{r}}_{C'}(\boldsymbol{\theta}_e, \mathbf{q}) - \mathbf{r}_{C'i}(\theta_i, q_i, \varphi) \|_2^2 \ . \tag{4.18}$$

Note that the chosen formulation of the optimization problem Eq. (4.18) minimizes the variance of the points $\mathbf{r}_{C'i}$ in the xy-plane.

Applying the optimal solution $\hat{\boldsymbol{\theta}}_e(\mathbf{q})$, the mean involute constraint point $\bar{\mathbf{r}}_{C'}(\hat{\boldsymbol{\theta}}_e, \mathbf{q})$ can be computed using Eq. (4.17) and then utilized to obtain the EE pose in the form

$$\hat{\mathbf{x}}(\mathbf{q}) = \begin{bmatrix} \begin{bmatrix} 1 & 0 & 0 \\ 0 & 1 & 0 \end{bmatrix} \bar{\mathbf{r}}_{C'}(\hat{\boldsymbol{\theta}}_e, \mathbf{q}) \\ \hat{\varphi} \end{bmatrix} \ . \tag{4.19}$$

Thus, the forward kinematics problem is solved.

The nonlinear least-squares problem in Eq. (4.18) is a $n_q + 1$ dimensional unconstrained optimization problem, which can be solved using a variety of algorithms for which numerical

libraries are readily available in many programming languages. To find the optimal solution via a numerical iterative scheme, a sufficiently close initial estimate $\boldsymbol{\theta}_e^0$ is required for which the optimization problem is locally convex. If the initial guess is too far away from the global optimum or the cost-function is locally non-convex in the vicinity of the starting point, the algorithm might diverge or converge to a local optimum which is not the desired solution for the forward kinematics problem.

So far, a forward kinematics solution algorithm for computing the approximate pose $\hat{\mathbf{x}}$ from the cable lengths $\mathbf{q}$ was derived. For this, the constraints imposed by the cables were formulated and then combined in a nonlinear least-squares problem, to find an approximation of the EE pose even in the presence of measurement errors. Until now, the problem was treated as a planar problem in the xy-plane only. In the following Section 4.2.3, the offsets in z-direction are taken into account. Thereafter in Section 4.3, a systematic method to find an initial estimate for the EE pose is proposed, which can be converted to a suitable initial estimate $\boldsymbol{\theta}_e^0$ for the optimization variables. A robust and widely used algorithm for solving nonlinear least-squares problems is the Levenberg-Marquardt method. Using this method, the convergence behavior of the outlined forward kinematics solution approach is studied in Section 4.4.

4.2.3 3D geometry extension

In this section, the offsets h_A in z-direction shown in Figure 4.7 are taken into account and the forward kinematics are adapted accordingly. The offsets are introduced because the cables are utilized to pull the EE towards the guiding surface, to ensure stable and reliable contact and guidance.

Due to these offsets, the involute curves arising in the forward kinematics problem are skewed in z-direction. Each cable, which forms an involute curve when being rolled onto the EE disk, must additionally overcome the distance h_A in z-direction as depicted in Figure 4.7. As a result, the distance in the groove plane $\mathbf{r}_{A'B}$ is modified to $\sqrt{r^2\theta^2 - h_A^2}$
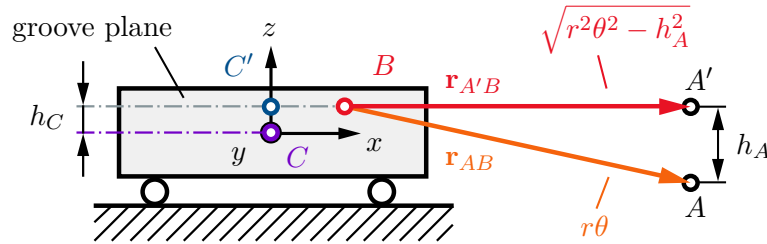
Figure 4.7: Offset in z-direction.

and the involute shape is skewed. Respecting the offsets h_A and h_C, the cable involute from Eq. (4.13) can be modified to obtain a curve which is subsequently called *modified cable involute*

$$\mathbf{r}_{AC}(\theta, \Delta l, \varphi) = \mathbf{R}_z\left(\alpha_0 + s\frac{\Delta l}{r} + s\varphi\right) r \begin{bmatrix} \cos(s\theta) + s\sqrt{\theta^2 - \left(\frac{h_A}{r}\right)^2}\sin(s\theta) \\ -\sin(s\theta) + s\sqrt{\theta^2 - \left(\frac{h_A}{r}\right)^2}\cos(s\theta) \\ h_C - h_A \end{bmatrix} \tag{4.20}$$

for $\theta > \frac{h_A}{r}$. Here, the rotation matrix $\mathbf{R}_z(\cdot)$ from Eq. (3.4) is used. The modified terms are highlighted in red color. Following the same steps as for the planar case, a modified constraint involute on which the point C must lie can be derived using Eq. (4.20) in the form

$$\mathbf{r}_C(\theta, \Delta l, \varphi) = \mathbf{r}_A - \mathbf{r}_{AC}(\theta, \Delta l, \varphi) \ . \tag{4.21}$$

A comparison of the constraint involute for the planar case $\mathbf{r}_{C'}(\theta, \Delta l, \varphi)$ and the modified constraint involute $\mathbf{r}_C(\theta, \Delta l, \varphi)$ respecting the offsets is visualized in Figure 4.8 for the parameter ratio $\frac{h_A}{r} = \frac{1}{3}$. Intuitively, the offset h_A has the greatest influence on the shape
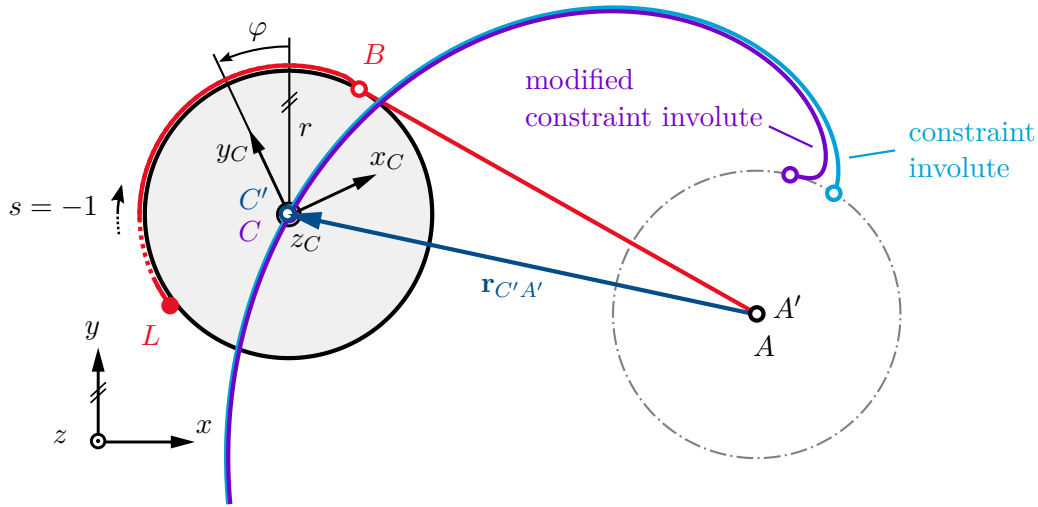
Figure 4.8: Comparison of the modified and planar constraint involutes.

of the modified involute when the EE is close to the winch i. e. the distance $\|\mathbf{r}_{C'A'}\|_2$ is small. For large distances from the winch, i. e. $\theta \to \infty$, the error between the modified constraint involute and the constraint involute for the planar case tends to zero.

To quantify the error introduced by neglecting the offset h_A in the forward kinematics, the distance in the xy-plane between the constraint involute and the modified constraint involute is considered. Because the z-coordinate of the EE is prescribed by the guiding plane, only the error in the xy-plane is of interest. Hence, the position error $e_{C,xy}$ is defined in the form

$$e_{C,xy} = \left\| \begin{bmatrix} 1 & 0 & 0 \\ 0 & 1 & 0 \end{bmatrix} (\mathbf{r}_{AC} - \mathbf{r}_{A'C'}) \right\|_2 \ . \tag{4.22}$$

This error in the xy-plane directly impacts the solution of the forward kinematics and must be sufficiently small to justify neglecting the offset h_A. Combining Eqs. (4.13) and (4.20) and considering that $s^2 = 1$, the involute position error $e_{C,xy}$ can be written as

$$e_{C,xy} = r \left(\theta - \sqrt{\theta^2 - \frac{h_A}{r}^2} \right) \ . \tag{4.23}$$

To find a more intuitive expression for the error $e_{C,xy}$, it can be rewritten as a function of the distance from the winch in the xy-plane instead of the involute parameter θ. For this

purpose, the distance between the EE and the winch anchor point A in the xy-plane can be expressed in the form

$$r_{AC,xy} = \left\| \begin{bmatrix} 1 & 0 & 0 \\ 0 & 1 & 0 \end{bmatrix} \mathbf{r}_{AC} \right\|_2 = r\sqrt{1 + \theta^2 - \left(\frac{h_A}{r}\right)^2} \,. \tag{4.24}$$

Substituting Eq. (4.24) into Eq. (4.23) yields the relation

$$e_{C,xy}(r_{AC,xy}) = \sqrt{r_{AC,xy}^2 + h_A^2 - r^2} - \sqrt{r_{AC,xy}^2 - r^2} \,, \tag{4.25}$$

which expresses the error introduced by neglecting the offset h_A in z-direction. The error is visualized for different ratios of $\frac{h_A}{r}$ in Figure 4.9.

(a) Involute error.

(b) Detail view.
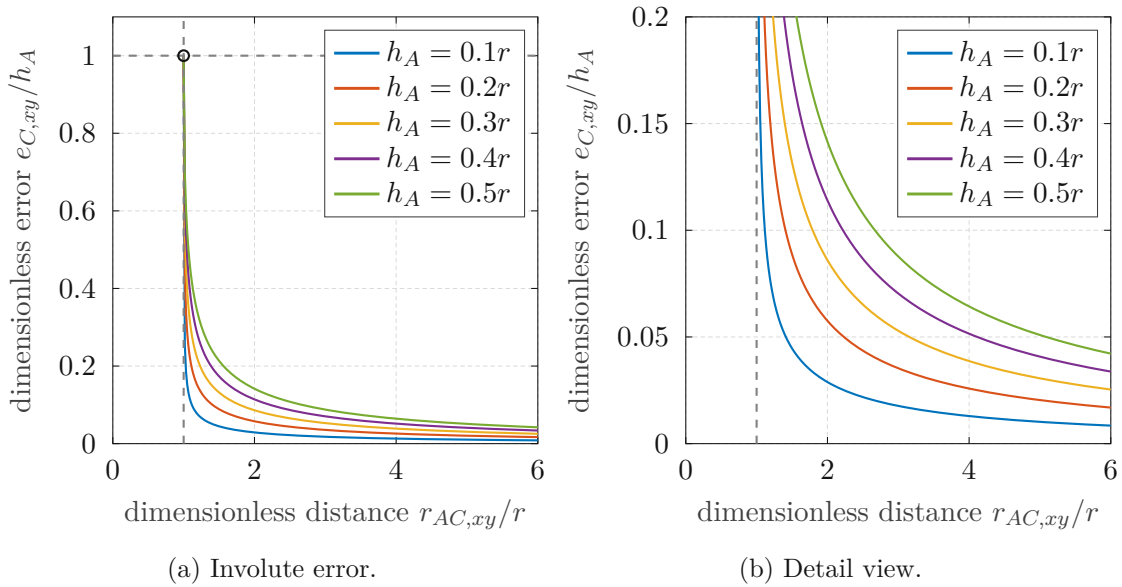
Figure 4.9: Involute error when neglecting the offset in z-direction.

From this figure, it can be concluded that the magnitude of $e_{C,xy}$ assumes a significant percentage of the EE height h_A. While the error is bounded by h_A and drops off quickly for positions further away from the winch, it remains in the order of several percent of the distance h_A for a wide range. To ensure that the EE is guided reliably by the guiding plane, the ratio $\frac{h_A}{r}$ must be chosen sufficiently large to ensure a sufficiently large contact force between the EE and the guiding plane. Hence, the offset h_A cannot be chosen arbitrarily small and must be carefully considered when designing a robot of this type. For most applications relying on the forward kinematics to obtain the EE position, considering the offset is crucial for obtaining a high positioning accuracy.

4.3 Initial pose estimation

For the iterative numerical solution of the nonlinear least-squares problem derived in Section 4.2.2, a suitable initial guess for the optimization variables $\boldsymbol{\theta}_e^0$ is necessary to

ensure convergence to the global optimum. In this section, a systematic algorithm for finding a suitable initial estimate of the EE pose $\mathbf{x}^0$, given the cable length i. e. joint coordinates $\mathbf{q}$, is presented. Note that the estimated EE position x_C and y_C can be easily converted to the involute parameters θ_i using the relation from Eq. (4.24) to obtain the initial guess for $\boldsymbol{\theta}_e^0$.

The algorithm presented in this section can be seen as an extension of the method described in [21] using axis-aligned bounding boxes. The basic idea of the algorithm is to strictly bound the position of the EE with low computational effort. Using the maximum possible distance from each winch, bounding boxes which are aligned with the coordinate axes can be created with very low numerical effort. The intersection of all bounding boxes then yields a region that certainly contains the EE location. The center of this region is subsequently used as an estimate for the EE location. This estimate is finally converted to an initial guess $\boldsymbol{\theta}_e^0$ for solving the optimization problem shown in Eq. (4.18).

First, an estimate for the rotation angle φ is calculated by treating the rotation and the translational movement of the EE separately. Using Eq. (4.4), the cable lengths i. e. joint coordinates $\mathbf{q}$ can be decomposed into

$$\mathbf{q} = \underbrace{\begin{bmatrix} l_{\varphi 0,1} & \dots & l_{\varphi 0,n_q} \end{bmatrix}^{\mathrm{T}}}_{\mathbf{l}_{\varphi 0}} - \underbrace{\begin{bmatrix} s_1 & \dots & s_{n_q} \end{bmatrix}^{\mathrm{T}}}_{\mathbf{s}} r\varphi \;, \tag{4.26}$$

where the vector $\mathbf{s}$ defines the cable configuration of the robot and $\mathbf{l}_{\varphi 0}$ is the vector of cable lengths without any rotation. Pure rotation of the EE causes a pattern in the joint coordinates which is a result of the winding configuration $\mathbf{s}$ while the cable lengths associated with translational movement are given by $\mathbf{l}_{\varphi 0}$. It is assumed, that for a robot with an even number of cables wrapped CW and CCW, the correlation of the pattern caused by $\mathbf{s}$ and $\mathbf{l}_{\varphi 0}$ is small. Hence, by correlating i. e. projecting $-\frac{\mathbf{s}}{n_q r}$ onto the joint vector $\mathbf{q}$, an approximation of the rotational component can be extracted with low numerical effort and an estimate φ^0 for the EE rotation angle φ can be obtained in the form

$$\varphi^0 = -\frac{\mathbf{s}^{\mathrm{T}}}{n_q r}\mathbf{q} = -\frac{1}{n_q r}\underbrace{\mathbf{s}^{\mathrm{T}}\mathbf{l}_{\varphi 0}}_{\approx 0} + \frac{1}{n_q}\underbrace{\mathbf{s}^{\mathrm{T}}\mathbf{s}}_{n_q}\varphi \approx \varphi \;. \tag{4.27}$$

To find the longest possible distance between the EE and a winch, consider the winch anchor point A_i and its first neighboring anchor point A_j which has the opposite winding direction such that $s_i = -s_j$. Starting from the reference position $\mathbf{r}_0$, the EE can move along the modified constraint involute to the point where the cable vectors $\mathbf{r}_{A'Bi}$ and $\mathbf{r}_{A'Bj}$ are aligned with each other as shown in Figure 4.10. This position is the boundary of the so-called wrench-closure workspace [19]. The robot is not able to move beyond this point in a controlled way, because the direction of available forces at the EE becomes limited.

The angle $\Delta\gamma_i$ denotes the angle between the cable vector $\mathbf{r}_{A'Bi,0}$ in the reference configuration and the straight line between the anchor points A_i and A_j and can be calculated using

$$\Delta\gamma_i = \arccos\frac{\mathbf{e}_{AiAj}^{\mathrm{T}}\mathbf{r}_{A'Bi,0}}{\|\mathbf{r}_{A'Bi,0}\|_2} \;, \tag{4.28}$$
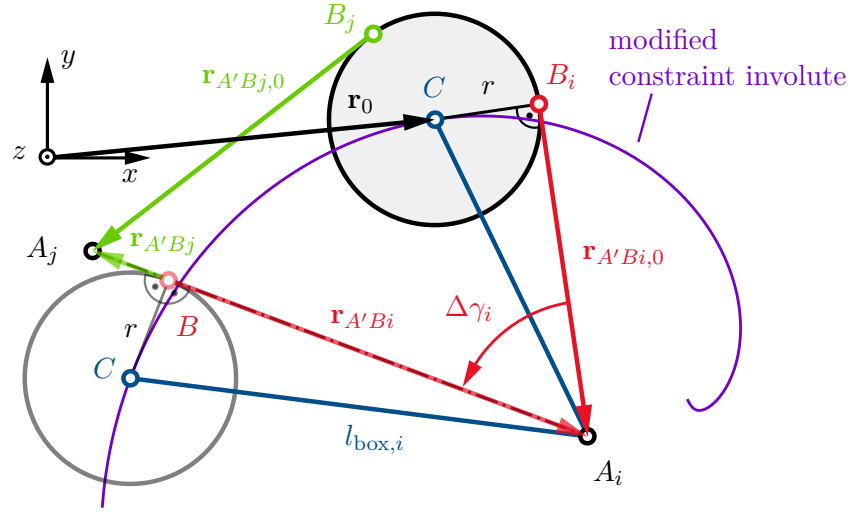
Figure 4.10: Maximum possible distance from the winch.

where $\mathbf{e}_{AiAj}$ denotes the unit vector which points from A_j to A_i. Respecting the maximum difference of the cable length from the reference position due to the measured length difference Δl_i as well as the unwound cable length $r\Delta\gamma_i$, the length

$$l_{\text{box},i} = \sqrt{(\|\mathbf{r}_{A'Bi,0}\|_2 + \Delta l_i + sr\varphi^0 + r\Delta\gamma_i)^2 + r^2} \tag{4.29}$$

is the maximum possible distance between the winch anchor point A_i and the EE center-point C.

Using the upper bound for the distance from the EE to each winch, bounding boxes in the form

$$\mathbf{r}_i^{\text{low}} = \mathbf{r}_{Ai} - l_{\text{box},i}\begin{bmatrix} 1 & 1 & 0 \end{bmatrix}^{\text{T}}$$
$$\mathbf{r}_i^{\text{high}} = \mathbf{r}_{Ai} + l_{\text{box},i}\begin{bmatrix} 1 & 1 & 0 \end{bmatrix}^{\text{T}} \tag{4.30}$$

can be created. The intersection of the n_q axis aligned bounding boxes can be calculated in the form

$$\mathbf{r}^{\text{low}} = \max_i \mathbf{r}_i^{\text{low}} \qquad\qquad \mathbf{r}^{\text{high}} = \min_i \mathbf{r}_i^{\text{high}} . \tag{4.31}$$

Finally, the centerpoint of the intersection bounding box is used to obtain an estimate for the pose

$$\mathbf{x}^0 = \begin{bmatrix} \begin{bmatrix} 1 & 0 & 0 \\ 0 & 1 & 0 \end{bmatrix} \frac{1}{2}(\mathbf{r}^{\text{low}} + \mathbf{r}^{\text{high}}) \\ \varphi^0 \end{bmatrix} . \tag{4.32}$$

Note that the quantities $\|\mathbf{r}_{A'Bi,0}\|_2$ and $\Delta\gamma_i$ can be pre-computed for the reference position and all steps involved in the initial pose estimation algorithm can be implemented computationally very efficiently on a real-time computer system. An example of the bounding boxes for $n_q = 4$ is shown in Figure 4.11. The intersection of the 4 bounding boxes is colored in grey and its center C^0, which represents the position estimate, is marked using a black square.

(a) Cable configuration.   (b) Bounding boxes.
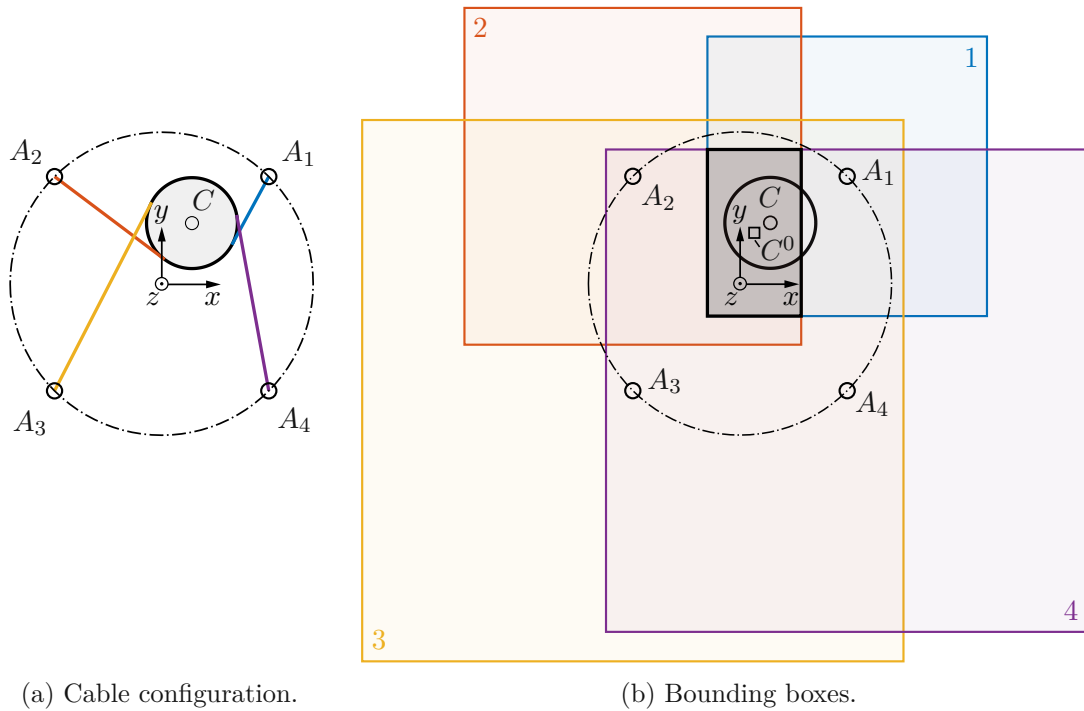
Figure 4.11: Pose estimation using axis aligned bounding boxes.

4.4 Convergence analysis

In this section, the convergence behavior of the presented forward kinematics solution is analyzed. Both the 3D geometry extension from Section 4.2.3 as well as the initial pose estimation algorithm from Section 4.3 are used if not stated otherwise. For solving the nonlinear least-squares problem, the Levenberg-Marquardt-Fletcher (LMF) method is used. The LMF method is a variation of the classical Levenberg-Marquardt algorithm where the damping parameter is adapted using the method proposed by Fletcher [26]. An implementation of the LMF algorithm in MATLAB is provided by Balda [27]. The library was slightly modified to make it suitable for code generation in MATLAB/SIMULINK for the deployment on a real-time computer system. The typical execution time of a single iteration of the LMF algorithm on the hardware prototype presented in Section 8.1 was found to be approximately $2.5\,\mu\text{s}$.

For the following convergence analysis, the LMF algorithm is used with a tolerance $\varepsilon_f = \varepsilon_x = 10^{-10}$, where ε_f denotes the stopping threshold for changes in the quality function value and ε_x denotes the stopping threshold for changes in the optimization variables. The maximum number of iterations was chosen as $n_{\max} = 50$, which was never reached during practical operation.

Throughout this work, three different designs of CDPRs are studied in detail and compared. For all robot designs, alternating winding directions are chosen in the form

$$s_i = (-1)^{i+1} \quad i = 1, 2, \ldots, n_q \,, \tag{4.33}$$

but they differ in the number of cables n_q. For Design A, the number of cables is $n_q = 4$, resulting in the configuration shown in Figure 4.12(a). For Design B, the number of cables is $n_q = 6$ as shown in Figure 4.12(b) and for Design C the number of cables $n_q = 8$ resulting in the CDPR configuration depicted in Figure 4.12(c).

(a) Configuration A
$n_q = 4$ cables.

(b) Configuration B
$n_q = 6$ cables.

(c) Configuration C
$n_q = 8$ cables.
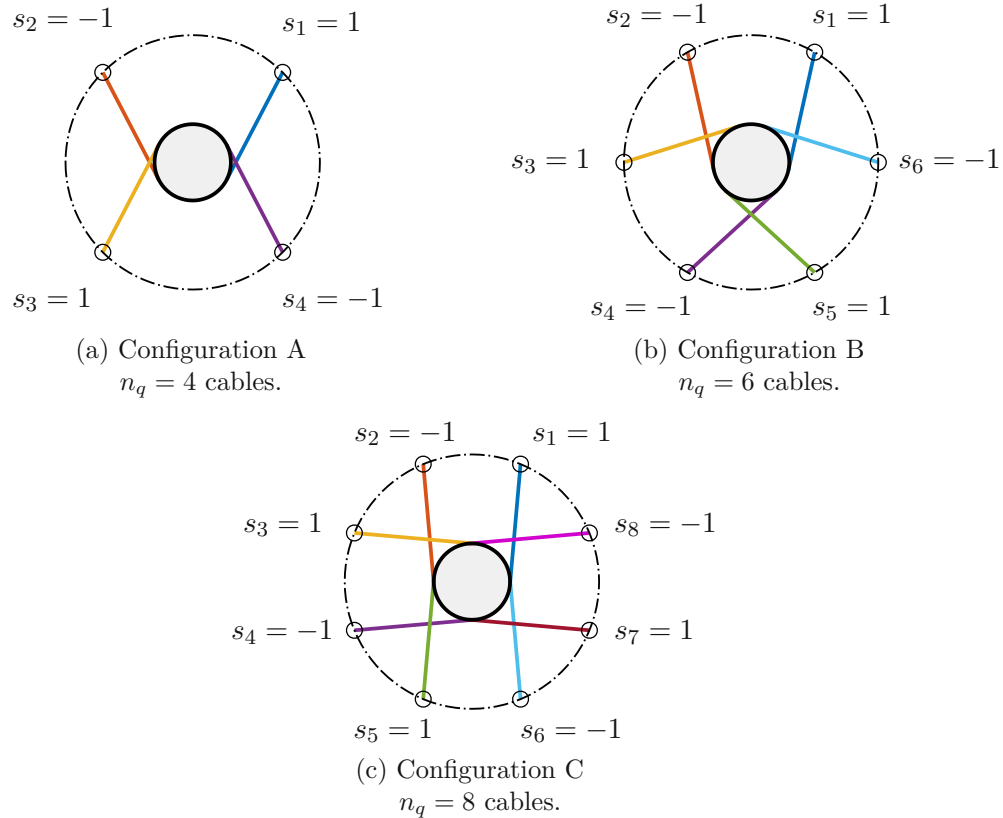
Figure 4.12: Cable configurations studied in detail.

For all robot designs, the geometric design parameters $r_w = 1\,\text{m}$, $r = 0.3\,\text{m}$, $h_A = h_C = 0\,\text{m}$ are used (see Figure 2.1(b) and Figure 3.1 for reference). These designs were chosen as candidates for the practical implementation of a general purpose manipulator prototype due to their symmetry. Different numbers of cables are studied with the aim of gaining insight into the effect of increasing the number of cables on the behavior of the resulting CDPR.

4.4.1 Convergence region

In this section, the convergence region of the forward kinematics solution is analyzed. The inverse kinematics are used to generate the joint vectors $\mathbf{q}$ on a grid of points x_C, y_C and for different EE angles φ. The forward kinematics algorithm is then applied to the simulated joint coordinates in order to retrieve a solution for the EE pose $\hat{\mathbf{x}}$. If the original pose $\mathbf{x}$ can be reconstructed with a position error $e_C < 10^{-6}$ m defined as

$$e_C = \|\mathbf{r}_C - \hat{\mathbf{r}}_C\|_2 \, , \tag{4.34}$$

the forward kinematics algorithm is considered to have converged successfully. The results for Design A are depicted in Figure 4.13. On the left side, Figure 4.13(a) shows the convergence region of the forward kinematics using the origin as initial pose estimate $\mathbf{x}^0 = \mathbf{0}$. In comparison, Figure 4.13(b) shows the convergence region using the initial pose estimation algorithm presented in Section 4.3.

(a) Origin as initial pose estimate.   (b) Initial pose estimation algorithm.
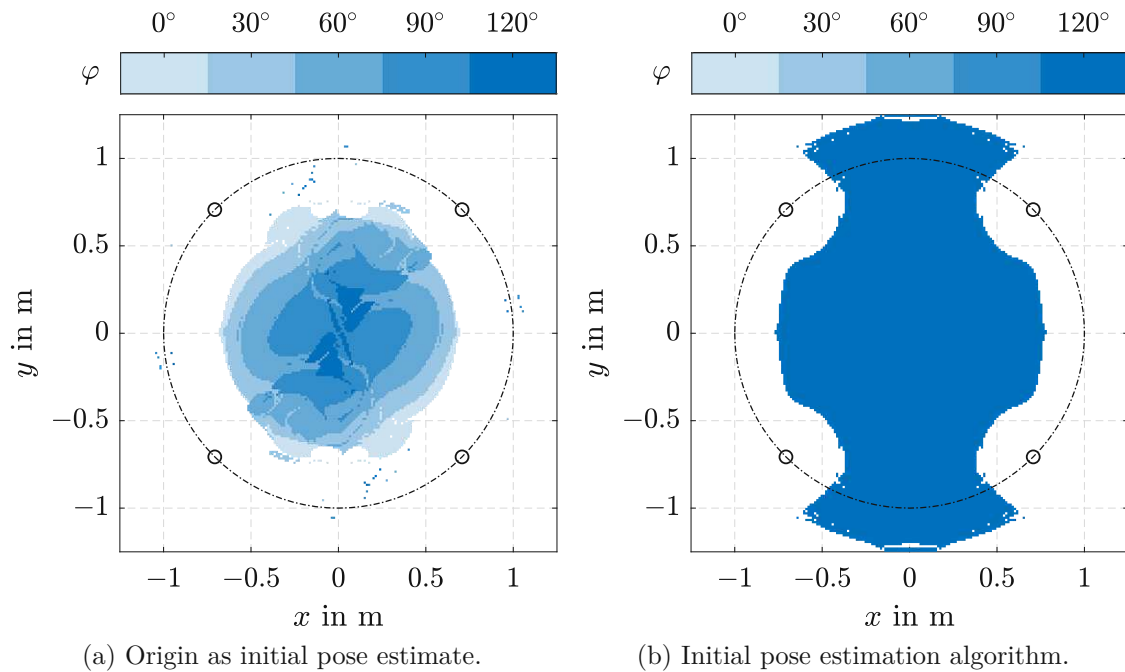
Figure 4.13: Convergence region of Design A.

Without any systematic initial pose estimation, the convergence region rapidly contracts for increasing values of φ. Also note that the convergence region is not continuous but has holes and there are spurious points where the algorithm converges. Using the proposed systematic initial pose estimation algorithm, convergence can be achieved even for large EE rotation angles φ and the convergence region is significantly improved.

The same behavior is confirmed for Design B and C and the resulting convergence regions with and without the initial pose estimation algorithm are shown in Figure 4.14 and Figure 4.15 respectively.

(a) Origin as initial pose estimate.

(b) Initial pose estimation algorithm.
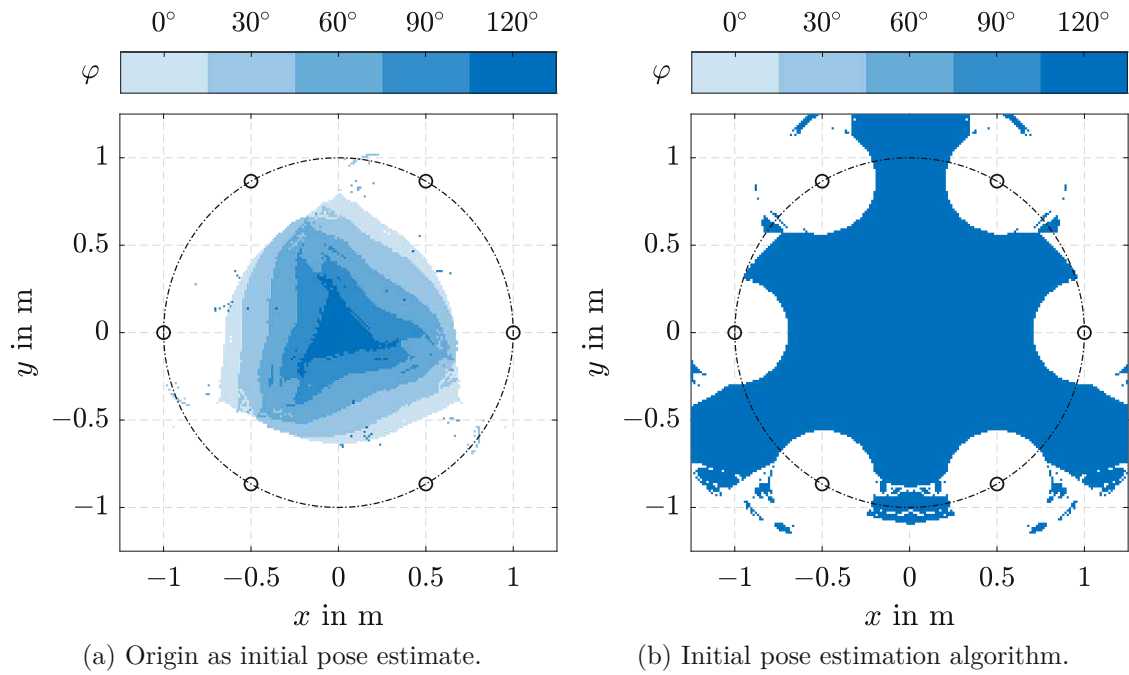
Figure 4.14: Convergence region of Design B.

(a) Origin as initial pose estimate.

(b) Initial pose estimation algorithm.
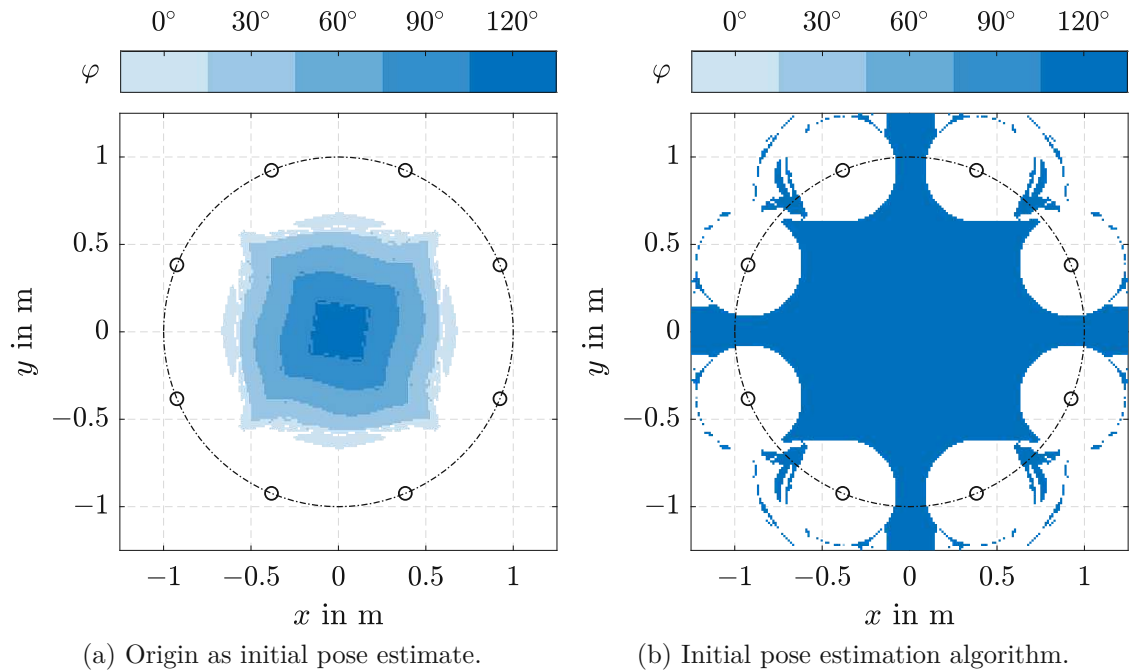
Figure 4.15: Convergence region of Design C.

4.4.2 Impact of measurement noise

In this section, the impact of measurement noise on the forward kinematics solution is investigated. For this purpose, joint coordinates are generated for uniformly random EE positions with $-r < x_C < r$, $-r < y_C < r$ and $\varphi = 0$. The simulated cable lengths $\mathbf{q}$ are disturbed by adding Gaussian noise with zero mean and different values for the standard deviation σ. For each noise level σ, a number of N evaluations of the forward kinematics algorithm are computed to gain insight into the statistical behavior of the algorithm.

Figure 4.16 shows the average position error and the average number of iterations using $N = 1000$ for a wide range of different noise values.
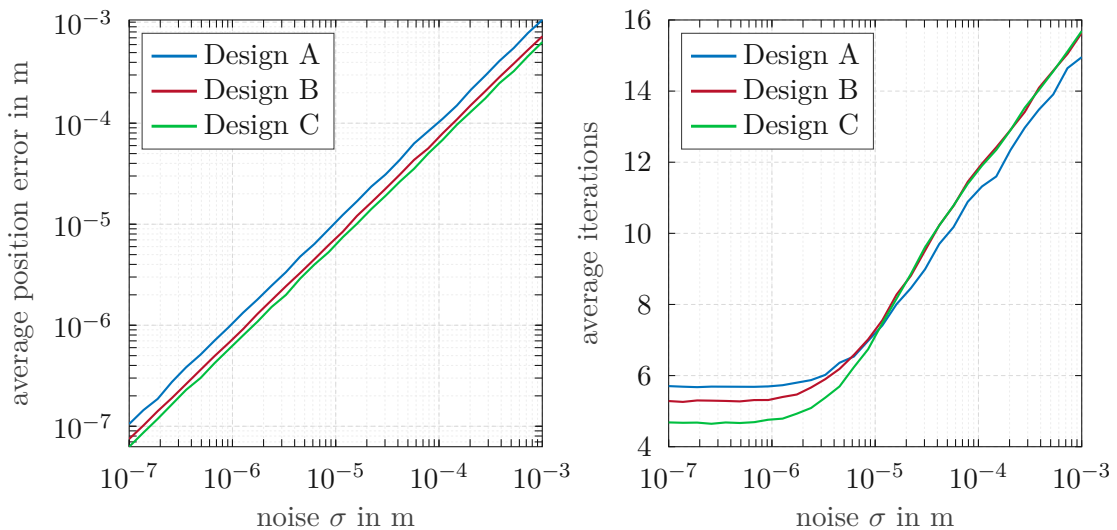
Figure 4.16: Impact of noise on the position error and number of iterations.

The position error is linearly proportional to the noise in the joint space and intuitively decreases with a larger number of cables used. While the average number of iterations necessary for the forward kinematics algorithm to converge is around 5 for small noise levels $\sigma < 10^{-6}$ m, it increases steadily for larger amounts of noise.

The distribution of the position error and the number of iterations is studied for three selected values for the standard deviation $\sigma = 0.1\,\mathrm{mm}$, $\sigma = 0.5\,\mathrm{mm}$ and $\sigma = 2.5\,\mathrm{mm}$. The position error as well as the number of iterations required by the algorithm are evaluated for $N = 10000$ EE positions. The results for Design A, B and C are shown in Figure 4.17. Here it is confirmed, that the position error decreases as the number of cables increases as the peaks of the position error distribution shift slightly to smaller values and the distributions become narrower with an increasing number of cables.

It can be concluded, that the forward kinematics algorithm is very robust with respect to measurement noise and converges reliably in the presence of noise.
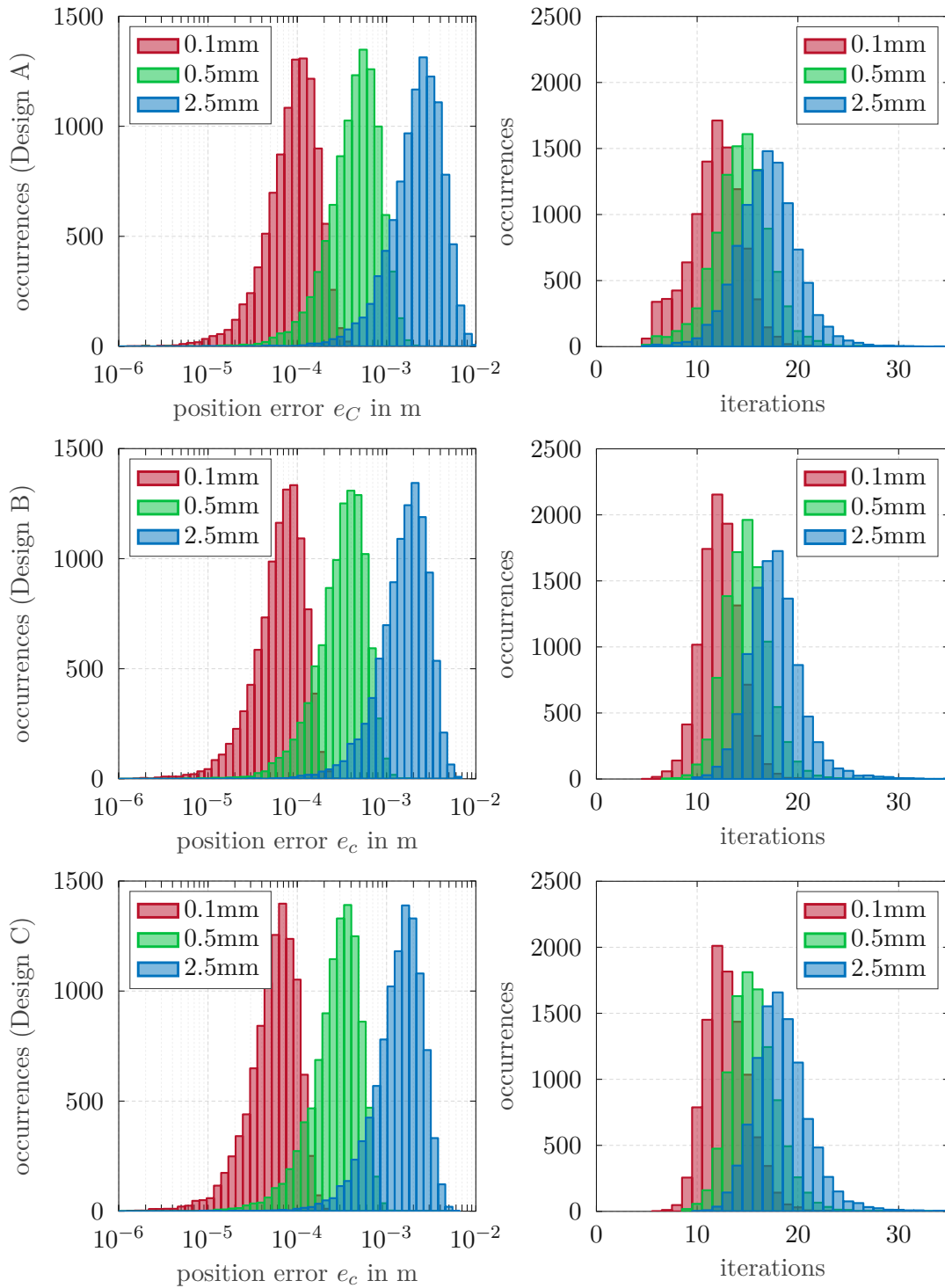
Figure 4.17: Convergence behavior for different noise levels ($\sigma = 0.1\,\mathrm{mm}, 0.5\,\mathrm{mm}, 2.5\,\mathrm{mm}$).
Design A (top), Design B (center) and Design C (bottom).

5 Workspace analysis

In this chapter, the workspace and its quality are studied for the novel CDPR concept. There exist many different notions and definition of a robot's workspace as well as performance criteria to judge the quality of its interior. CDPRs exhibit the fundamental limitation that the cables always need to remain under tension, which has a defining effect on the workspace of a CDPR.

As previously discussed, CDPRs inherently need to be overactuated to achieve tension in all cables without having to rely on external forces. The relation between the cable forces $\boldsymbol{\tau}$ and the resulting task-space wrench $\mathbf{f}$ is given by the Jacobian matrix of the inverse kinematics $\mathbf{J}_{\mathrm{ik}}^{\mathrm{T}}$ as shown in Eq. (3.17). As a consequence of the kinematic redundancy, the matrix $\mathbf{J}_{\mathrm{ik}}^{\mathrm{T}}$ is rectangular. Thus, there exists a nullspace in which additional cable forces can be added without affecting the resulting wrench $\mathbf{f}$. Using these null space cable forces, tension in all cables can be achieved and the magnitude of the tension forces can be adjusted as desired.

This intuitive notion leads to the so-called *wrench-closure workspace*, which is the set of all EE poses, for which any wrench can be exerted by positive cable forces using appropriate forces in the null space of $\mathbf{J}_{\mathrm{ik}}^{\mathrm{T}}$. Here, positive cable forces correspond to pulling forces by convention. This means that the CDPR loses its general manipulation capabilities outside the wrench-closure workspace, because forces cannot be generated in some directions. The wrench-closure workspace originates from purely kinematic constraints and can thus be investigated by analyzing the null space of $\mathbf{J}_{\mathrm{ik}}^{\mathrm{T}}$, e. g. using the method described in [28].

The problem of finding a suitable cable force distribution and thus choosing appropriate null space cable forces is a major challenge for CDPRs. For the special case of so-called completely restrained CDPRs which have exactly $n_q = n_x + 1$ cables, the nullspace is 1-dimensional and the problem is comparatively simple. A closed-form algorithm to find suitable forces and choosing the desired tension in the cables is presented in [29]. In [21], different force distribution methods for redundantly restrained robots with $n_q > n_x + 1$ are discussed and compared.

A unique choice of $\boldsymbol{\tau}$ can be found by the solution of the optimization problem

$$
\begin{aligned}
\min_{\boldsymbol{\tau}} \quad & \|\boldsymbol{\tau} - \boldsymbol{\tau}_{\mathrm{d}}\|_2 \\
\text{s.t.} \quad & \boldsymbol{\tau}_{\min} \le \boldsymbol{\tau} \le \boldsymbol{\tau}_{\max}, \\
& \mathbf{f}_{\mathrm{d}} = -\mathbf{J}_{\mathrm{ik}}^{\mathrm{T}} \boldsymbol{\tau},
\end{aligned}
\tag{5.1}
$$

where $\boldsymbol{\tau}_{\mathrm{d}}$ defines the desired pre-tension forces of the cables, which is a design parameter. For the analysis of the workspace $\boldsymbol{\tau}_{\mathrm{d}} = \boldsymbol{\tau}_{\min} = \mathbf{0}$ and $\boldsymbol{\tau}_{\max} = \mathbf{1}\tau_{\max}$ is chosen and the geometric parameters $r_{\mathrm{w}} = 1\,\mathrm{m}$ and $r = 0.3\,\mathrm{m}$ are selected. In the following, all figures of the workspace are restricted to the wrench-closure workspace, indicating the theoretical limit of achievable EE positions due to the kinematic constraints.

5.1 Manipulability

The so-called *manipulability* is a measure of how close a robot is to a singular configuration. To derive this measure, the reachable task-space velocities for all joint velocities of unit length are investigated, see [4]

$$\mathcal{E} = \{\dot{\mathbf{x}} \,|\, \|\dot{\mathbf{q}}\|_2 = 1\} \,. \tag{5.2}$$

Explicitly, this set can be expressed as

$$\dot{\mathbf{q}}^{\mathrm{T}}\dot{\mathbf{q}} = 1 \tag{5.3}$$

$$\dot{\mathbf{x}}^{\mathrm{T}}\mathbf{J}_{\mathrm{ik}}^{\mathrm{T}}\mathbf{J}_{\mathrm{ik}}\dot{\mathbf{x}} = 1 \,. \tag{5.4}$$

Thus, Eq. (5.2) defines an ellipsoid, also called the *manipulability ellipsoid.*

A multitude of manipulability indices based on this ellipsoid have been proposed in the literature, see, e.g., [16, 17]. Here, the manipulability measure

$$m_1 = \sqrt{\det(\mathbf{J}_{\mathrm{ik}}^{\mathrm{T}}\mathbf{J}_{\mathrm{ik}})^{-1}} \tag{5.5}$$

is used for the following investigations. This measure is proportional to the volume of the manipulability ellipsoid and vanishes at singular configurations. If the achievable task-space velocities are evenly distributed in all directions, Eq. (5.5) yields large values. Due to the inverse relation between the force ellipsoid and the manipulability ellipsoid, this also implies that wrenches can be realized evenly in all task-space directions, see Eq. (3.17) and [17].

In Figure 5.2(a), the manipulability measure for Design A is shown. Here, the wrench-closure workspace, i.e. the set of poses where an arbitrary wrench can be achieved, is characterized by one principal direction. This directionality is a consequence of the pairs (s_1, s_2) and (s_3, s_4) wrapped around the EE platform, as illustrated in Figure 5.1(a). These cable pairs are considered *strong pairs* because they facilitate forces in the corresponding y-direction. In contrast, the cables of the pairs (s_1, s_4) and (s_2, s_3) cross between the winches and the EE as indicated in Figure 5.1(b), and thus the feasible forces in x-direction are limited which is why these cable pairs will be referred to as *weak pairs.*

In general, the manipulability measure varies only slightly in the whole reachable task space. The generality of the manipulability measure does not allow for a more detailed analysis of the capabilities of this design.

Figure 5.2(b) shows the manipulability measure of Design B. Again, the manipulability measure varies only slightly in the whole reachable task space. Furthermore, it would be expected that the EE is best to manipulate in the center of the workspace where in fact the manipulability measure is lowest.

The manipulability measure of Design C, depicted in Figure 5.2(c) shows a similar behavior as for Design B. While the CDPR is intuitively expected to perform best in the center of its workspace, the manipulability measure is lowest there and reaches its peak values just at the edges of the wrench-closure workspace.

In contrast to robots consisting of rigid links, the workspace of CDPRs is not limited by singularities but by the inability of the cables to exert pushing forces. This directional

(a) Strong pair (s_1, s_2).   (b) Weak pair (s_1, s_4).
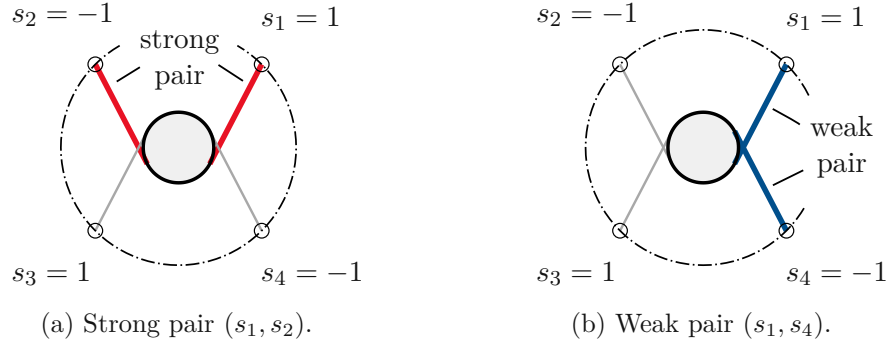
Figure 5.1: Strong pair and weak pair of cables.

constraint is not captured by the classical manipulability measure m_1. This is why $\mathbf{J}_{\mathrm{ik}}^{\mathrm{T}}$ is well conditioned even at the borders of the task space, which also leads to a high manipulability measure. Therefore, the classical manipulability measure presented in Eq. (5.5) is not well suited to analyze the feasible forces close to the borders of the workspace of a CDPR and does not allow a detailed analysis of the given wrench directions. This is why a different measure of manipulability for this type of robot kinematics is presented in the following section.

5.2 Force efficiency

From a practical perspective, the minimum tension required in each cable and the highly nonlinear directional dependence of the achievable wrenches are the determining factors for the workspace of a CDPR. For the robot to move effectively in the largest possible workspace area, the maximum load on a single cable is the limiting factor. Thus, the *force efficiency* index is proposed to measure the ratio between a given wrench and the maximum cable force to realize this wrench [11].

Similar to the well-known force manipulability ellipsoid, see, e.g., [4, 17], for a chosen cable force τ_{s} on the most stressed cable

$$\tau_{\min} < \tau_{\mathrm{s}} < \tau_{\max}, \tag{5.6}$$

all achievable wrenches form a polytope

$$\mathcal{P}_F = \{\mathbf{f} \,|\, \|\boldsymbol{\tau}\|_\infty = \tau_{\mathrm{s}} \wedge \boldsymbol{\tau}_{\min} \leq \boldsymbol{\tau}\} \tag{5.7}$$

where the elements of $\mathcal{P}_F$ are defined by Eq. (5.1). For any chosen direction $\mathbf{d}$, where $\|\mathbf{d}\|_2 = 1$, the wrench

$$\mathbf{f}_{\mathrm{d}} = f\mathbf{d} \tag{5.8}$$

with unique magnitude f is achievable, such that $\mathbf{f}_{\mathrm{d}} \in \mathcal{P}_{\mathrm{F}}$. The force efficiency η in direction $\mathbf{d}$ is defined in the form

$$\eta = \frac{f}{\tau_{\mathrm{s}}}. \tag{5.9}$$

(a) Manipulability measure of Design A.

(b) Manipulability measure of Design B.

(c) Manipulability measure of Design C.
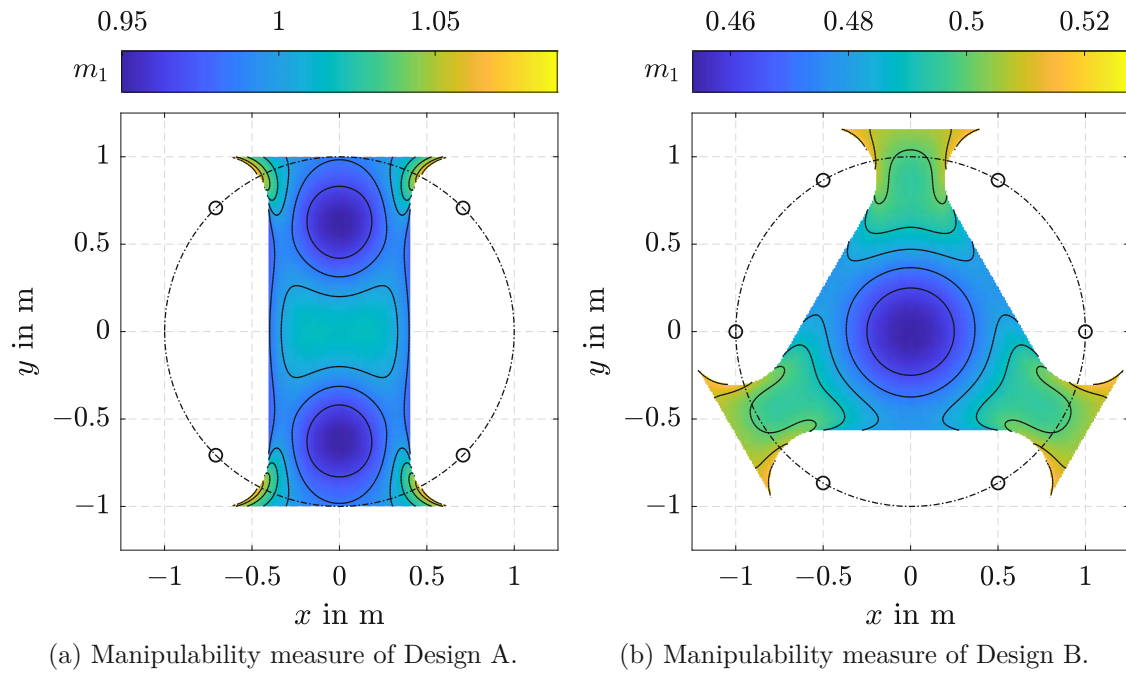
Figure 5.2: Manipulability measure m_1 of Design A, B and C.

This definition is similar to the *manipulator mechanical advantage*, see [30], but respects the fundamental limits in the tension of the cable forces. The force efficiency can be interpreted as the kinematic transmission of cable forces to given task-space wrenches. Thus $\eta > 1$ indicates that multiple cables facilitate the given task-space wrench and $\eta = 0$ indicates that $\mathbf{x}$ is outside the wrench-feasible workspace. Note that in general the force efficiency depends on the cable forces in the nullspace of $\mathbf{J}_{\mathrm{ik}}^{\mathrm{T}}$, which are defined by Eq. (5.1) and depend on the parameters $\boldsymbol{\tau}_{\mathrm{min}}, \boldsymbol{\tau}_{\mathrm{max}}$ and $\boldsymbol{\tau}_{\mathrm{d}}$. Hence, it is a very practical measure of the CDPR performance to predict the feasible magnitude of wrenches in any given direction of interest $\mathbf{d}$. For the idealized case $\boldsymbol{\tau}_{\mathrm{min}} = \boldsymbol{\tau}_{\mathrm{d}} = \mathbf{0}$ the force efficiency does not depend on the desired force $\mathbf{f}_{\mathrm{d}}$, but measures a kinematic property. The isolines of the force efficiency are closely related to the wrench-feasible workspace, see e.g. [18]. In addition, the interior of the wrench-feasible workspace can be analyzed by the force efficiency.

In the following, the force efficiency defined in Eq. (5.9) is analyzed for wrenches acting in different directions in a cylindrical coordinate system centered in the origin as depicted in Figure 5.3.
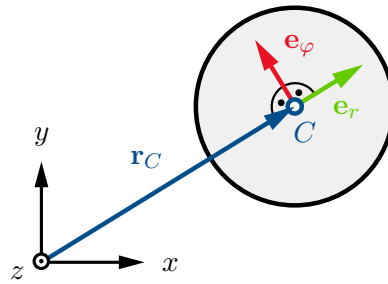
Figure 5.3: Basis vectors $\mathbf{e}_r$ and $\mathbf{e}_\varphi$ for cylindrical coordinates.

The radial basis vector $\mathbf{e}_r$ and the azimutal basis vector $\mathbf{e}_\varphi$ are given by

$$\mathbf{e}_r = \frac{1}{\sqrt{x_C^2 + y_C^2}} \begin{bmatrix} x_C \\ y_C \\ 0 \end{bmatrix}, \qquad \mathbf{e}_\varphi = \frac{1}{\sqrt{x_C^2 + y_C^2}} \begin{bmatrix} -y_C \\ x_C \\ 0 \end{bmatrix}. \tag{5.10}$$

Figure 5.4 provides an overview of the force efficiency of Design A for different directions $\mathbf{d}$. In Figure 5.4(a) the force efficiency for an outward motion away from the origin using $\mathbf{d} = \mathbf{e}_r$ is shown. Here, it is confirmed that the radial outward movement is achieved by two pulling cables with a force efficiency $\eta > 1.5$ in the central axes between the kinematically strong pairs of cables, which do not cross between the winches and the EE. Due to the strong pairs of cables, the CDPR has two favorable directions which are clearly visible using the force efficiency. In contrast to the manipulability measure, see Figure 5.2, the force efficiency decreases towards the boundaries of the wrench-feasible workspace.

Figure 5.4(b) depicts the force efficiency for $\mathbf{d} = -\mathbf{e}_r$ which corresponds to a radial inward motion towards the origin. Movements towards the centerpoint of the robot are highly efficient over the whole workspace because multiple cables can always participate in pulling the EE towards the origin.

The force efficiency for azimutal motion around the origin with $\mathbf{d} = \mathbf{e}_\varphi$ is depicted in Figure 5.4(c). Here the favorable regions are clearly visible and it is confirmed that for a large region of the workspace a force efficiency of $\eta \approx 1$ can be achieved.

Finally in Figure 5.4(d), the force efficiency for a rotational motion of the EE using $\mathbf{d} = [0, 0, 1]^{\mathrm{T}}$ is presented. Pure rotation in CCW direction without translational movement can be achieved best along an axis which is diagonal to the preferred axis for translational motion.

Comparing Design A, B and C it can be concluded that intuitively, adding more cables provides more favorable directions of motion. However, increasing the number of cables also increases the cost and complexity of the CDPR. Design B using $n_q = 6$ cables is considered to be a good trade-off between cost and quality of the resulting workspace for the realization of a general planar manipulator. For this reason, Design B is selected for implementing a hardware prototype.

(a) Force efficiency in direction $\mathbf{d} = \mathbf{e}_r$ (radially outward from the origin).

(b) Force efficiency in direction $\mathbf{d} = -\mathbf{e}_r$ (radially inward towards the origin).

(c) Force efficiency in direction $\mathbf{d} = \mathbf{e}_\varphi$ (CCW around the origin).

(d) Force efficiency in direction $\mathbf{d} = [0, 0, 1]^{\mathrm{T}}$ (rotation of the EE).
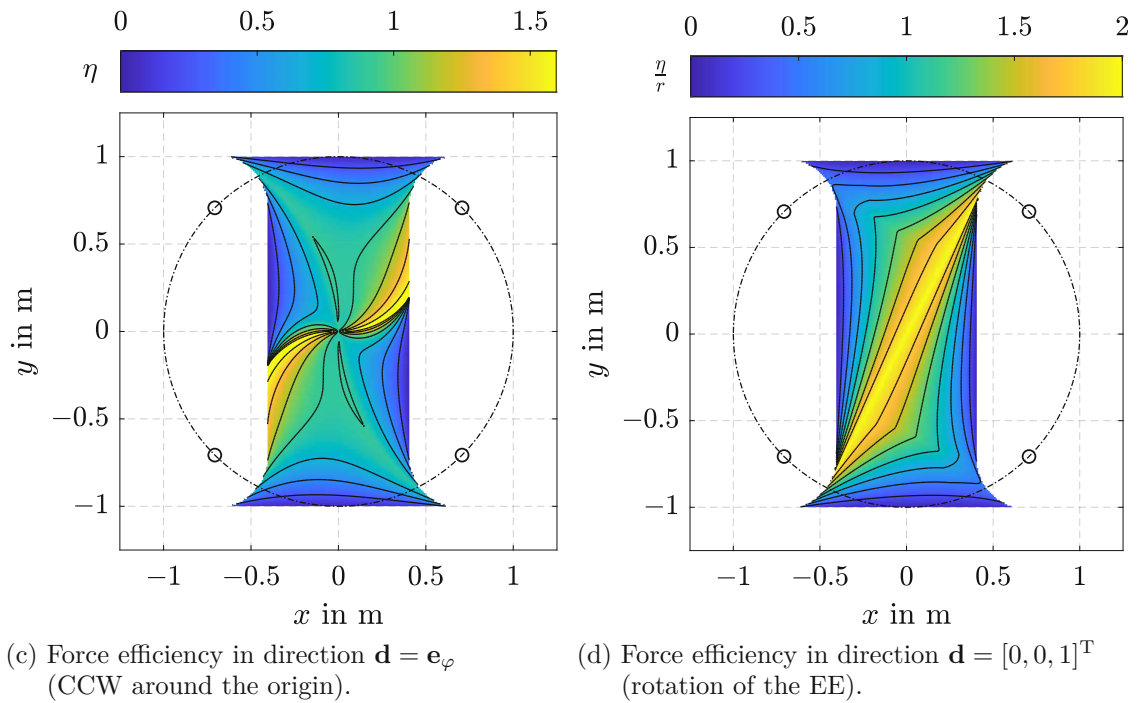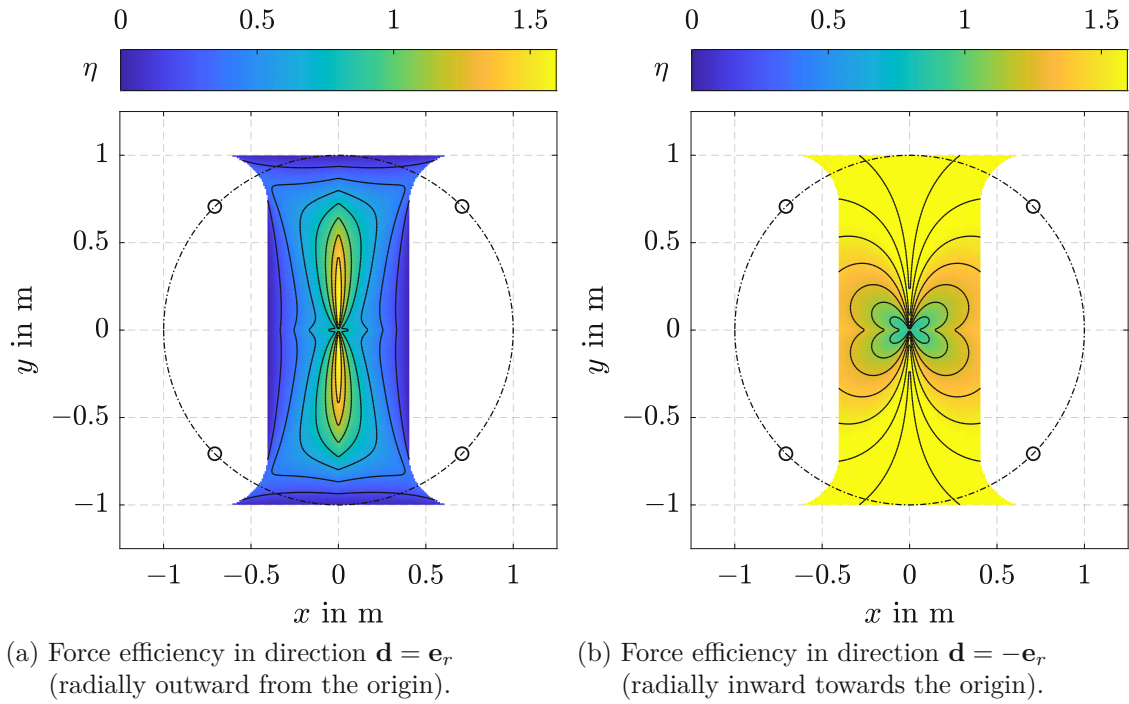
Figure 5.4: Force efficiency η in different directions $\mathbf{d}$ for Design A.

(a) Force efficiency in direction $\mathbf{d} = \mathbf{e}_r$ (radially outward from the origin).

(b) Force efficiency in direction $\mathbf{d} = -\mathbf{e}_r$ (radially inward towards the origin).

(c) Force efficiency in direction $\mathbf{d} = \mathbf{e}_\varphi$ (CCW around the origin).

(d) Force efficiency in direction $\mathbf{d} = [0, 0, 1]^{\mathrm{T}}$ (rotation of the EE).
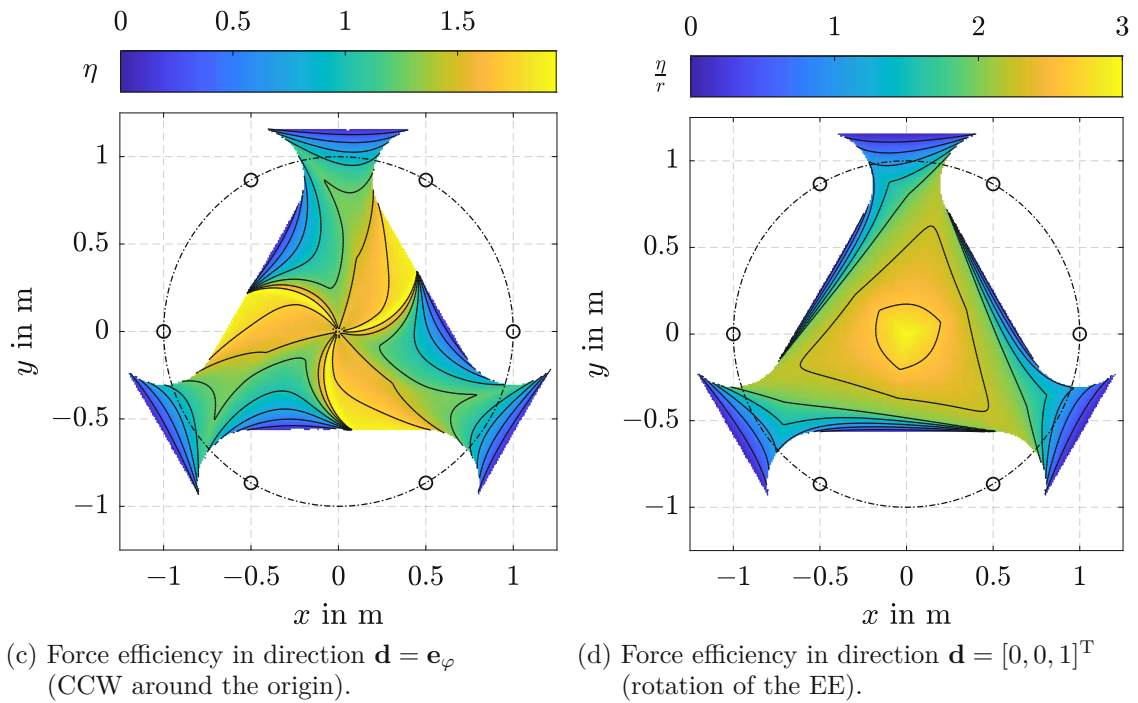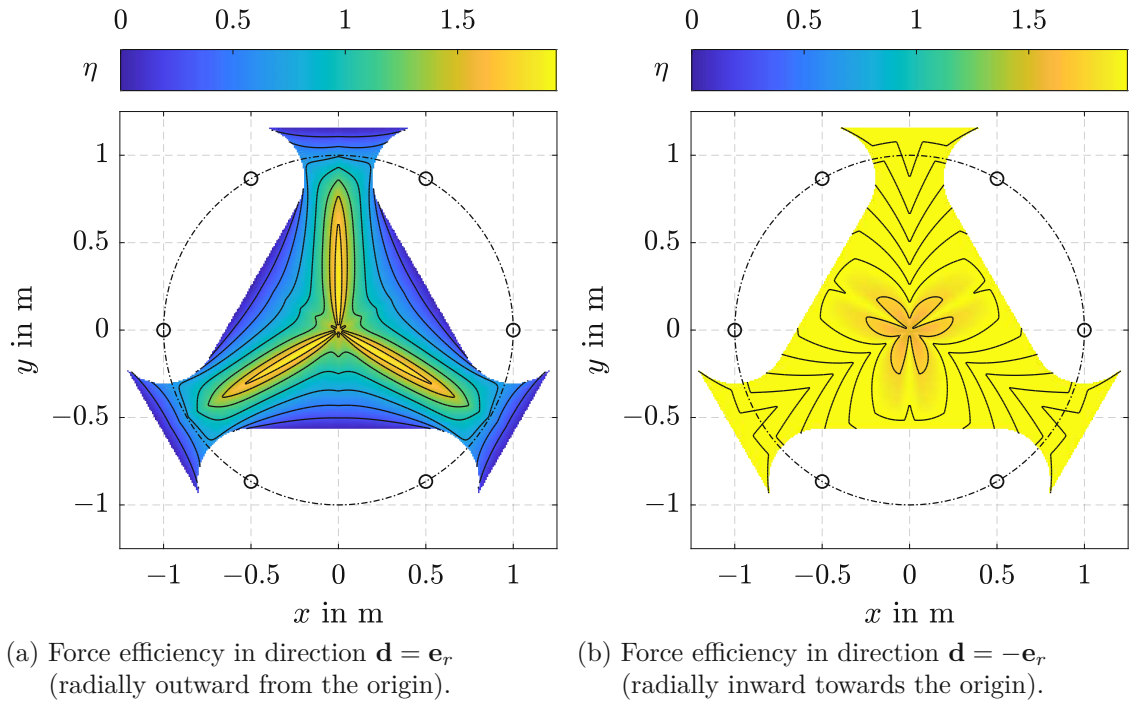
Figure 5.5: Force efficiency η in different directions $\mathbf{d}$ for Design B.

(a) Force efficiency in direction $\mathbf{d} = \mathbf{e}_r$ (radially outward from the origin).

(b) Force efficiency in direction $\mathbf{d} = -\mathbf{e}_r$ (radially inward towards the origin).

(c) Force efficiency in direction $\mathbf{d} = \mathbf{e}_\varphi$ (CCW around the origin).

(d) Force efficiency in direction $\mathbf{d} = [0, 0, 1]^{\mathrm{T}}$ (rotation of the EE).
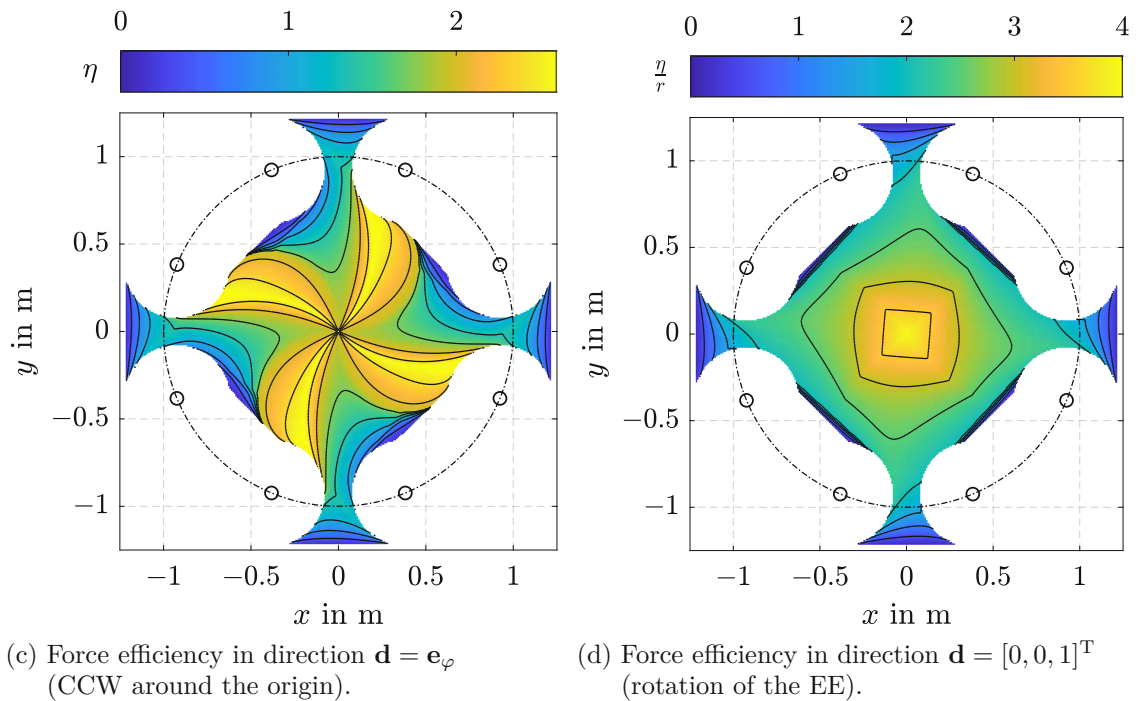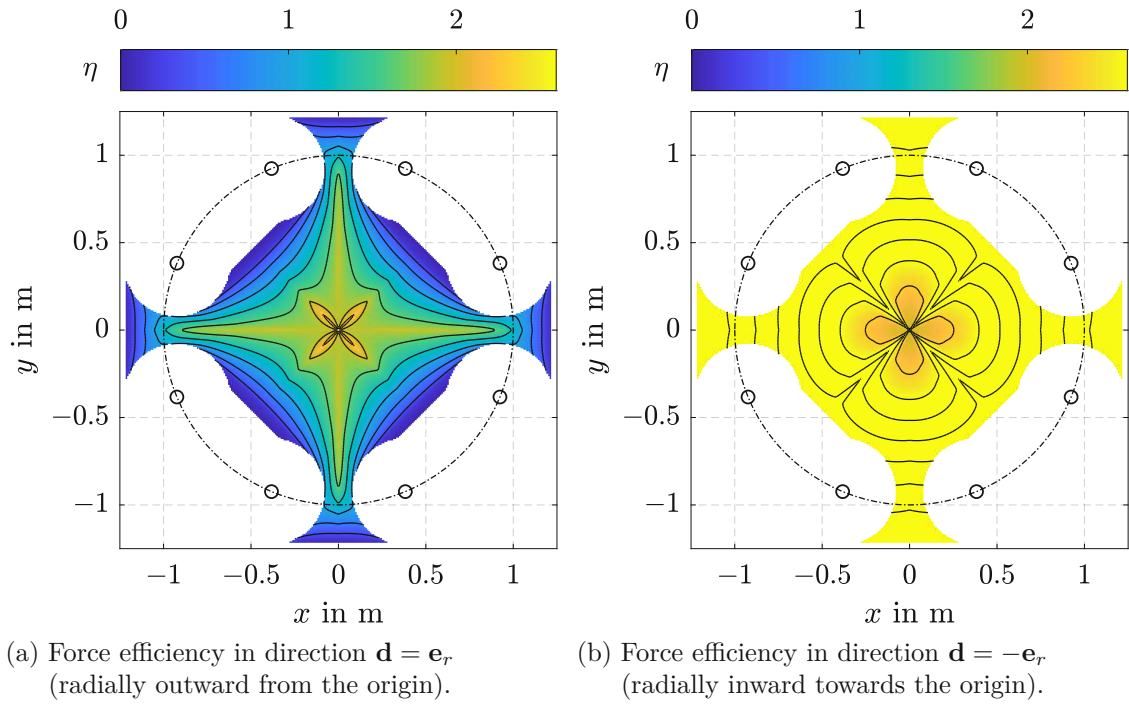
Figure 5.6: Force efficiency η in different directions $\mathbf{d}$ for Design C.

5.3 Uneven numbers of cables

So far, only CDPR designs with even numbers of cables have been considered in this work. In this section, the possibility of creating a robot with an uneven number of cables is investigated and briefly discussed. Figure 5.7 shows the studied Design D using $n_q = 5$ cables.
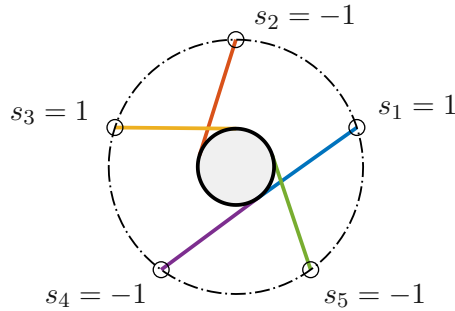
Figure 5.7: Cable configuration D using $n_q = 5$ cables.

Computing the force efficiency η and applying the previously gained understanding of kinematically strong pairs of cables, the workspace of Design D can be analyzed. For Design D, cables (s_1, s_2) and cables (s_3, s_4) form strong pairs. These strong pairs are neighboring cables with different winding directions which are capable of very efficiently pulling the EE radially outwards i.e. away from the origin in the direction $\mathbf{e}_r$. As a result

(a) Force efficiency in direction $\mathbf{d} = \mathbf{e}_r$ (radially outward from the origin).

(b) Force efficiency in direction $\mathbf{d} = \mathbf{e}_\varphi$ (CCW around the origin).
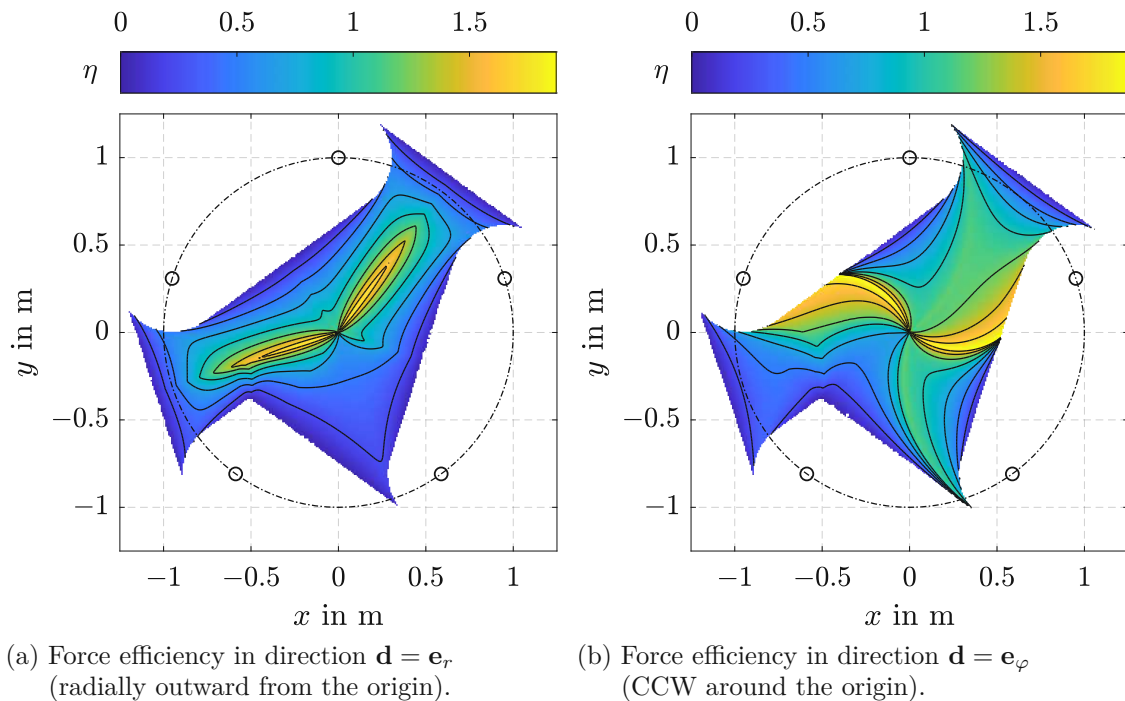
Figure 5.8: Force efficiency η in different directions $\mathbf{d}$ for Design D.

of the strong pairs, the force efficiency in the direction $\mathbf{d} = \mathbf{e}_r$ depicted in Figure 5.8(a) shows two favorable directions. Figure 5.8(b) shows the force efficiency for azimutal motion around the origin in direction $\mathbf{d} = \mathbf{e}_\varphi$. Comparing Design D with Designs A and B (see Figure 5.4 and 5.5) it can be seen that Design D exhibits features from both Design A and Design B. Intuitively, using $n_q = 5$ cables can be seen as either an extension of Design A ($n_q = 4$) or an incomplete version of Design B ($n_q = 6$). While Design D has two strong pairs, the additional cable s_5 extends the workspace and adds a useful part of the wrench-closure workspace. However, cable s_5 does not form a strong pair and thus a third favorable direction such as in Design B is lacking.

Figure 5.9 shows the force efficiency for pure rotation in both CCW and CW directions. This reveals the strong asymmetry in the design which is caused by the uneven number of cables. There are 3 cables which can participate in rotating the EE in CW direction as revealed in Figure 5.9(b). At the same time there are only only 2 cables which can participate in CCW rotation of the EE as shown in Figure 5.9(a). With respect to pure

(a) Force efficiency in direction $\mathbf{d} = [0, 0, 1]^{\mathrm{T}}$ (CCW rotation of the EE).

(b) Force efficiency in direction $\mathbf{d} = [0, 0, -1]^{\mathrm{T}}$ (CW rotation of the EE).
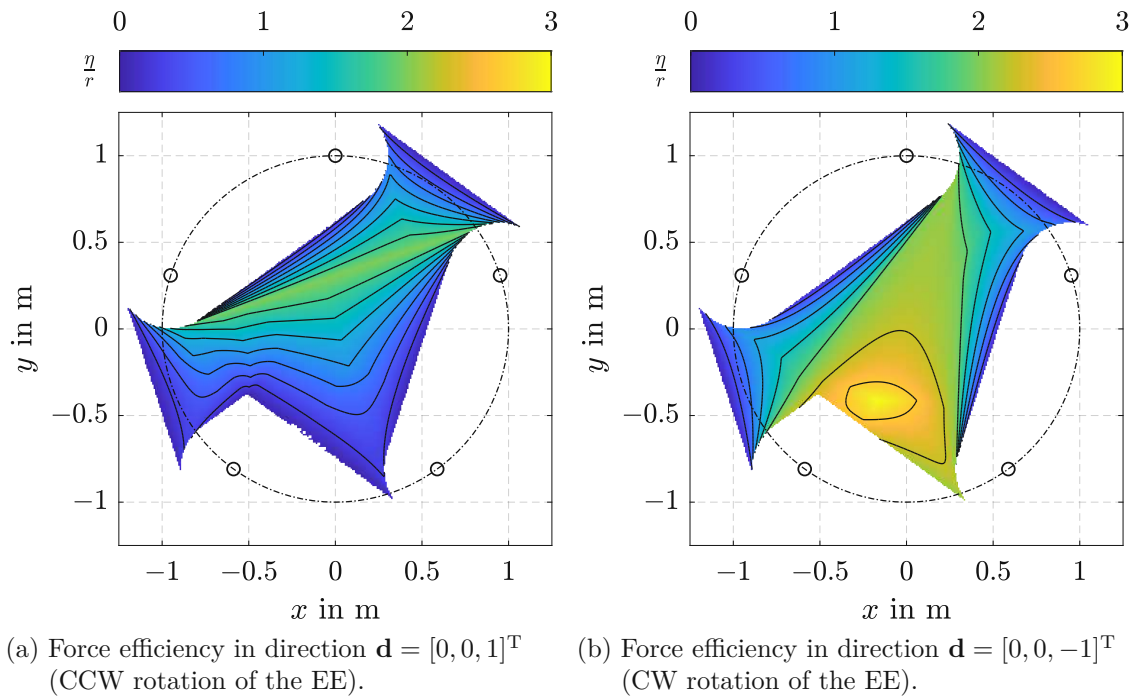
Figure 5.9: Force efficiency η for rotation of Design D.

rotation of the EE, it can be seen that Design D performs similarly to Design A for CCW rotation and exhibits a similar behavior as Design B for CW rotation.

It can be concluded that CDPR designs using uneven numbers of cables show strong asymmetry and can be seen as an intermediate design between their counterparts with even numbers of cables. While the asymmetry in the manipulation capabilities is not desirable for a general manipulator, specialized robots are conceivable which can benefit from the asymmetric characteristics.

6 Dynamic robot model

A CDPR is a mechatronic system consisting of many interacting parts and subsystems from different physical domains. In this chapter, a control-oriented dynamic robot model is derived focusing on the mechanical domain. In Section 6.1, an overview over the model structure and the interacting components is provided. A simple mechanical model for the cable winch is discussed in Section 6.2. Based on the inverse kinematics presented in Chapter 3, the equations of motion for the robot are derived in Section 6.3. The dynamic model is then used in Chapter 7 to design a controller for the CDPR.

6.1 Mechatronic structure

Figure 6.1 shows the different mechatronic elements and physical interfaces between the elements in a schematic view. The robot is actuated by an electric drivetrain which
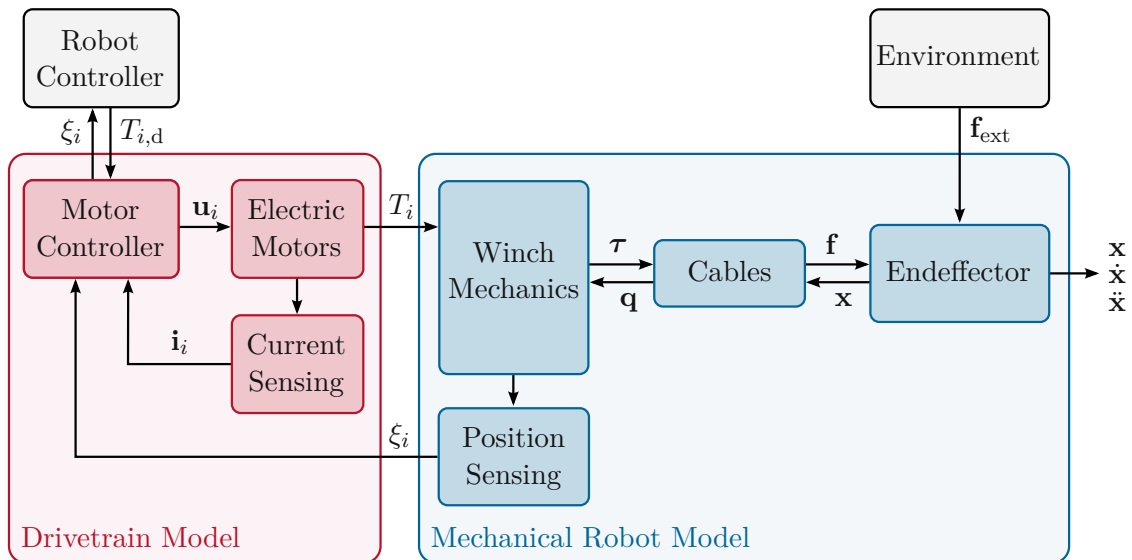
Figure 6.1: Mechatronic structure of the robot.

operates as a cascaded control loop. The motor controller receives a desired torque signal $M_{i,\mathrm{d}}$ for each electric motor from the high-level robot controller. In the inner control loop, the voltage $\mathbf{u}_i$ is controlled by the motor controller using the measured current $\mathbf{i}_i$ and the motor angles ξ_i as feedback. The torque produced by the electric motor (typically a permanent magnet synchronous motor) can be either inferred using an observer or measured directly using a dedicated torque sensor. Thus, the electric drivetrain provides the actual torques T_i to the mechanical robot system. In this work, the electrical drivetrain

is not further investigated, more details on modelling and controlling electrical drives can be found in the literature such as [31, 32].

The winch mechanics relate the torques T_i and angles ξ_i of the electric motors to the vector of cable forces $\boldsymbol{\tau}$ and the cable lengths $\mathbf{q}$. As a result of the cable forces, a wrench $\mathbf{f}$ on the EE is generated as derived in Eq. (3.17). Together with the external forces $\mathbf{f}_{\text{ext}}$, the wrench $\mathbf{f}$ dictates the EE motion $\mathbf{x}, \dot{\mathbf{x}}, \ddot{\mathbf{x}}$. The EE position $\mathbf{x}$ is related to the cable length $\mathbf{q}$ via the inverse kinematic transformation function $\boldsymbol{\phi}_{\text{ik}}$.

6.2 Winch mechanics

The winch converts the rotary motion of the electric motor into a linear motion of the cable. Figure 6.2 shows a conceptual drawing of the winch mechanism. The cable is deflected by a guiding pulley between the cable spool and the workspace. Since the radius of the guiding pulley is small compared to the dimensions of the workspace, this offset is neglected, see, e.g., [21]. For the sake of simplicity it is assumed that the winch mechanisms for all cables are identical and hence the index i is omitted in the following.
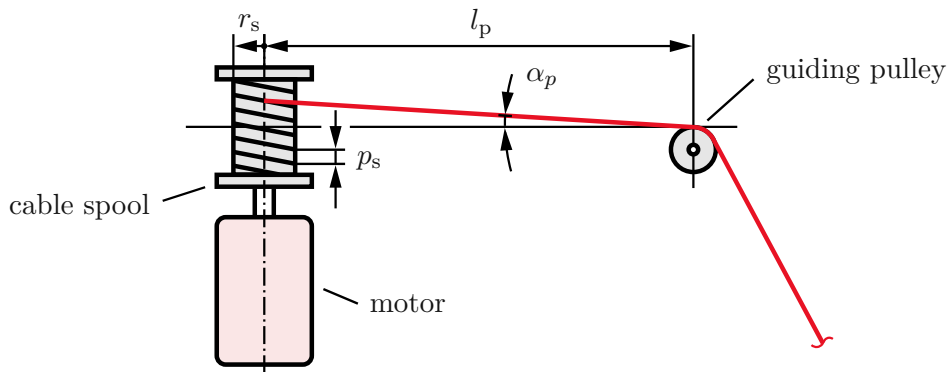
Figure 6.2: Cable winch mechanism.

The electric motor directly drives the cable spool, which has a helical groove that guides the cable when coiling it onto the spool. The helical groove has a pitch of p_{s} and an effective coiling radius of r_{s} which need to be taken into account for the calculation of the cable lengths. Thus, turning the motor by an angle of ξ will result in coiling the cable inside the helical groove by the length

$$\Delta l = \xi \underbrace{\sqrt{r_{\text{s}}^2 + \left(\frac{p_{\text{s}}}{2\pi}\right)^2}}_{\nu_{\text{w}}} = \xi \nu_{\text{w}} \,. \tag{6.1}$$

The resulting winch transmission ratio ν_{w} establishes the relation between the motor angle ξ and the change of the cable length Δl.

Due to the pitch of the helical groove, an additional nonlinear change of the cable length is introduced by the change of the cable angle α_{p}, see Figure 6.2. Hence, the total change

of the cable length can be written in the form

$$\Delta l = \xi \nu_{\text{w}} + \underbrace{\sqrt{l_{\text{p}}^2 + \left(\frac{p_{\text{s}}}{2\pi}\xi\right)^2} - l_{\text{p}}}_{e_{\text{p}}} \; . \tag{6.2}$$

Subsequently, the nonlinear pulley error e_{p} is neglected since the distance between the cable spool and the guiding pulley l_{p} is assumed to be large compared to the total height of the cable spool. In particular, this assumption is valid for the winch system employed in the prototype robot presented in Section 8.1. Based on this assumption, the relation between the rotary motion of the motors and the linear motion of the cables can be considered linear according to Eq. (6.1).

The inertia of all rotating components inside the motor (including couplings etc.) and the cable spool can be added. Thus, the total moment of inertia of the winch drivetrain

$$I_{\text{w}} = I_{\text{motor}} + I_s \tag{6.3}$$

is obtained where I_{motor} denotes the moment of inertia of the electric motor and I_s the moment of inertia of the spool.

6.3 Equations of motion

To derive the equations of motion for the mechanical system, the Newton-Euler equations can be applied. Alternatively to the method shown in the following, d'Alembert's principle can be used to obtain the equations of motion [33]. The derivation using d'Alembert's principle is shown in Appendix A.1.1. This formulation is particularly convenient when the model should be extended or when multiple physical domains should be integrated into the model at a later time.

To apply the Newton-Euler equations, the multibody system can be separated at the cables to obtain single body subsystems. Figure 6.3 depicts the resulting free-body diagram for the single body systems. The same assumptions as listed in Section 3.1 are employed for deriving the dynamic model. In particular, all bodies including the cables are considered rigid and thus all elastic deformations are neglected. In addition, the guiding pulley and the cables are considered massless and thus do not affect the transmission of the cable forces $\boldsymbol{\tau}$ from the cable spool to the EE. Hence, the guiding pulley can be omitted from the free-body diagram. In the control-oriented model, all dissipative effects are neglected and it is assumed that the inertial forces are large compared to dissipative forces. This includes the friction in the bearings of the winch system, the friction between the EE and the guiding plate as well as any aerodynamic effects. This assumption is relatively limiting because it is only valid if the accelerations of the EE are sufficiently large.

The balance of angular momentum for the cable spools reads as

$$I_{\text{w}}\ddot{\boldsymbol{\xi}} = \mathbf{T} + \nu_{\text{w}}\boldsymbol{\tau} \; , \tag{6.4}$$

with the vector of motor torques $\mathbf{T} \in \mathbb{R}^{n_q}$ and the moment of inertia I_{w} from Eq. (6.3), which is identical for all winches and accounts for all rotating parts.
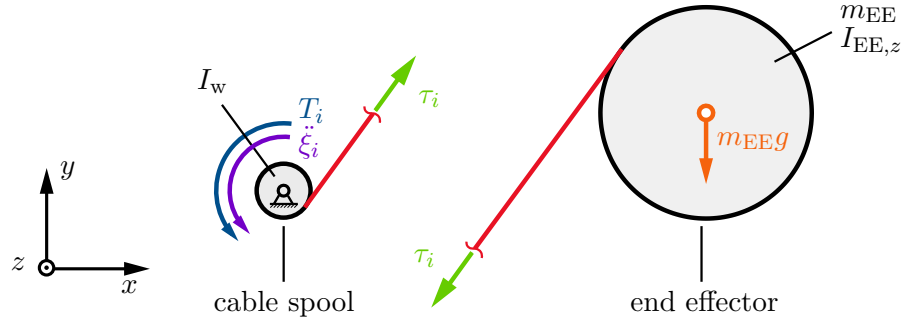
Figure 6.3: Free body diagram.

Similarly, the balance of momentum for the EE takes the form, see Eq. (3.17),

$$\mathbf{M}_{\text{EE}}\ddot{\mathbf{x}} = \mathbf{f} - \mathbf{g} = -\mathbf{J}_{\text{ik}}^{\text{T}}\boldsymbol{\tau} - \mathbf{g} \tag{6.5}$$

with the diagonal mass matrix

$$\mathbf{M}_{\text{EE}} = \begin{bmatrix} m_{\text{EE}} & 0 & 0 \\ 0 & m_{\text{EE}} & 0 \\ 0 & 0 & I_{\text{EE},z} \end{bmatrix} \tag{6.6}$$

consisting of the mass m_{EE} and the moment of inertia $I_{\text{EE},z}$ with respect to the z-axis of the EE. Moreover, $\mathbf{g}$ describes the gravitational force acting on the EE, i.e.

$$\mathbf{g} = \begin{bmatrix} 0 & m_{\text{EE}}g & 0 \end{bmatrix}^{\text{T}}, \tag{6.7}$$

with the gravitational acceleration g.

Combining the relations from Eqs. (3.19) and (6.1), the vector $\ddot{\boldsymbol{\xi}}$ can be expressed as

$$\ddot{\boldsymbol{\xi}} = \frac{\mathrm{d}}{\mathrm{d}t}\left(\frac{1}{\nu_{\text{w}}}\mathbf{J}_{\text{ik}}(\mathbf{x})\dot{\mathbf{x}}\right) = \frac{1}{\nu_{\text{w}}}\left(\dot{\mathbf{J}}_{\text{ik}}\dot{\mathbf{x}} + \mathbf{J}_{\text{ik}}\ddot{\mathbf{x}}\right). \tag{6.8}$$

Note that the time-derivative of the Jacobian of the inverse kinematics $\dot{\mathbf{J}}_{\text{ik}}$ is a function of $\mathbf{x}$ and $\dot{\mathbf{x}}$. It can be computed analytically in a closed form from the Jacobian matrix using Eq. (3.18).

Substituting Eq. (6.8) into Eq. (6.4), calculating $\boldsymbol{\tau}$ and inserting it into Eq. (6.5) results in the equations of motion

$$\underbrace{\left(\mathbf{M}_{\text{EE}} + \frac{I_{\text{w}}}{\nu_{\text{w}}^2}\mathbf{J}_{\text{ik}}^{\text{T}}\mathbf{J}_{\text{ik}}\right)}_{\mathbf{M}(\mathbf{x})}\ddot{\mathbf{x}} + \underbrace{\left(\frac{I_{\text{w}}}{\nu_{\text{w}}^2}\mathbf{J}_{\text{ik}}^{\text{T}}\dot{\mathbf{J}}_{\text{ik}}\right)}_{\mathbf{C}(\mathbf{x},\dot{\mathbf{x}})}\dot{\mathbf{x}} + \mathbf{g} = \underbrace{\frac{1}{\nu_{\text{w}}}\mathbf{J}_{\text{ik}}^{\text{T}}}_{\boldsymbol{\Lambda}(\mathbf{x})}\mathbf{T}, \tag{6.9}$$

with the positive definite mass matrix $\mathbf{M}(\mathbf{x})$, the Coriolis matrix $\mathbf{C}(\mathbf{x},\dot{\mathbf{x}})$ and the torque transformation matrix $\boldsymbol{\Lambda}(\mathbf{x})$.

7 Controller design

In this section, a trajectory following control strategy for the novel CDPR type is presented. The controller is based on the dynamic robot model from Chapter 6 and is used in Chapter 8 to demonstrate the performance of the novel CDPR concept and to validate the theoretical considerations. The control concept will be further elaborated in a follow-up master's thesis, where more details will be provided and an analysis of the controller's performance will be conducted. A more general discussion of different control concepts for robots can be found in [4, 34].

The controller follows a trajectory in the task space and stabilizes the trajectory tracking error defined as

$$\mathbf{e}_{\mathrm{x}} = \mathbf{x} - \mathbf{x}_{\mathrm{d}} \, , \tag{7.1}$$

where $\mathbf{x}_{\mathrm{d}}(t) \in \mathbb{R}^{n_x}$ denotes the desired trajectory of the EE pose. Due to the fundamental limitation that cables can only transmit pulling forces, special care must be taken when designing a controller for a CDPR. The control strategy must guarantee, that the constraint $\boldsymbol{\tau} > \boldsymbol{\tau}_{\mathrm{min}}$ is never violated to ensure sufficient tension in all cables at all times.

7.1 Control strategy

A valid cable force distribution, which satisfies the constraints while achieving a desired task-space wrench $\mathbf{f}_{\mathrm{d}}$, can be found by solving the optimization problem from Eq. (5.1). The cable force distribution function $\boldsymbol{\tau}^* : \mathbb{R}^{n_x} \to \mathbb{R}^{n_q}$ can thus be defined in the form

$$\begin{aligned}
\boldsymbol{\tau}^*(\mathbf{f}_{\mathrm{d}}) = \arg\min_{\boldsymbol{\tau}} \quad & \|\boldsymbol{\tau} - \boldsymbol{\tau}_{\mathrm{d}}\|_2 \\
\text{s.t.} \quad & \boldsymbol{\tau}_{\mathrm{min}} \leq \boldsymbol{\tau} \leq \boldsymbol{\tau}_{\mathrm{max}}, \\
& \mathbf{f}_{\mathrm{d}} = -\mathbf{J}_{\mathrm{ik}}^{\mathrm{T}} \boldsymbol{\tau} \, .
\end{aligned} \tag{7.2}$$

Applying this cable force distribution function $\boldsymbol{\tau}^*$ to the desired wrench $\mathbf{f}_{\mathrm{d}}$, guarantees valid cable forces and resolves the kinematic redundancies of the kinematically underdetermined system. More details on the numerical implementation of the force distribution function can be found in an upcoming follow-up thesis.

By rearranging Eq. (6.5), the desired wrench acting on the EE can be chosen in such a way, that the inertial forces for accelerating the EE given by $\mathbf{M}_{\mathrm{EE}}\ddot{\mathbf{x}}$ and the gravitational force $\mathbf{g}$ are compensated. A type of PD controller in the task space using these compensation terms thus takes the form

$$\mathbf{f}_{\mathrm{d}} = \mathbf{M}_{\mathrm{EE}}\ddot{\mathbf{x}}_{\mathrm{d}} + \mathbf{g} - \mathbf{K}_{\mathrm{P}}\mathbf{e}_{\mathrm{x}} - \mathbf{K}_{\mathrm{D}}\dot{\mathbf{e}}_{\mathrm{x}} \, , \tag{7.3}$$

where $\mathbf{K}_{\mathrm{P}}$ and $\mathbf{K}_{\mathrm{D}}$ denote the P (proportional) and D (derivative) gain matrices of the controller, respectively. In the literature, such a control scheme is often referred to as a so-called PD+ controller [35].

To compensate the inertial forces required to accelerate the rotating parts I_w, a compensation component is added by combining Eqs. (6.4) and (6.8). This results in the control law

$$\mathbf{T}_\mathrm{d} = \underbrace{-\nu_\mathrm{w} \; \boldsymbol{\tau}^*}_{\substack{\text{Force} \\ \text{Dist.}}} \underbrace{\left(\mathbf{M}_{\mathrm{EE}} \ddot{\mathbf{x}}_\mathrm{d} + \mathbf{g} - \mathbf{K}_\mathrm{P} \mathbf{e}_\mathrm{x} - \mathbf{K}_\mathrm{D} \dot{\mathbf{e}}_\mathrm{x} \right)}_{\substack{\text{PD+ for EE} \\ \text{Eq. (7.3)}}} + \underbrace{\frac{I_\mathrm{w}}{\nu_\mathrm{w}} \left(\dot{\mathbf{J}}_{\mathrm{ik}} \dot{\mathbf{x}}_\mathrm{d} + \mathbf{J}_{\mathrm{ik}} \ddot{\mathbf{x}}_\mathrm{d} \right)}_{\substack{\text{Winch Inertia} \\ \text{Compensation}}} . \qquad (7.4)$$

Here, the control variable $\mathbf{T}_\mathrm{d}$ denotes the desired torque, which acts as an input to the cascaded torque control. The PD+ control law for the EE from Eq. (7.3) corresponds to the forces, which must be transmitted by the cables. Thus, the force distribution function $\boldsymbol{\tau}^*$ must be applied to these forces to ensure that the resulting cable forces satisfy the constraints imposed by the cables. In contrast, the winch inertia compensation term in Eq. (7.4) can be applied directly to the motors without having to comply with any constraints. The structure of the resulting control system is visualized in Figure 7.1.
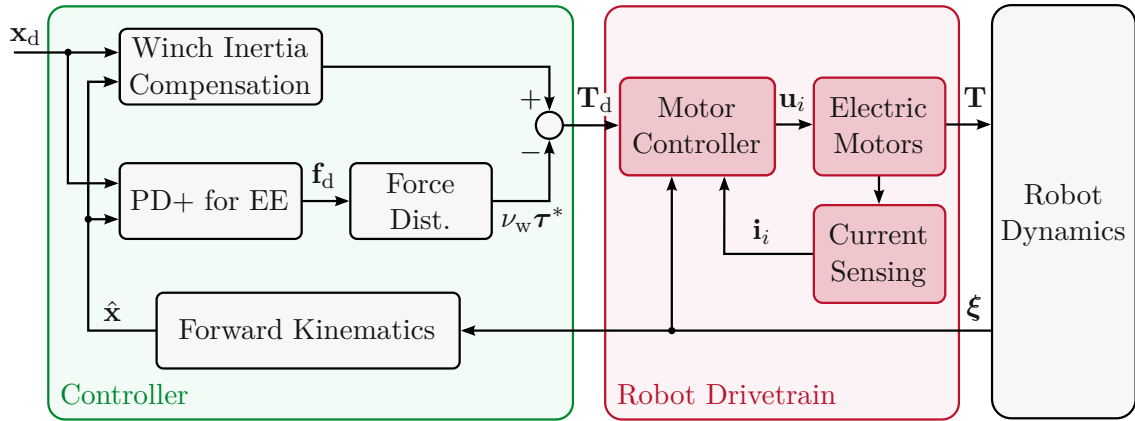
Figure 7.1: Structure of the control concept.

It is assumed in the following, that the torque dynamics of the drivetrain are significantly faster than the robot dynamics. Thus, the dynamics of the inner control loop can be neglected and it can be assumed $\mathbf{T} \approx \mathbf{T}_\mathrm{d}$.

Furthermore, it should be noted that the EE pose $\mathbf{x}$ cannot be measured directly and only the motor angles $\boldsymbol{\xi}$ are available as a measurement. Hence, the pose must be determined using the forward kinematics and $\hat{\mathbf{x}}$ must be used instead of $\mathbf{x}$. In the following, measurement errors are neglected and it is assumed that $\hat{\mathbf{x}} \approx \mathbf{x}$. de In case the optimization problem from Eq. (7.2) is infeasible and no valid solution $\boldsymbol{\tau}^*(\mathbf{f}_\mathrm{d})$ can be found, the CDPR must be halted to prevent damage due to inappropriate cable forces. To avoid this, special care must be taken that the trajectory is feasible within the dynamical capabilities of the robot.

7.2 Error dynamics and stability

To investigate the behavior of the closed loop system, the temporal evolution of the trajectory tracking error $\mathbf{e}_\mathrm{x}(t)$, defined in Eq. (7.1), is of great interest.

The control law from Eq. (7.4) can be substituted into the equations of motion from Eq. (6.9). Simplifying and grouping terms, assuming $\mathbf{x} = \hat{\mathbf{x}}$ and $\mathbf{T} = \mathbf{T}_\mathrm{d}$, yields the ordinary differential equation

$$\mathbf{M}(\mathbf{x})\ddot{\mathbf{e}}_\mathrm{x} + (\mathbf{C}(\mathbf{x},\dot{\mathbf{x}}) + \mathbf{K}_\mathrm{D})\dot{\mathbf{e}}_\mathrm{x} + \mathbf{K}_\mathrm{P}\mathbf{e}_\mathrm{x} = \mathbf{0} \ . \tag{7.5}$$

In control theory, this equation is referred to as *error dynamics* and the present form of Eq. (7.5) is characteristic and well-known for a PD+ controller.

By choosing the controller matrices $\mathbf{K}_\mathrm{P}$ and $\mathbf{K}_\mathrm{D}$ appropriately, the error dynamics can be adjusted as desired. Here, the term $(\mathbf{C}(\mathbf{x},\dot{\mathbf{x}}) + \mathbf{K}_\mathrm{D})$ can be interpreted as damping and $\mathbf{K}_\mathrm{P}$ represents the stiffness of the error system. Because the damping and the stiffness can be directly influenced, the PD+ controller in the task space can also be interpreted as a so-called compliance controller where the mechanical compliance of the robot along the trajectory can be chosen as desired.

It can be shown, that the trajectory tracking error $\mathbf{e}_\mathrm{x}$ is globally asymptotically stable for a symmetric and positive definite choice of $\mathbf{K}_\mathrm{P}$ and a positive definite $\mathbf{K}_\mathrm{D}$. The proof found in [36] uses a suitable Lyapunov function and a theorem of Matrosov. Note that the global asymptotic stability is retained even if the matrices $\mathbf{K}_\mathrm{D}$ and $\mathbf{K}_\mathrm{P}$ are time-variant. Thus, the controller matrices can be chosen such that the error dynamics become independent of the pose $\mathbf{x}$. For simplicity, the controller matrices $\mathbf{K}_\mathrm{D}$ and $\mathbf{K}_\mathrm{P}$ used in the prototype CDPR, presented in Section 8.1, are chosen constant and diagonal. The selected values are listed in Table A.3 found in the Appendix A.2.

8 Experimental results

In this chapter, experimental measurement data validating the theoretical considerations are presented. The experimental setup is outlined in Section 8.1. Thereafter, in Section 8.2, the measured positioning accuracy achieved using the forward kinematics solution from Chapter 4 is shown and discussed. The force efficiency studied in Section 5.2 is experimentally validated in Section 8.3 for a given task-space wrench. Finally the dynamic positioning performance of the prototype CDPR is evaluated in Section 8.4 for both translation and rotation.

8.1 Experimental robot prototype setup

In this section the implemented prototype robot, which demonstrates the performance and capabilities of the novel CDPR design, is presented. Mechanical aspects and details of the implementation of the robot are briefly outlined in the following. A list of parameters of the prototype CDPR can be found in Appendix A.2.

Figure 8.1 shows a photograph of the laboratory experiment. Here, the circular EE is realized by a common tournament dartboard with a mass of $4.45\,\text{kg}$ which is actuated by six winches. The design is based on a square frame, on which the winches and the guiding surface are mounted. The highlighted area in Figure 8.1 represents the theoretical wrench-closure workspace. Due to collisions with structural elements, the useful workspace of the prototype is smaller.

8.1.1 Winch design

The aim of the winch design is to actuate the cables in a mechanically simple but reliable way. Figure 8.2 provides an overview of the winch system. The winches are attached to the aluminum robot frame via mounting plates which are machined from stainless steel. The electrical drive system consists of Beckhoff AM8033 permanent magnet synchronous servomotors with a rated torque of $2.7\,\text{Nm}$ and a rated power of $1.7\,\text{kW}$ driven by Beckhoff AX8206 inverters in a cascaded torque control. Each motor directly drives a spool which has a helical groove and is 3D-printed from silver polylactide (PLA). The spool is reinforced with a steel tube and connected to the motor shaft via a clamping set. Additional considerations for choosing an appropriate winch transmission ratio are documented in Appendix A.1.2. The cable is guided by the 3D-printed PLA guiding pulley which is equipped with a ball-bearing and mounted directly to the aluminium frame.
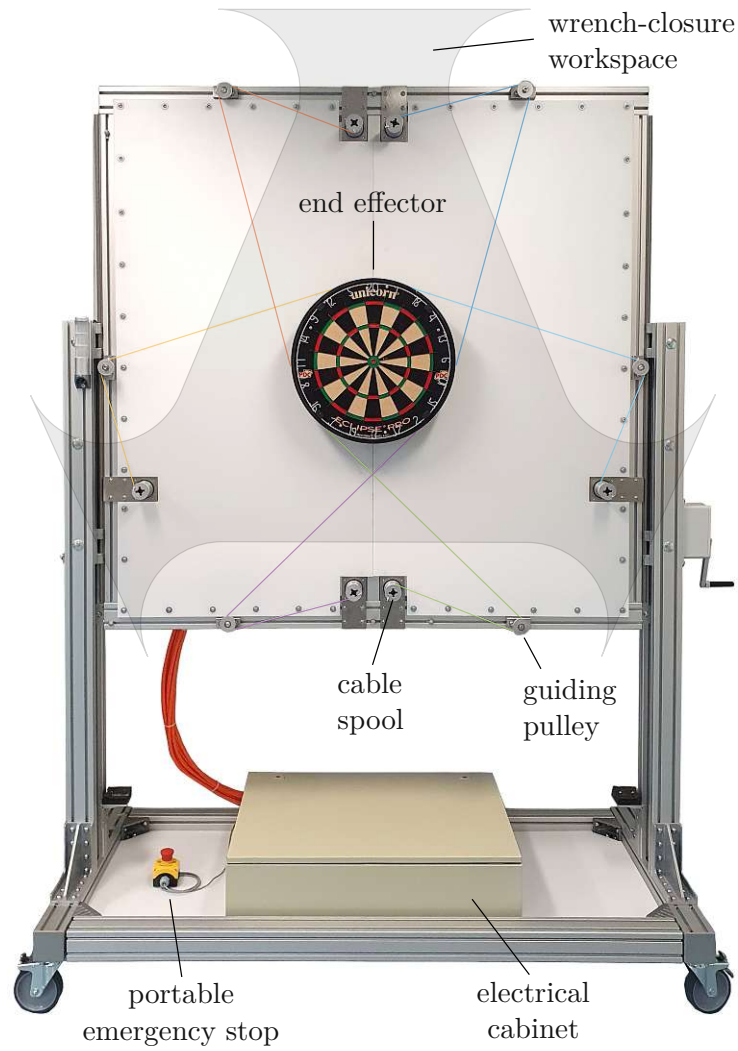
Figure 8.1: Front view of the robot prototype. The white cables are colored for better visibility.
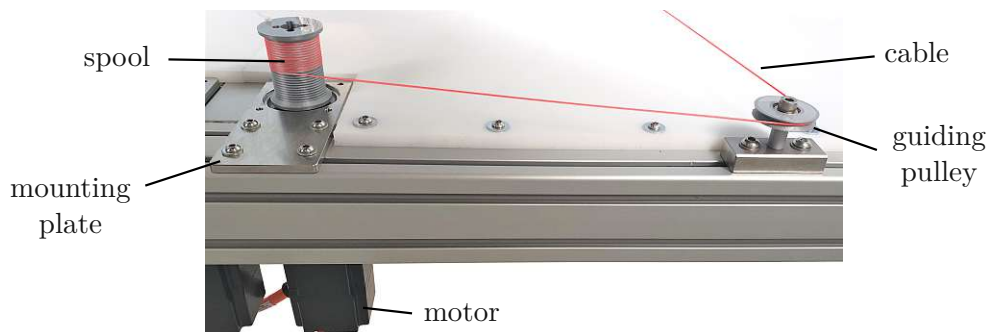
Figure 8.2: Winch design. The white cable is colored red for better visibility.

8.1.2 End effector design

The EE is composed of a tournament dartboard equipped with a fixture which incorporates guiding grooves for the cables, see Figure 8.3. The circular fixture is divided into six
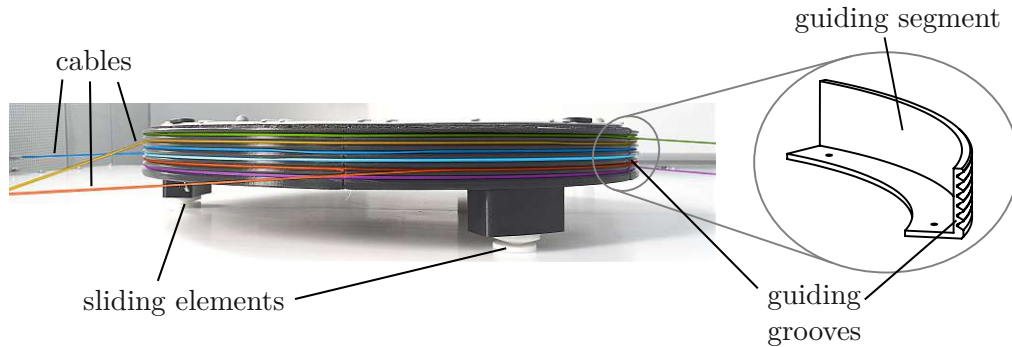
Figure 8.3: Design of the EE. The white cables are colored for better visibility.

segments which together create a circular shape. Each cable is attached to one segment and then wrapped around the designated groove. All guiding grooves must be shaped appropriately to ensure robust, stable, and reliable guidance of the cables withing the entire workspace of the robot. To prohibit the rotation of the EE around the x- and y-axis, the EE must be pushed towards the guiding surface with a sufficiently high force and hence the offset h_{A}, see Figure 3.1, must be chosen sufficiently large. However, large offsets cause larger deflection angles of the cables which need to be tolerated by the guiding grooves. Hence, the shape of the groove must ensure a reliable operation in the whole workspace. Finally, the depth of the guiding grooves must be chosen to accommodate the wrapped cable length l', see Section 2.1.

In the implemented CDPR prototype, each cable is wrapped around the EE in its own guiding groove. As a result, each cable has a different offset in z-direction from the guiding surface. To achieve an equal deflection angle for all cables when the EE is at the origin, the respective guiding pulleys are offset in z-direction accordingly, see Figure 8.4. The

Figure 8.4: Guiding surface. The white cables are colored for better visibility.

cable arrangement on the EE is chosen such that the tilting moments around the x- and y-axis, caused by the cable forces, have opposing directions for cables forming a weak pair. Two crossing cables form a weak pair as discussed in Section 5.1 and depicted in Figure 5.1. Consequently, very large forces are required to move the EE in the direction of a weak pair, which is also reflected by the low force efficiency in these directions as shown

in Section 5.2. Therefore, it is desirable to avoid tilting moments when moving in such a direction. For the presented CDPR configuration, the cables (s_1, s_6), (s_2, s_3) and (s_4, s_5) form weak pairs. Thus, with the cable layout shown in Figure 8.5 the dominating tilting moments around the x- and y-axis caused by the weak pairs are reduced for symmetrical forces in the associated cables of the weak pairs.
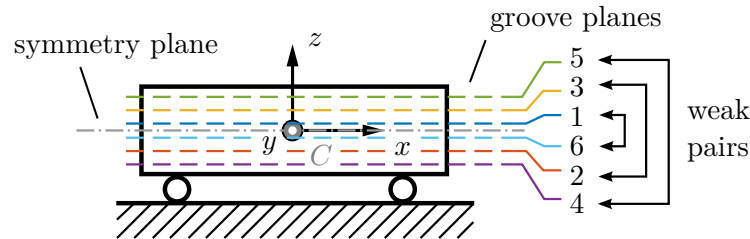
Figure 8.5: Cable arrangement.

To reduce the friction between the EE and the guiding surface, the EE is equipped with sliding elements. Figure 8.3 shows the location and design of the sliding elements attached to the EE. These sliding elements can be easily replaced for maintenance and can be adapted for the specific task by choosing designs with appropriate damping, stiffness and friction coefficients for the sliding elements.

8.1.3 Material choices

In the following, the most important material choices for the design and reliable operation of the proposed CDPR design are outlined. The cables are made of the material Dyneema SK78 (high-modulus polyethylene) which offers very high tensile strength, high stiffness, low creep and high durability under cyclic bending [37]. Because of these properties, Dyneema is very suitable and commonly used in CDPR applications [38]. The rated breaking load of the chosen cables (Liros D-Pro 1mm) is $1950\,\mathrm{N}$. The maximum working load $\tau_{\mathrm{max}} = 280\,\mathrm{N}$ ensures that the cable force does not exceed 15% of its breaking load to guarantee safe operation and long fatigue life of the cables.

For the guiding surface, the material polyethylene with high molecular weight (PE-HMW) was chosen. This material offers a low coefficient of friction while being scratch resistant and durable [39]. To reduce the amount of friction between the EE and the guiding surface, different sliding elements can be used. Figure 8.6 shows two optional sliding elements used for the robot. While the polymer ball transfer units (igus xiros) offer low rolling friction and high stiffness in z-direction, the felt sliding pads exhibit a lower stiffness, but achieve higher damping and allow for silent operation with a very low increase in friction. For all subsequent experiments, the felt sliding pads are employed.

8.2 Forward kinematics positioning accuracy

In this section, the positioning accuracy of the forward kinematics presented in Chapter 4 is investigated. Thus the modeling assumptions used to derive the forward kinematics algorithm are evaluated and the solution is validated.

Figure 8.6: Sliding elements compared to a 1 Euro coin.

The accuracy is evaluated via the position error e_C defined in Eq. (4.34). For this purpose, the position of the EE $\mathbf{r}_C$ is measured using a commercial motion tracking camera system consisting of six *Optitrack Prime 17W* cameras. The cameras are positioned around the robot and reflective infrared (IR) markers are attached to the EE and the robot frame. Figure 8.7(a) indicates the placement of the optical markers on the EE with green squares and the location of the markers on the aluminium frame of the CDPR using red circles. While the markers attached to the EE are used to track its location and orientation very robustly, the markers on the frame are used for aligning the coordinate system of the optical tracking system with the CDPR coordinate system during calibration. Furthermore, the markers on the CDPR frame are used to compensate for coordinate system drift and vibrations of the frame.

The estimated position $\hat{\mathbf{r}}_C$ is computed from the cable lengths measured by absolute encoders connected to the motor shafts of the driving motors using the forward kinematics algorithm presented in Chapter 4.

Measurements are taken on a grid of 20×20 equidistant points in the inner workspace $\mathcal{U}$ which is defined as

$$\mathcal{U} = \{\mathbf{x} \mid x_C \in [-0.25\,\mathrm{m}, 0.25\,\mathrm{m}], \ y_C \in [-0.25\,\mathrm{m}, 0.25\,\mathrm{m}]\}. \tag{8.1}$$
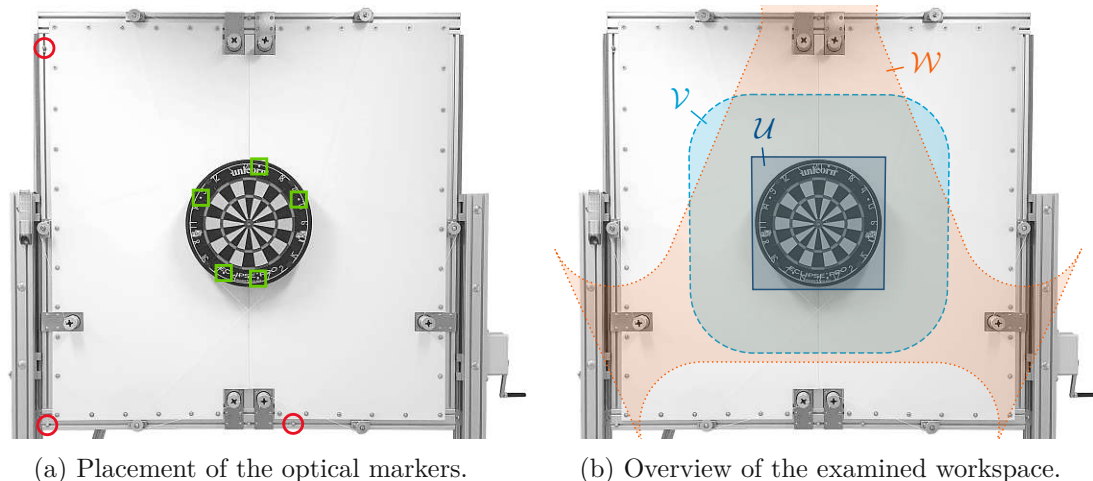
(a) Placement of the optical markers.   (b) Overview of the examined workspace.

Figure 8.7: Experiment design for measuring the positioning accuracy.

For all poses in the inner workspace $\mathcal{U}$, the collision region $\mathcal{V}$ corresponds to the outer boundary which contains all points of the EE and thus serves as a tool to analyze collision margins between the EE and other structural components. The set $\mathcal{V}$ can be formally defined as

$$\mathcal{V} = \{\mathbf{x} + [x, y, \varphi]^{\mathrm{T}} \mid \mathbf{x} \in \mathcal{U}, \ x^2 + y^2 \leq r\} \ . \tag{8.2}$$

The examined inner workspace $\mathcal{U}$, the corresponding collision region $\mathcal{V}$ as well as the wrench-closure workspace $\mathcal{W}$ are visualized in Figure 8.7(b).

The position error on the measured grid in the region $\mathcal{U}$ is depicted in Figure 8.8 as a heatmap. Here it is visible that a positioning accuracy of $< 1\,\mathrm{mm}$ can be achieved in a large portion of the workspace. For the center of the workspace $\mathcal{U}$, the positioning accuracy is similar to the accuracy of the optical measurement system of $\pm 0.3\,\mathrm{mm}$. The position error close to the top corners reaches values of $\approx 1.2\,\mathrm{mm}$ and reaches a peak value of $2.3\,\mathrm{mm}$ in the top right corner. This sharp increase in the position error e_C can be explained by the increasing cable forces in the weak cable pair (s_1, s_6), which are necessary to counteract gravity. These forces are the cause for two main effects which are considered the main source of the position error. First, the large cable forces cause an elastic elongation in the cables which is neglected in the standard model used to derive the forward kinematics. Second, the large cable forces cause tilting moments M_x and M_y which cause the felt sliding pads to deform slightly and even to visibly lift off the guiding surface in point $\mathbf{x} = [0.25\,\mathrm{m}, 0.25\,\mathrm{m}, 0\,\mathrm{rad}]$ located in the top right corner of the investigated workspace $\mathcal{U}$.
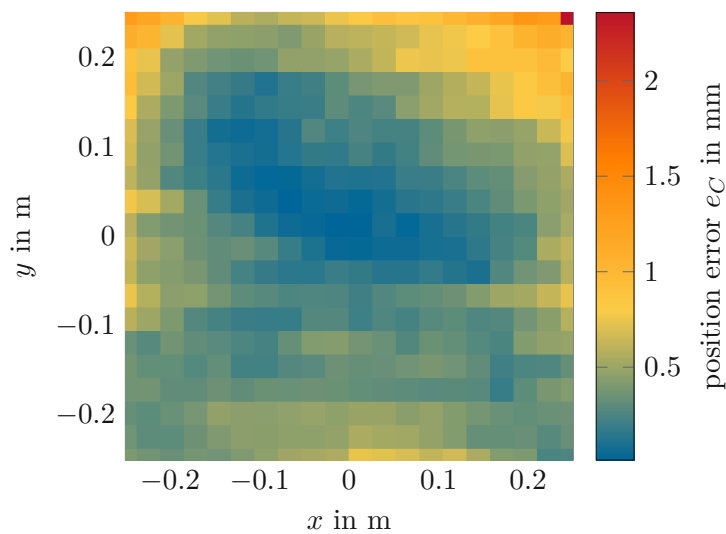
Figure 8.8: Error map of the forward kinematics error.

The experimental results show that a sub-millimeter positioning accuracy can be achieved by the CDPR developed in this work which is sufficient for many general purpose positioning tasks. To obtain higher accuracy, the stiffness of the sliding pads could be increased and the robot model could be extended to take the deformations of the cables into account. To avoid tilting of the EE, the sliding elements could be enlarged or more

sliding elements can be added to the EE which would result in a higher robustness with respect to tilting torques.

8.3 Force efficiency experiment

In this section, the force efficiency measure η discussed in Section 5.2 is applied and validated using experimental data. The gravitational force on the EE is used as loading force to demonstrate that the predicted force efficiency is actually achieved in practice. Hence, it is shown that the force efficiency measure can be applied as a useful tool to analyze the capabilities of the robot inside its workspace.

A positioning task with a small and constant velocity is performed, such that the inertial forces on the EE are negligible and the dominant force is the gravitational force.

The EE is moved from the pose $\mathbf{x}_1$ to the pose $\mathbf{x}_2$ which are chosen as

$$\mathbf{x}_1 = \begin{bmatrix} 0\,\mathrm{m} & -0.3\,\mathrm{m} & 0\,\mathrm{rad} \end{bmatrix}^\mathrm{T}, \qquad \mathbf{x}_2 = \begin{bmatrix} 0.3\,\mathrm{m} & 0.2\,\mathrm{m} & 0\,\mathrm{rad} \end{bmatrix}^\mathrm{T}. \tag{8.3}$$

A linear task-space trajectory with a constant desired velocity of $v_\mathrm{d} = 0.1\,\mathrm{m/s}$ is used as shown in Figure 8.9(c). The poses of the robot are depicted in Figure 8.9(a). To analyze this task, the force efficiency for the wrench according to Eq. (5.9)

$$\mathbf{f}_\mathrm{d} = \mathbf{g} = \begin{bmatrix} 0 & m_{EE}g & 0 \end{bmatrix}^\mathrm{T} = \begin{bmatrix} 0 & 43.65\,\mathrm{N} & 0 \end{bmatrix}^\mathrm{T} \tag{8.4}$$

is shown in Figure 8.9(b). Here, the limit of the cable forces $\tau_\mathrm{min} = 10\,\mathrm{N}$, and the desired cable forces $\tau_\mathrm{d} = 50\,\mathrm{N}$ are considered in the cable force-distribution function, see Eq. (7.2), which is part of the controller outlined in Chapter 7.

The experiment can be divided into three sections. In section ①, the pose of the EE is constant at $\mathbf{x}_1$. In this pose, the cables are symmetrical with respect to the y-axis due to the symmetry of the robot as visualized in Figure 8.9(a). The force due to the gravitational acceleration on the EE acts along this axis of symmetry in negative y-direction. As a consequence, the cable forces of the corresponding pairs (s_1, s_2), (s_3, s_6), (s_4, s_5) are equal. The measured cable forces τ_i, $i = 1, \ldots, 6$ are shown in Figure 8.9(d). Some very small deviations between the corresponding cables are visible which are caused by static friction effects.

In section ②, which is divided in ②a and ②b, the EE moves with a constant velocity as shown in Figure 8.9(c).

During the movement across the workspace the force efficiency gradually changes as visible in Figure 8.9(b) and Figure 8.9(e). The change in the force efficiency is directly related to the change in the maximum cable force which is necessary to counteract the gravitational force on the EE. The relation becomes apparent when comparing the cable forces shown in Figure 8.9(d) with the force efficiency depicted in Figure 8.9(e).

In section ②b, the force efficiency decreases rapidly, consequently the cable forces increase at the same rate. This decrease in efficiency is caused by the cable forces τ_3 and τ_4 reaching the lower limit τ_min. A reduction of the opposing cable forces τ_3 and τ_4 can be interpreted as instantaneous pushing forces on the EE. As soon as these forces reach the lower limit and no more reduction is possible, the cables s_1 and s_6 need to exert even
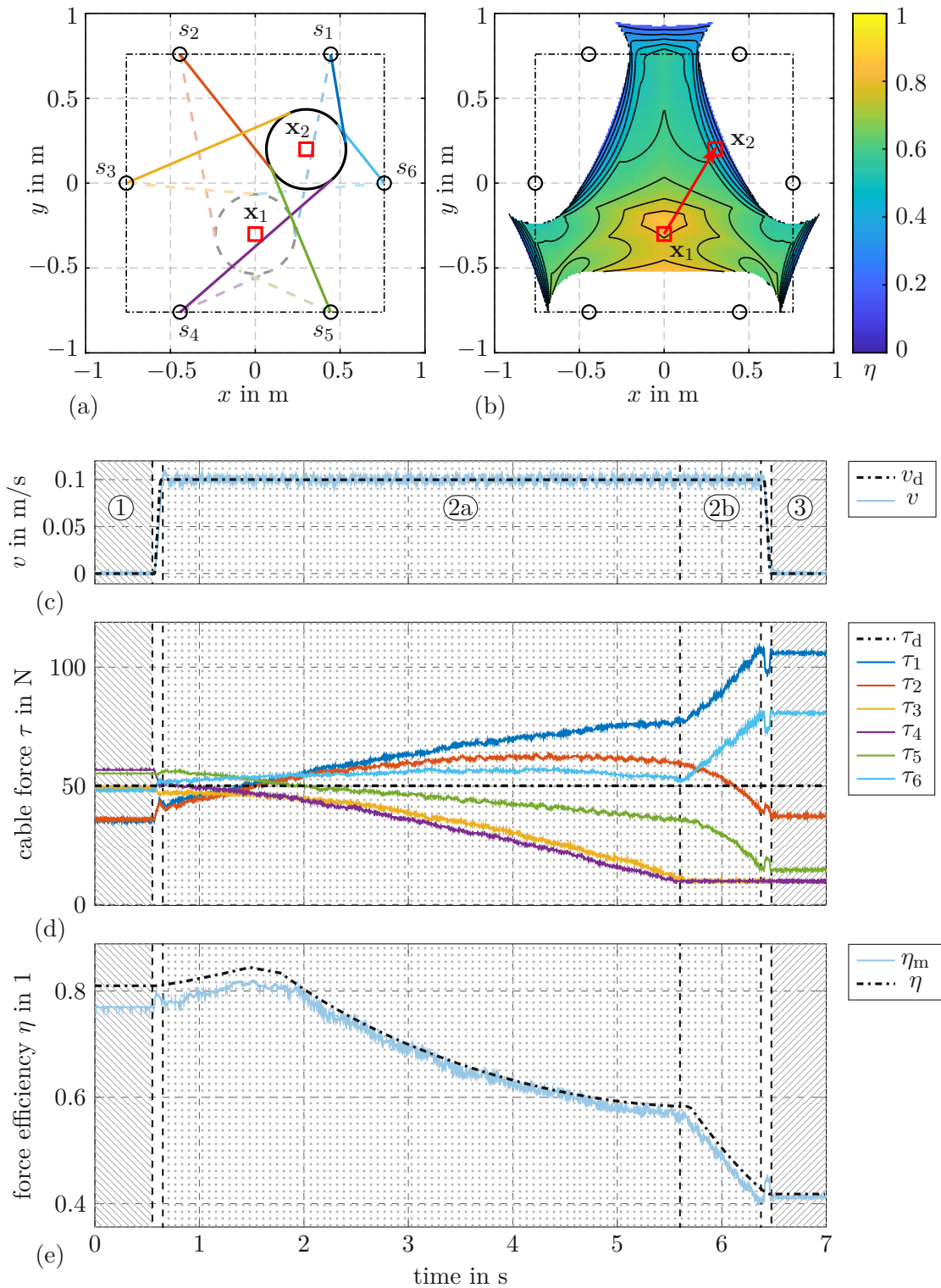
Figure 8.9: Experimental results: (a) Poses $\mathbf{x}_1$ and $\mathbf{x}_2$. (b) Force efficiency ($\mathbf{d} = \mathbf{e}_y$). (c) Velocity $v = \sqrt{\dot{x}_C^2 + \dot{y}_C^2}$. (d) Measured cable forces. (e) Force efficiency.

higher forces to counteract gravity as the trajectory progresses. Due to the geometry of the robot, (s_1, s_6) form a weak pair and thus very large forces are required in these cables. Since the force distribution algorithm is considered in the computation of the force efficiency, the aforementioned cable force limits are accurately reflected in the force efficiency value.

In section ③, the pose of the EE is constant at $\mathbf{x}_2$. The force efficiency in this pose is approximately half the force efficiency of pose $\mathbf{x}_1$ as shown in Figure 8.9(e). Consequently, the maximum of the cable forces is approximately twice as high, see Figure 8.9(d). In this pose, the load caused by gravity is distributed asymmetrically between the cables because the cable geometry in the pose $\mathbf{x}_1$ is asymmetric and thus there are no cable pairs exerting the same force.

Between section ① and ②a as well as ②b and ③ the EE has to be accelerated and decelerated respectively, as depicted in the velocity profile in Figure 8.9(c). Hence, the required inertial forces are provided by the cable forces shown in Figure 8.9(d).

The force efficiency from Eq. (5.9) along the trajectory can be estimated by using the measured cable forces and the known force due to gravity. In Figure 8.9(d), the measured force efficiency η_m is compared to the theoretical value. The measured progression of the force efficiency η_m is slightly lower than the theoretical η calculated for a pure gravitational load in negative y-direction. This discrepancy can be explained by the friction forces between the EE and the guiding surface and friction torques in the bearings which result in smaller effective forces available for counteracting the gravitational force on the EE. The cable force is measured indirectly utilizing the motor current, which also introduces some uncertainty. In general, the measured curve matches the expected theoretical force efficiency and validates the observations made in the system analysis.

8.4 Dynamic positioning performance

To demonstrate the performance of the novel CDPR design, different highly dynamic positioning tasks are performed and compared. In Section 8.4.1, the EE is moved along a linear trajectory in two selected directions in order to demonstrate that the EE can be positioned quickly inside the workspace. The capabilities of the CDPR to facilitate rotational motion are demonstrated in Section 8.4.2.

8.4.1 Translational motion

Starting from the origin $\mathbf{x}_0 = \mathbf{0}$, the EE is moved along a linear trajectory in the task space to the poses

$$\mathbf{x}_\mathrm{A} = \begin{bmatrix} 0.26\,\mathrm{m} & 0.15\,\mathrm{m} & 0\,\mathrm{rad} \end{bmatrix}^\mathrm{T}, \qquad \mathbf{x}_\mathrm{B} = \begin{bmatrix} 0\,\mathrm{m} & 0.3\,\mathrm{m} & 0\,\mathrm{rad} \end{bmatrix}^\mathrm{T}. \qquad (8.5)$$

The motion to $\mathbf{x}_\mathrm{A}$ shown in Figure 8.10(a) corresponds to the motion towards the weak pair (s_1, s_6) against gravity and can be interpreted as the most undesirable positioning task for the CDPR prototype. For comparison, the motion to $\mathbf{x}_\mathrm{B}$ depicted in Figure 8.10(b) corresponds to the motion towards the strong pair (s_1, s_2) but in this case the full

gravitational force has to be overcome. Hence the two positioning tasks can be seen as worst-case scenarios and are representative for all other possible positioning tasks.

The velocity profiles for the linear trajectories are shown in Figure 8.10(c) where v_d denotes the desired velocity along the trajectory. The chosen trajectory $\mathbf{x}_\mathrm{d}$ is three times continuously differentiable such that the jerk along the trajectory is bounded and well defined at all times. The acceleration along the trajectory is limited to $30\,\mathrm{m/s^2}$ and the velocity is limited to $2\,\mathrm{m/s}$. This results in a total duration of less than $250\,\mathrm{ms}$ for the positioning task. The cable forces for the motion to $\mathbf{x}_\mathrm{A}$ are depicted in Figure 8.10(d) and the cable forces for $\mathbf{x}_\mathrm{B}$ are shown in Figure 8.10(e).

The motion can be divided into three steps. In ① the EE accelerates with a maximum acceleration of $30\,\mathrm{m/s^2}$. To achieve this acceleration and also overcome gravitational and friction forces, the cable forces must deviate from the desired cable force $\tau_\mathrm{d} = 50\,\mathrm{N}$ such that a resulting net force on the EE is created. While the forces in cables opposing the EE motion must be reduced, the cable forces in the direction of motion must be increased for this purpose. For trajectory A which is shown in Figure 8.10(a), the strong cable pair (s_3, s_4) is opposing the motion whereas the weak cable pair (s_1, s_6) acts in the direction of motion. As a result, the forces (τ_3, τ_4) are reduced and (τ_1, τ_6) are increased as shown in Figure 8.10(d). In contrast, for trajectory B depicted in 8.10(b), the weak pair (s_4, s_5) opposes the direction of motion while the strong pair (s_1, s_2) acts in the direction of motion. Hence, the forces (τ_4, τ_5) are reduced and (τ_1, τ_2) are increased as visible in Figure 8.10(e). When comparing the forces for the two trajectories shown in Figure 8.10(d) and 8.10(e), it can be seen that higher magnitudes of forces are necessary for trajectory A than for trajectory B despite the necessity of overcoming a larger portion of the gravitational force in trajectory B. This difference is a result of the direction of motion which lies in the direction of a weak pair for trajectory A and in the direction of a strong pair in trajectory B. The CDPR is able to apply wrenches more efficiently in the direction of trajectory B than in the direction of trajectory A, as predicted by the force efficiency shown in Figure 5.5(a).

Because trajectory B follows the vertical symmetry axis of the CDPR, the cable forces are also symmetrical and act in pairs as visible in Figure 8.10(e). The discrepancy at the beginning of the motion when the EE is stationary at the origin $\mathbf{x}_0$ is caused by asymmetrical friction forces. Trajectory A does not follow any symmetry and hence the cable forces only form pairs at the origin $\mathbf{x}_0$.

8.4.2 Rotational motion

To demonstrate the performance of the CDPR for rotational motion, the EE is rotated by $90\,\mathrm{deg}$ at the center of the workspace from the origin $\mathbf{x}_0 = \mathbf{0}$ to the pose

$$\mathbf{x}_\varphi = \begin{bmatrix} 0\,\mathrm{m} & 0\,\mathrm{m} & \frac{\pi}{2}\mathrm{rad} \end{bmatrix}^\mathrm{T}. \tag{8.6}$$

The trajectory of the angular velocity $\dot\varphi_\mathrm{d}$ and the measured angular velocity $\dot\varphi$ are depicted in Figure 8.11(a). The maximum angular acceleration $\ddot\varphi_\mathrm{d}$ is limited to $120\,\mathrm{rad/s^2}$ and the angular velocity limit is chosen as $12\,\mathrm{rad/s}$. Figure 8.11(b) shows the cable forces
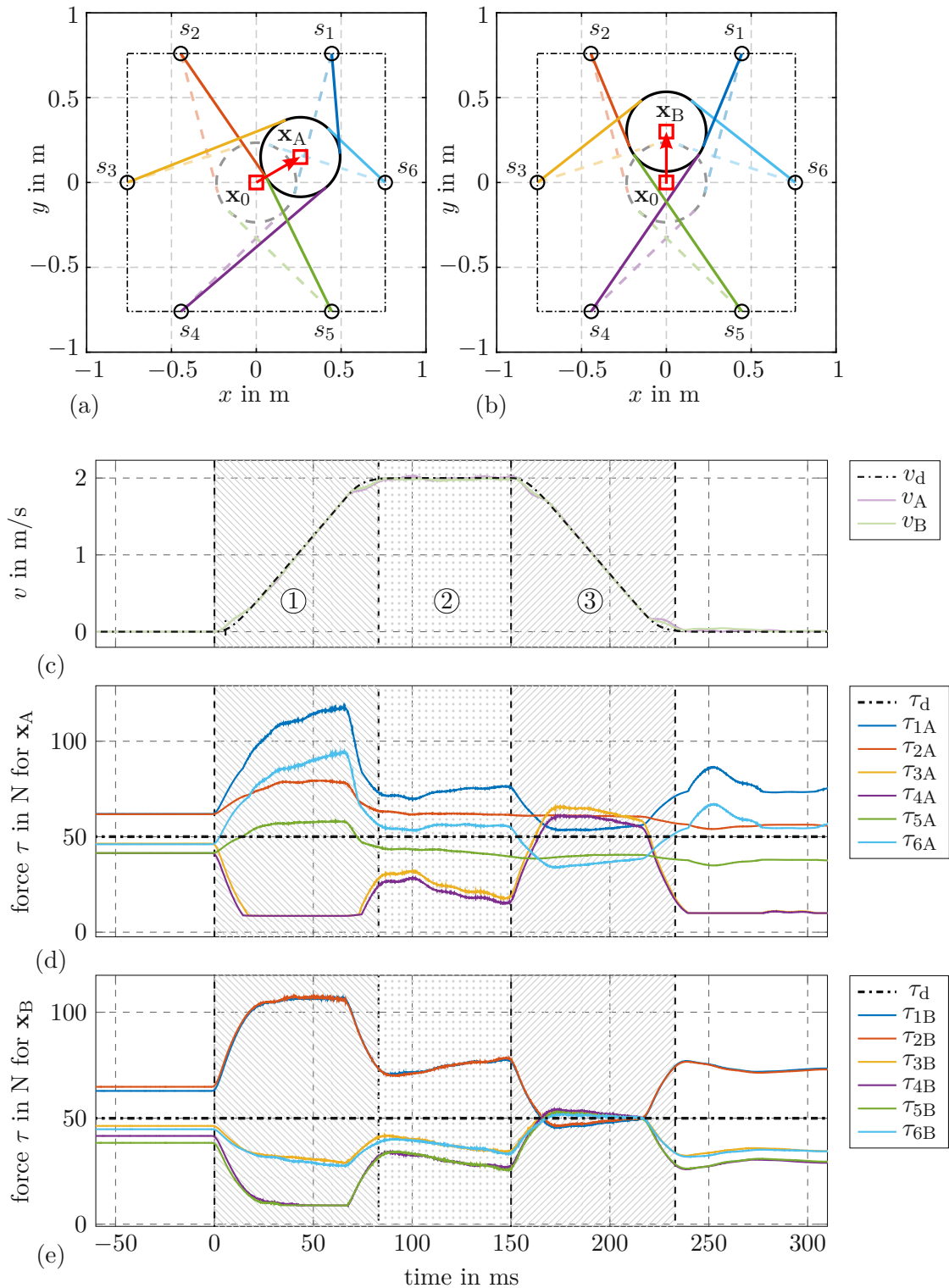
Figure 8.10: Experimental results: (a) Poses $\mathbf{x}_0$ and $\mathbf{x}_A$. (b) Poses $\mathbf{x}_0$ and $\mathbf{x}_B$. (c) Velocity $v = \sqrt{\dot{x}_C^2 + \dot{y}_C^2}$. (d) Cable forces for x_A. (e) Cable Forces for x_B.

τ_i, $i = 1, \ldots, 6$ for following the trajectory. Using these dynamic limits, the motion requires approximately 250 ms to complete.
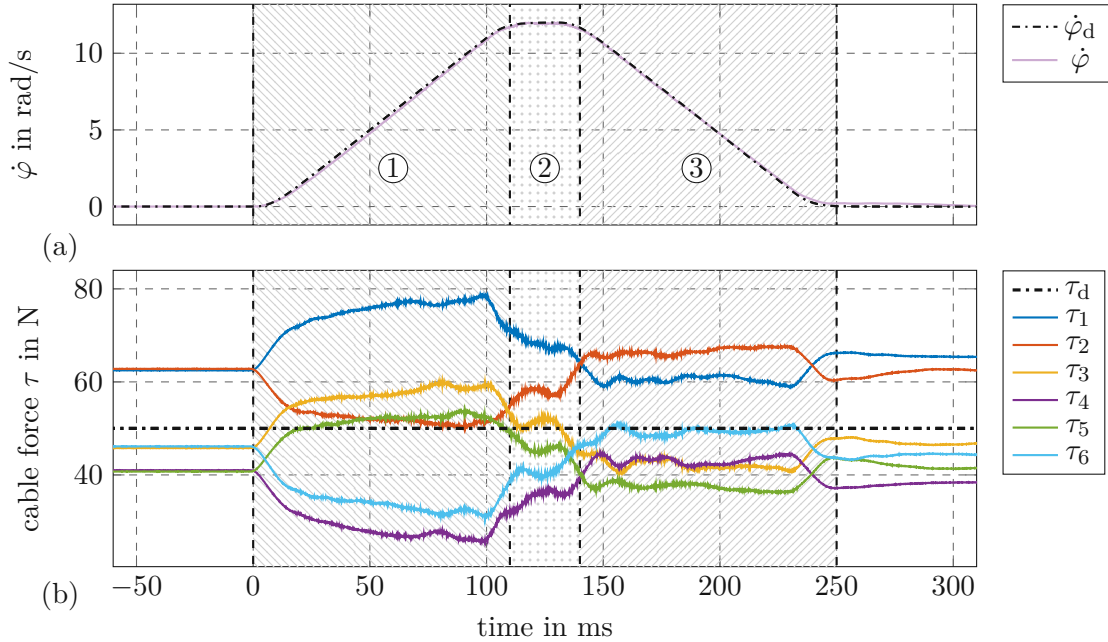

Figure 8.11: Experimental results: (a) Angular velocity $\dot{\varphi}$. (b) Cable forces.

The motion can be divided into 3 sections. In ① the EE accelerates until it reaches the maximum angular velocity. Due to the symmetry at the origin, the cable forces (τ_1, τ_2), (τ_3, τ_4) and (τ_5, τ_6) form pairs and start with equal values. The two cables in each pair have opposing winding directions i.e. $(s_1 = -s_2)$, $(s_3 = -s_4)$ and $(s_5 = -s_6)$. Thus the torque M_z acting on the EE vanishes for equal forces in the pairs, see Eq. (3.13). To achieve a net torque $M_z > 0$ on the EE to overcome friction and provide the required inertial forces, the cable pairs need to exert different forces on the EE i.e. the forces in cables wrapped CCW ($s_1 = s_3 = s_5 = 1$) need to increase while the forces in CW cables ($s_2 = s_4 = s_6 = -1$) need to decrease. This is clearly visible in Section ① in Figure 8.11(b).

In ②, the maximum angular velocity is reached and the EE rotates at constant velocity as visible in Figure 8.11(a). The net torque M_z decreases but is still greater than zero because the EE must overcome friction forces to maintain its angular velocity. Hence the difference of the cable forces in the pairs (τ_1, τ_2), (τ_3, τ_4) and (τ_5, τ_6) decreases in ② compared to ① as shown in Figure 8.11(b).

In Section ③ the EE decelerates until it reaches a velocity of zero. During deceleration the net torque $M_z < 0$ to provide the necessary inertial forces to follow the trajectory. However, the friction forces actively slow down the EE in ③ and thus the magnitude of the torque is lower than in Section ①. This is clearly visible in Figure 8.11(b).

When the EE reaches a velocity of zero, the cable forces reach an equilibrium at which they remain until the end of the experiment. Note that these equilibrium forces are not equal to the forces at the beginning of the experiment and there is a net torque $M_z > 0$

acting on the EE at the end of the experiment. This is caused by static friction which causes the EE to stop at an angle φ which is slightly deviates from the target angle $\frac{\pi}{2}$.

9 Conclusion and outlook

In this work, a novel planar cable driven parallel robot (CDPR) concept was investigated which allows for arbitrary rotation of the end effector (EE). By wrapping the cables around a cylindrical fixture attached to the EE, the CDPR achieves large rotations without adding any moving parts to the robot which results in a mechanically simple and robust design.

The geometry of the CDPR concept was analyzed and the inverse kinematic problem was solved in Chapter 3. The inverse kinematics solution is computationally inexpensive and because each cable can be treated independently, the computational effort scales linearly with the number of cables. The inverse kinematics algorithm always has a unique real-valued solution for feasible poses and yields complex solutions for poses which are not physically feasible. Furthermore, a differential kinematic description of the robot in the form of the Jacobian matrix of the inverse kinematics was derived.

A solution of the forward kinematics was presented in Chapter 4 which demonstrated that the forward kinematics for the novel CDPR concept can be geometrically interpreted as the intersection of modified involute curves. The forward kinematics problem was formulated as a nonlinear least-squared problem and a robust solution algorithm was developed which uses bounding boxes to obtain an initial estimate for the EE pose. The convergence behavior and the impact of measurement noise on the forward kinematics solution was investigated using simulations. The algorithm showed very robust convergence behavior and a convergence region which almost covers the entire wrench-closure workspace. Furthermore, the algorithm was found to be robust with respect to noise. If the forward kinematic algorithm fails to find a valid solution, the error is detectable via the residual error value and the robot can be safely halted.

To analyze the workspace of the CDPR concept, classical manipulability measures found in the literature were found to be unsuitable and thus the force efficiency measure was applied to investigate the workspace of different CDPR designs in Chapter 5. Three different candidate designs were studied and the structure of the workspace was generalized for the novel CDPR concept via strong and weak cable pairs. The workspace of CDPRs using uneven numbers of cables was considered and compared to the workspace of CDPRs with even numbers of cables. Based on the theoretical considerations, a design candidate was selected for the realization of a prototype robot.

A control-oriented dynamical model was developed in Chapter 6 and used in Chapter 7 to design a trajectory following controller for the CDPR. The control concept has a so-called 'PD+'structure and exhibits global asymptotic stability.

In Chapter 8 an experimental prototype robot was designed and presented. The forward kinematics solution algorithm and the force efficiency were validated using experimental data and the performance and practicality of the CDPR design was demonstrated. A positioning accuracy of $< 1\,\mathrm{mm}$ could be achieved within most of the workspace.

In a follow-up master's thesis, the CDPR prototype will be successfully applied to catch a flying dart thrown by a human. For this purpose, the controller outlined in Chapter 7 will be discussed in more detail and a trajectory generator will be presented which is able to dynamically adapt and recalculate the trajectory. A tracking algorithm will be proposed to predict the impact location of the dart. The trajectory can then be adapted in real-time such that the dartboard attached to the EE is moved accordingly to hit any desired field.

Further development of the CDPR concept could focus on extending the dynamical model. By incorporating cable deformations, the positioning accuracy could potentially be improved significantly. Furthermore, dissipative effects such as friction could be considered, to improve the fidelity of the model in particular for slow movements with small accelerations.

In future work, the design of the guiding system could be improved to reduce friction between the EE and the guiding system and avoid tilting of the EE. The possibility of using different gliding elements, air bearings or magnetic levitation could be investigated. Further research effort could be assigned to study possible methods for using cables wrapped around the EE of a three dimensional CDPR.

A Appendix

A.1 Additional derivations

A.1.1 Equations of motion using d'Alembert's principle

To derive the equations of motion, d'Alembert's principle in the Lagrangian formulation

$$
\underbrace{\delta W}_{\text{external}} = \underbrace{\int_m \ddot{\mathbf{r}}_P \cdot \delta \mathbf{r}_P \, \mathrm{d}m}_{\text{inertial}} + \underbrace{\delta V}_{\text{potential}} \tag{A.1}
$$

can be used [33]. Here, m denotes the mass of the moving parts including the EE and all spinning parts of the winches. The principle states that the virtual work done by the external forces δW is equal to the virtual work done by the inertial forces and the variation of the potential δV of all conservative forces present in the system, for an arbitrary virtual displacement which is compliant with the kinematic constraints.

The variation of equation (3.15) yields a relation between a virtual displacement $\delta \mathbf{x}$ of the EE and a virtual displacement of the cable lengths $\delta \mathbf{q}$ in the form

$$
\delta \mathbf{q} = \mathbf{J}_{\mathrm{ik}} \delta \mathbf{x} \; . \tag{A.2}
$$

The relation between a virtual displacement of the motor angles $\delta \boldsymbol{\xi}$ and a virtual displacement of the joint coordinates $\delta \mathbf{q}$ is defined in (6.1) and reads as

$$
\delta \boldsymbol{\xi} = \frac{1}{\nu_{\mathrm{w}}} \delta \mathbf{q} \; . \tag{A.3}
$$

Thus, the virtual work introduced into the system by the electric motors driving the winches can be written as

$$
\delta W = \delta \boldsymbol{\xi}^{\mathrm{T}} \mathbf{T} = \frac{1}{\nu_{\mathrm{w}}} \delta \mathbf{x}^{\mathrm{T}} \mathbf{J}_{\mathrm{ik}}^{\mathrm{T}} \mathbf{T} \; , \tag{A.4}
$$

where $\mathbf{T} \in \mathbb{R}^{n_q}$ is the vector of motor torques. Dissipative effects like friction between the EE and the guiding surface, friction in the motor bearings and air resistance are negligible compared to the inertial forces. Thus, these effects are neglected in the model.

Considering both the rotation of the winches and the movement of the EE, the virtual work of the inertial forces can be written as

$$
\int_m \ddot{\mathbf{r}}_P \cdot \delta \mathbf{r}_P \, \mathrm{d}m = I_{\mathrm{w}} \delta \boldsymbol{\xi}^{\mathrm{T}} \ddot{\boldsymbol{\xi}} + \delta \mathbf{x}^{\mathrm{T}} \mathbf{M}_{\mathrm{EE}} \ddot{\mathbf{x}} \; , \tag{A.5}
$$

where $\mathbf{M}_{\mathrm{EE}}$ denotes the mass-matrix, see (6.6). The rotating parts of the winches (i. e. shafts, couplings and the rotor of the driving motor) can be represented by the inertia I_{w}, see (6.3).

Finally, the variation of the gravitational potential reads as

$$\delta V = \delta \mathbf{x}^{\mathrm{T}} \mathbf{g} \,, \tag{A.6}$$

with the force $\mathbf{g}$, see (6.7).

Substituting equations (A.4), (A.5), and (A.6) into equation (A.1) yields the expression

$$\frac{1}{\nu_{\mathrm{w}}} \delta \mathbf{x}^{\mathrm{T}} \mathbf{J}_{\mathrm{ik}}^{\mathrm{T}} \mathbf{T} = I_{\mathrm{w}} \delta \boldsymbol{\xi}^{\mathrm{T}} \ddot{\boldsymbol{\xi}} + \delta \mathbf{x}^{\mathrm{T}} \mathbf{M}_{\mathrm{EE}} \ddot{\mathbf{x}} + \delta \mathbf{x}^{\mathrm{T}} \mathbf{g} \,. \tag{A.7}$$

Using (6.8) to eliminate $\ddot{\boldsymbol{\xi}}$,

$$\delta \mathbf{x}^{\mathrm{T}} \left(\frac{1}{\nu_{\mathrm{w}}} \mathbf{J}_{\mathrm{ik}}^{\mathrm{T}} \mathbf{T} \right) = \delta \mathbf{x}^{\mathrm{T}} \left(\frac{I_{\mathrm{w}}}{\nu_{\mathrm{w}}^2} \mathbf{J}_{\mathrm{ik}}^{\mathrm{T}} \left(\dot{\mathbf{J}}_{\mathrm{ik}} \dot{\mathbf{x}} + \mathbf{J}_{\mathrm{ik}} \ddot{\mathbf{x}} \right) + \mathbf{M}_{\mathrm{EE}} \ddot{\mathbf{x}} + \mathbf{g} \right) \tag{A.8}$$

is obtained. Equation (A.8) must hold true for any arbitrary virtual displacement $\delta \mathbf{x}$. Thus, the terms in the brackets must be identical. Rearranging the terms finally yields

$$\underbrace{\left(\mathbf{M}_{\mathrm{EE}} + \frac{I_{\mathrm{w}}}{\nu_{\mathrm{w}}^2} \mathbf{J}_{\mathrm{ik}}^{\mathrm{T}} \mathbf{J}_{\mathrm{ik}} \right)}_{\mathbf{M}(\mathbf{x})} \ddot{\mathbf{x}} + \underbrace{\left(\frac{I_{\mathrm{w}}}{\nu_{\mathrm{w}}^2} \mathbf{J}_{\mathrm{ik}}^{\mathrm{T}} \dot{\mathbf{J}}_{\mathrm{ik}} \right)}_{\mathbf{C}(\mathbf{x}, \dot{\mathbf{x}})} \dot{\mathbf{x}} + \mathbf{g} = \underbrace{\frac{1}{\nu_{\mathrm{w}}} \mathbf{J}_{\mathrm{ik}}^{\mathrm{T}}}_{\boldsymbol{\Lambda}(\mathbf{x})} \mathbf{T} \,. \tag{A.9}$$

Using the symmetric mass-matrix $\mathbf{M}$, the Coriolis matrix $\mathbf{C}$ and the torque transformation matrix $\boldsymbol{\Lambda}$, the equations of motion can be written in the standard-form

$$\mathbf{M}(\mathbf{x})\ddot{\mathbf{x}} + \mathbf{C}(\mathbf{x}, \dot{\mathbf{x}})\dot{\mathbf{x}} + \mathbf{g} = \boldsymbol{\Lambda}(\mathbf{x})\mathbf{T} \,. \tag{A.10}$$

A.1.2 Transmission ratio design

The winch transmission ratio ν_{w} can be designed to optimally facilitate a given acceleration starting from a constant configuration. To this end, the motor torques are partitioned in the form

$$\mathbf{T} = \mathbf{T}_{\mathrm{s}} + \Delta \mathbf{T} \tag{A.11}$$

where $\mathbf{T}_{\mathrm{s}}$ is chosen uniquely by (5.1) such that the gravitational forces are compensated in the form

$$\mathbf{f}_{\mathrm{d}} = \mathbf{g} = \boldsymbol{\Lambda} \mathbf{T}_{\mathrm{s}} \,. \tag{A.12}$$

Consequently, a constant operating point $\mathbf{x}_{\mathrm{s}}$ is defined by $\dot{\mathbf{x}}_{\mathrm{s}} = \ddot{\mathbf{x}}_{\mathrm{s}} = \Delta \mathbf{T}_{\mathrm{s}} = \mathbf{0}$. Insertion of (A.11) into (6.9), and linearization around this operating point yields

$$\underbrace{\left. \left(\nu_{\mathrm{w}} \mathbf{M}_{\mathrm{EE}} + \frac{I_{\mathrm{w}}}{\nu_{\mathrm{w}}} \mathbf{J}_{\mathrm{ik}}^{\mathrm{T}} \mathbf{J}_{\mathrm{ik}} \right) \right|_{\mathbf{x} = \mathbf{x}_{\mathrm{s}}}}_{\mathbf{M}_{\mathrm{s}}(\nu_{\mathrm{w}})} \ddot{\mathbf{x}} = \mathbf{J}_{\mathrm{ik}}^{\mathrm{T}} \Delta \mathbf{T} \,. \tag{A.13}$$

The winch transmission ratio ν_{w} can be chosen such that for a given desired acceleration $\ddot{\mathbf{x}}_{\mathrm{d}}$ the motor torque $\Delta\mathbf{T}$ is minimized in the form

$$
\begin{aligned}
\min_{\Delta\mathbf{T},\,\nu_{\mathrm{w}}} \quad & \|\Delta\mathbf{T}\|_2 \\
\text{s.t.} \quad & (\nu_{\mathrm{w}}\boldsymbol{\tau}_{\min} - \mathbf{T}_s) \leq \Delta\mathbf{T} \leq (\nu_{\mathrm{w}}\boldsymbol{\tau}_{\max} - \mathbf{T}_s), \\
& \mathbf{M}_{\mathrm{s}}(\nu_{\mathrm{w}})\ddot{\mathbf{x}}_{\mathrm{d}} = \mathbf{J}_{\mathrm{ik}}^{\mathrm{T}}\Delta\mathbf{T}, \\
& \nu_{\mathrm{w}} > 0\,.
\end{aligned}
\tag{A.14}
$$

For the chosen parameters, solving the optimization problem (A.14) yields the value $\nu_{\mathrm{w}} = 19.283\,\mathrm{mm}$. Due to manufacturing tolerances in the production of the spool, the actual value of $\nu_{\mathrm{w}} = 19.53\,\mathrm{mm}$ was obtained, which was identified from measurement data.

A.2 Parameters

Parameter	Symbol	Value	Unit
Degrees of freedom	n_x	3, 1R2T	1
Number of cables	n_q	6	1
Size of robot frame	−	1.56×1.56	m
End effector radius	r	0.235	m
End effector mass	m_{EE}	4.45	kg
End effector moment of inertia	$I_{z,\mathrm{EE}}$	0.12	kgm^2
Winch transmission ratio	ν_{w}	19.53	mm
Winch moment of inertia	I_{w}	$1.81 \cdot 10^{-4}$	kgm^2
Cable force limits	$\tau_{\min}, \tau_{\max}$	10, 280	N
Cable force target	τ_{d}	50	N
Cable type	−	Liros D-Pro 01505-0100	−
Cable diameter	−	1	mm
Number of Motors	−	6	−
Electric Motors	−	AM8033-0FB1	−
Inverters	−	AX8206-0000	−
Rated motor power	−	1.7	kW
Control system	−	TwinCAT 3	−

Table A.1: Prototype CDPR parameters.

Cable	Anchor point	Groove offset	Winding dir.
i	$\mathbf{r}_{A,i}$ in m	$h_{C,i}$ in mm	s_i
1	$[0.447, -0.760, 0.038]^{\mathrm{T}}$	13.75	1
2	$[0.760, 0.004, 0.026]^{\mathrm{T}}$	−2.75	−1
3	$[0.445, 0.760, 0.032]^{\mathrm{T}}$	2.75	1
4	$[-0.445, 0.760, 0.020]^{\mathrm{T}}$	−8.25	−1
5	$[-0.760, 0.005, 0.038]^{\mathrm{T}}$	8.25	1
6	$[-0.442, -0.760, 0.014]^{\mathrm{T}}$	−13.75	−1

Table A.2: Prototype CDPR geometry parameters.

Parameter	Symbol	Value	Unit
Sample time	T_s	125	µs
Controller Matrix	$\mathbf{K}_{\mathrm{P}}$	diag($[20, 20, 400]$)	N/mm, N m/rad
Controller Matrix	$\mathbf{K}_{\mathrm{D}}$	diag($[150, 150, 8]$)	N s/m, N m s/rad

Table A.3: Controller parameters.

Bibliography

[1] Statista. "Operational stock of multipurpose industrial robots worldwide from 2010 to 2020." (2022), [Online]. Available: `https://www.statista.com/statistics/281380/estimated-operational-stock-of-industrial-robots-worldwide/` (visited on 10/16/2022).

[2] C. Müller, *World robotics 2022 – industrial robots*, IFR Statistical Department, VDMA Services GmbH, Frankfurt am Main, Germany, 2022.

[3] N. M. S. Consulting. "Global opportunity analysis and industry forecast." (2022), [Online]. Available: `https://www.nextmsc.com/report/warehouse-robotics-market` (visited on 10/16/2022).

[4] K. Lynch and F. Park, *Modern Robotics: Mechanics, Planning and Control*. Cambridge: Cambridge University Press, 2017, ISBN: 978-1-107-15630-2.

[5] S. Qian, B. Zi, W.-W. Shang, and Q.-S. Xu, "A review on cable-driven parallel robots," *Chinese Journal of Mechanical Engineering*, vol. 31, no. 1, pp. 1–11, 2018.

[6] C. Alias, I. Nikolaev, E. G. C. Magallanes, and B. Noche, "An overview of warehousing applications based on cable robot technology in logistics," in *IEEE International Conference on Service Operations and Logistics, and Informatics*, 2018, pp. 232–239.

[7] V. Mattioni, E. Ida, and M. Carricato, "Design of a planar cable-driven parallel robot for non-contact tasks," *Applied Sciences*, vol. 11, no. 20, p. 9491, 2021.

[8] X. Jin *et al.*, "Upper limb rehabilitation using a planar cable-driven parallel robot with various rehabilitation strategies," in *Cable-Driven Parallel Robots*, Cham: Springer, 2015, pp. 307–321, ISBN: 978-3-319-09489-2.

[9] D. Fedorov and L. Birglen, "Differential noncircular pulleys for cable robots and static balancing," *Journal of Mechanisms and Robotics*, vol. 10, no. 6, p. 061 001, 2018.

[10] R. L. Williams and P. Gallina, "Planar cable-direct-driven robots: Design for wrench exertion," *Journal of intelligent and robotic systems*, vol. 35, no. 2, pp. 203–219, 2002.

[11] G. Feiler, M. Schwegel, U. Knechtelsdorfer, and A. Kugi, "Design and analysis of a class of planar cable-driven parallel robots with arbitrary rotation," *IFAC-PapersOnLine*, vol. 55, no. 27, pp. 82–88, 2022, 9th IFAC Symposium on Mechatronic Systems.

[12] M. V. K. Reddy, "Orientability of the moving platform in planar cable robots," M.S. thesis, Indian Institute of Science, Bengaluru, India, 2019.

[13] M. V. K. Reddy, N. C. Praneet, and G. K. Ananthasuresh, "Planar cable-driven robots with enhanced orientability," in *Cable-Driven Parallel Robots*, Cham: Springer, 2019, pp. 3–12, ISBN: 978-3-030-20751-9.

[14] P. Miermeister and A. Pott, "Design of cable-driven parallel robots with multiple platforms and endless rotating axes," in *Interdisciplinary Applications of Kinematics*, Cham: Springer, 2015, pp. 21–29.

[15] K. Hirosato and T. Harada, "Analysis of cable-configurations of kinematic redundant planar cable-driven parallel robot," in *Cable-Driven Parallel Robots: Proceedings of the 4th International Conference on Cable-Driven Parallel Robots 4*, Springer, 2019, pp. 35–46.

[16] E. Staffetti, H. Bruyninckx, and J. De Schutter, "On the invariance of manipulability indices," in *Advances in Robot Kinematics: Theory and Applications*, Dordrecht: Springer, 2002, pp. 57–66, ISBN: 978-94-017-0657-5.

[17] T. Yoshikawa, *Foundations of Robotics: Analysis and Control.* London: MIT Press, 1990, ISBN: 978-0-262-24028-4.

[18] M. Gouttefarde, J.-P. Merlet, and D. Daney, "Wrench-feasible workspace of parallel cable-driven mechanisms," in *IEEE International Conference on Robotics and Automation*, 2007, pp. 1492–1497.

[19] M. Gouttefarde and C. M. Gosselin, "Analysis of the Wrench-Closure Workspace of Planar Parallel Cable-Driven Mechanisms," *IEEE Transactions on Robotics*, vol. 22, no. 3, pp. 434–445, 2006.

[20] L. Gagliardini, M. Gouttefarde, and S. Caro, "Design of reconfigurable cable-driven parallel robots," in *Mechatronics for Cultural Heritage and Civil Engineering*, New York: Springer, 2018, pp. 85–113.

[21] A. Pott, *Cable-Driven Parallel Robots: Theory and Application* (Springer Tracts in Advanced Robotics). Cham: Springer, 2018, ISBN: 978-3-319-76138-1.

[22] J. Rotman, *An Introduction to the Theory of Groups* (Graduate Texts in Mathematics). New York: Springer, 1999, ISBN: 978-0-387-94285-8.

[23] M. Yuan and F. Freudenstein, "Kinematic analysis of spatial mechanisms by means of screw coordinates. part 1—screw coordinates," *Journal Eng. Industry Trans. ASME*, vol. 93, no. 1, pp. 61–66, 1971, ISSN: 1087-1357.

[24] F. C. Moon, *Applied dynamics: with applications to multibody and mechatronic systems.* New York: Wiley, 1998, ISBN: 0-471-13828-2.

[25] L.-W. Tsai, *Robot analysis: the mechanics of serial and parallel manipulators.* New York: Wiley, 1999, ISBN: 0-471-32593-7.

[26] R. Fletcher, "A modified marquardt subroutine for non-linear least squares," Theoretical Physics Division, Atomic Energy Research Establishment Harwell, UK, Tech. Rep., 1971.

[27] M. Balda. "Lmfsolve.m: Levenberg-marquardt-fletcher algorithm for nonlinear least squares problems." (2009), [Online]. Available: `https : / / www . mathworks . com / matlabcentral / fileexchange / 16063 – lmfsolve – m – levenberg – marquardt – fletcher – algorithm – for – nonlinear – least – squares – problems` (visited on 11/04/2022).

[28] R. G. Roberts, T. Graham, and J. M. Trumpower, "On the inverse kinematics and statics of cable-suspended robots," in *1997 IEEE International Conference on Systems, Man, and Cybernetics. Computational Cybernetics and Simulation*, IEEE, vol. 5, 1997, pp. 4291–4296.

[29] R. Verhoeven and M. Hiller, "Tension distribution in tendon-based stewart platforms," in *Advances in Robot Kinematics*, Dordrecht: Springer, 2002, pp. 117–124.

[30] R. Dubey and J. Y. Luh, "Redundant robot control using task based performance measures," *Journal of Robotic Systems*, vol. 5, no. 5, pp. 409–432, 1988.

[31] J. A. Melkebeek, *Electrical Machines and Drives : Fundamentals and Advanced Modelling* (Power Systems). Cham: Springer, 2018, ISBN: 3-319-72730-3.

[32] F. Khorrami, P. Krishnamurthy, and H. Melkote, *Modeling and adaptive nonlinear control of electrical motors* (Power systems). Berlin: Springer, 2003, ISBN: 3-540-00936-1.

[33] M. Riemer, W. Seemann, J. Wauer, and W. Wedig, *Mathematische Methoden der Technischen Mechanik : Für Ingenieure und Naturwissenschaftler*, 3. Aufl. 2019. Wiesbaden: Springer, 2019, ISBN: 3-658-25613-3.

[34] B. Siciliano, O. Khatib, and T. Kröger, *Springer handbook of robotics*, 2nd edition. Berlin Heidelberg: Springer, 2016, ISBN: 3-319-32550-7.

[35] V. Santibañez and R. Kelly, "Global asymptotic stability of the PD control with computed feedforward in closed loop with robot manipulators," *IFAC Proceedings Volumes*, vol. 32, no. 2, pp. 683–688, 1999.

[36] B. Paden and R. Panja, "Globally asymptotically stable 'PD+'controller for robot manipulators," *International Journal of Control*, vol. 47, no. 6, pp. 1697–1712, 1988.

[37] D. Asane, A. Schmitz, and S. Sugano, "Investigating the strain behaviour of dyneema under cyclic loads," in *Annual Conference on Robotics and Mechatronics*, The Japan Society of Mechanical Engineers, 2020, 1P2–K05.

[38] J. C. Weis, B. Ernst, and K.-H. Wehking, *Use of High Strength Fibre Ropes in Multi-Rope Kinematic Robot Systems*. Berlin, Heidelberg: Springer, 2013, pp. 185–199.

[39] C. Vasile, M. Pascu, and R. T. Limited, *Practical Guide to Polyethylene*. Shrewsbury: RAPRA Technology Press, 2005, ISBN: 1-85957-493-9.